30 cm Drop Modeling

Spent Fuel and Waste Disposition

Prepared for
U.S. Department of Energy
Spent Fuel and Waste Science and Technology
Nicholas A Klymyshyn, Kevin Kadooka, Pavlo Ivanusa, Casey Spitz, James F Fitzpatrick

SUMMARY

This unlimited distribution milestone report is the deliverable for M2SF-20PN010202012.

This report documents modeling and analysis of the 30 cm cask drop scenario for spent nuclear fuel (SNF) casks. The 30 cm drop is an important hypothetical dynamic loading scenario for SNF because 10 CFR 71.71 defines testing requirements for normal conditions of transport (NCT) of SNF packages, and free drop (of 30 cm for the heaviest packages) tests are required. Other NCT conditions specified in 10 CFR 71.71 include vibration normally incident to transport, and DOE's multimodal transportation test (MMTT) and related analysis concluded that mechanical shock and vibration incident to transportation is negligible for SNF structural integrity because the loads are so small. The SNF cask 30 cm drop has a lot more potential to cause damage to SNF because the kinetic energy and momentum of the system is stopped abruptly during the cask impact event. Test data and model predictions both agree that the SNF assemblies are subjected to significantly higher loads in a cask drop event than normal transportation shock and vibration, but currently there is no reason to expect gross structural damage of the fuel assembly or widespread SNF cladding failure as a result of a 30 cm cask drop. The ultimate goal of this work is to close the knowledge gap of stress profiles on SNF rods and fuel assembly components during NCT, and this report describes the progress toward reaching that goal as well as a plan for finishing this work over the next year or two. Key remaining tasks include refining the fuel assembly model, calculating a selection of specific fuel assembly cases to populate the damage model, and finally running the damage model to predict the full general response range of 30 cm drop loads on SNF.

Cask drop and fuel assembly drop tests provide data that is needed to validate structural dynamic finite element models of fuel rods and fuel assembly components. This report documents the evaluation of the test data and the application of that data to inform and validate finite element models and analysis methods. Modeling the specific scenarios that were tested (the as-tested configuration) is the first step of the analytical process. Once the models are demonstrated to closely approximate the test conditions, they can be applied to the general cask drop scenario to estimate the response of other configurations (irradiated fuel rods, other cask impact orientations, other fuel assembly designs, etc.). This study uses established, commercially available finite element software (LS-DYNA, ANSYS) and the technical challenge is modeling the structural dynamic impact phenomena effectively. SNF cask and nuclear material package

"Test data and model predictions both agree that the SNF assemblies are subjected to significantly higher loads in a cask drop event than normal transportation shock and vibration, but…

… *currently there is no reason to expect gross structural damage of the fuel assembly or widespread SNF cladding failure as a result of a 30 cm cask drop.*

The ultimate goal of this work is to close the knowledge gap of stress profiles on SNF rods and fuel assembly components during NCT, and this report describes the progress toward reaching that goal as well as a plan for finishing this work over the next year or two."

designers use these tools for design and safety demonstration purposes, and other industries model this kind of structural dynamic impact behavior routinely (automobile crashworthiness, metal forming, etc.), so there is already confidence that the models can calculate an accurate, engineering-level prediction of impact response. The test data provides us a novel opportunity to validate fuel rod and fuel assembly level impact models.

One of the important observations from the 1/3 scale cask drop testing at BAM in December 2018 is that the impact response of fuel assemblies is varied throughout the cask. Rather than all responding in unison, the fuel assemblies show evidence of secondary impacts that vary by basket location. The single fuel assembly drop test of 2020 also showed evidence of a secondary impact, which resulted from a gap developing between the fuel assembly and the basket tube during freefall. The practical implication is that fuel assemblies in a cask drop scenario should be expected to experience a range of loading, rather than identical structural loads at every basket location. To close the knowledge gap, we must evaluate the variation and uncertainty in this kind of loading scenario. In a 32-fuel assembly cask there are potentially over 8,000 fuel rods, and there is a very significant practical difference between a single fuel rod structural failure and 1% fuel rod failure. A natural variation in fuel assembly loads by position is apparent in the test data and closing the stress profiles knowledge gap requires an understanding of the load distribution. It can be overly conservative and misleading to determine the maximum possible loading conditions, without also determining minimum and mean loads, and the locations of those loading conditions.

This is because risk and consequence analyses must make assumptions of the amount of fuel rods that fail within a cask during a postulated event. For example, NRC's NUREG-2224 (a document that is currently in draft form) is expected to identify 1% fuel rod rupture as an acceptable assumption for determining canister pressure and temperature during normal conditions of storage, 10% fuel rod rupture during off-normal events, and 100% rod rupture for accident events. Part of closing the stress profiles knowledge gap is relating what we learn from testing and modeling to what the industry and regulatory bodies need to perform their analyses.

A new full fuel assembly finite element model was developed to account for the permanent deformation of spacer grids that was observed in the test data. This new model is an evolutionary change from PNNL's previous fuel rod model and it uses beam elements to represent the grid spacers. The model agrees reasonably well with validation data at this point in its development, but the model needs more accurate energy dissipation. The model is currently too conservative in calculating cladding strain compared to test data and increasing energy dissipation through damping or other means is expected to improve model performance. A conservative model can still be useful, but because our goal is accurate simulation of the impact test response, it is recommended that the model be improved to better match the test data. Collecting more test data would also be valuable, as discussed in this report.

The general case of the 30 cm drop could include any impact orientation, any SNF cask, and any fuel assembly design, which is a potentially broad range of impact response. The condition of the SNF at the time of impact (such as temperature, burnup, gap conditions, etc.) can also affect the structural loads transmitted to the SNF assembly. PNNL's detailed fuel assembly model takes too long to run to be able to evaluate every single fuel assembly design, cask design, impact orientation, and SNF condition, so PNNL is developing a damage modeling tool to complete the analysis of the general 30 cm drop case. The damage modeling tool works by modeling the trends observed in single fuel assembly 30 cm drop analyses. The results of fuel assembly drop analyses form a database that the damage tool uses to estimate similar conditions, using regression techniques across many variables. A limited number of single fuel assembly drop cases are needed to be the starting basis of the damage tool, and then more single fuel assembly drop cases will be added as necessary to expand the parametric study and explore the range of results. It is expected that the damage modeling tool described in this report could be used very effectively to understand the variability and uncertainty in stress and strain conditions in the fuel assemblies for the range of impact load conditions in the 30 cm drop scenario. The damage model would

ultimately be used to bound the range of stress profiles within the fuel assemblies by estimating the full range of response for all 17 cask systems, and all fuel assembly designs. The damage model would close the stress profile knowledge gap by describing the overall range of loads and provide estimates of the loading range for specific fuel and cask configurations.

This project also identified the critical need to relate the SNF cladding strains recorded in testing and calculated in the fuel assembly model to localized failure criteria that are based on Sibling Pin test campaign results. One challenge is relating strains or loads recorded or calculated on one fuel assembly design to the strains and loads that are anticipated to occur if the same loading scenario happens to other fuel assembly designs. There is not a direct translation of forces, bending moments, or strains from one fuel design to the next. Mechanical loads caused by the 30 cm drop scenario are very short in duration, so the time component of loads needs to be considered. There is also the possibility that loads are path-dependent, when complex phenomena like sliding fuel pellet fragments are considered. Relating the structural dynamic loads observed and modeled at the fuel assembly level to laboratory scale tests of fuel cladding and fuel rod segments is an important step in closing the SNF stress profiles knowledge gap. This report explains the technical concerns and proposes the project tasks to make this critical connection in FY2021.

This page is intentionally left blank.

ACKNOWLEDGMENTS

This page is intentionally left blank.

CONTENTS

This page is intentionally left blank.

LIST OF FIGURES

LIST OF TABLES

ACRONYMS

BAM	Bundesanstalt für Materialforschung und –prüfung (German Federal Institution of Materials Research and Testing)
BWR	boiling water reactor
CFR	*Code of Federal Regulations*
CG	center of gravity
DOE	U.S. Department of Energy
EPRI	Electric Power Research Institute, Inc.
ENSA	Equipos Nucleares, S.A., S.M.E
FEA	finite element analysis
FY	fiscal year
HAC	hypothetical accident condition
INL	Idaho National Laboratory
MMTT	ENSA/DOE multimodal transportation test
NCT	normal conditions of transport
PNNL	Pacific Northwest National Laboratory
PWR	pressurized water reactor
SFWST	Spent Fuel and Waste Science and Technology
SNF	spent nuclear fuel
SNL	Sandia National Laboratories

This page is intentionally left blank.

30 CM DROP MODELING

1   INTRODUCTION

This report describes modeling and analysis of a 30 cm drop of a spent nuclear fuel (SNF) cask that supports experimental testing and achievement of the goal of closing the knowledge gap related to SNF loads in a normal conditions of transport (NCT) cask drop scenario. The DOE-NE SFWST research and program is guided by the high-level goal of closing prioritized knowledge gaps, which are summarized in Saltzstein et al. 2020. The gap study is updated on a regular basis and guides DOE investment in research projects. The SNF stress profiles knowledge gap is critical to the SFWST program because effective mechanical testing of SNF requires an understanding of the magnitude and frequency of mechanical loads that are relevant to NCT. Conservatively high estimates of mechanical loads can be a problem for the test programs if they perform tests outside the real range of interest. Closing the stress profiles knowledge gap means that the current state of knowledge and understanding of mechanical loads on fuel is sufficient to guide effective SNF test programs that acquire useful and relevant test data. Closing the knowledge gap also provides useful information to the SNF community, including regulatory bodies such as the US Nuclear Regulatory Commission (NRC).

Over the last few years, the U.S. Department of Energy (DOE) has conducted a cask and fuel assembly experiential drop test campaign to record structural dynamic data about instrumented casks and surrogate nuclear fuel assemblies. The project team involves multinational collaboration between Equipos Nucleares (ENSA) of Spain, Bundesanstalt für Materialforschung und –prüfung [German Federal Institution of Materials Research and Testing] (BAM), and DOE, with the DOE team including staff from Sandia National Laboratories (SNL) and Pacific Northwest National Laboratory (PNNL). The DOE team is led by SNL, and its expertise is in testing and data collection. PNNL's expertise is in modeling and structural dynamic analysis, and its role on the team is to help design the experiments with pre-test modeling and analysis. After the data are collected, PNNL's continuing role is to validate numerical models of the tests and eventually apply the validated models and methods to cask drop scenarios that are beyond the loading range of practical testing. For example, this type of testing cannot include real, radioactive SNF. Validated models are required to predict how real SNF would behave under similar loading conditions, as well as in all other feasible drop conditions that are relevant to the DOE Spent Fuel and Waste Sciences and Technology (SFWST) program's interests. For example, the testing was done in the horizontal drop orientation, and this report studies the range of all possible cask drop orientations to determine the one that has the highest loads for the specific test article that was tested.

The 30 cm drop is a standard test performed to demonstrate SNF cask compliance with Title 10 of the *Code of Federal Regulations* 71.71 (10 CFR 71.71), the CFR that pertains to SNF packages. 10 CFR 71.71 is concerned with cask integrity and does not specify any requirements to preserve the integrity of SNF within the cask. The drop is performed onto an unyielding surface, which is harder than concrete or soil. The drop test does not attempt to create realistic cask drop conditions—it is a test that cask makers perform according to the description in the regulations. The purpose of studying the SNF response to such a test is to evaluate the fuel response to the prescribed test conditions. The test generally represents a set of loading conditions that a package is expected to maintain to sustain its function and its structure without the need to replace any of the cask's structural components. The structural requirements are such that a cask that is dropped according to the test conditions essentially remains in its as-manufactured state and could be placed back into service (with damaged impact limiters replaced with new ones).

It is valuable to know how the fuel would respond to a 30 cm drop because that is a benchmark case. Cask drops that might occur during the handling and transportation of SNF are not limited to 30 cm. The 30 cm drop onto an unyielding surface is intended to be harsh enough to represent the upper bound of dynamic structural loads a cask might bear during normal operation. The test is conceptual, rather than literal—there is no expectation that a cask will regularly be dropped 30 cm. Understanding how SNF will

respond to the conceptual 30 cm drop is important to maintaining consistency with the cask regulatory expectations. If a cask is expected to survive a 30 cm drop onto an unyielding surface and remain transportable, it is beneficial for everyone to understand what would happen to the fuel assemblies during such an event. One could conservatively assume that all of the fuel rods would fail to maintain their integrity in a 30 cm drop event, but the test data so far and the current modeling results suggest that fuel rods would maintain a significant margin from losing their structural integrity from a 30 cm cask drop event. Quantifying the structural dynamic loads on the SNF is the key purpose of this testing and modeling campaign, and this is the specific knowledge gap that this report addresses.

1.1 Report Contents and Organization

The tests described in this report were completed in the 2018 to 2020 time frame, but because PNNL's scope goes beyond modeling of the test configurations, this work is not yet complete. This report captures the modeling and analysis completed to date and identifies where additional work is needed to close the knowledge gaps. Key remaining tasks include refining the fuel assembly model, calculating a selection of specific fuel assembly cases to populate the damage model, and finally running the damage model to predict the full general response range of 30 cm drop loads on SNF. The authors propose to continue the work of cask drop modeling in fiscal year 2021 (FY 2021), and plan to perform additional experimental tests to collect more data to improve the models and perform additional analyses to generalize the model results in a way that is applicable to all potential SNF cask drops. One key to generalizing the testing and modeling results is to use the damage prediction model that PNNL initiated this year and is described in this report.

Section 2 of this report covers cask modeling. A 1/3-scale model is validated against the test data collected at BAM and data from earlier ENUN-32P cask testing conducted at SNL (Ammerman and Lum 2011).

Section 3 evaluates the influence of the fuel basket in the 30 cm drop scenario. In the ENSA/DOE multimodal transportation test (MMTT) (McConnell et al. 2018), it was concluded that the basket had a negligible effect on normal conditions of transportation (NCT) shock and vibration loading of SNF (Klymyshyn et al. 2018), and the cask and basket could be considered rigid structures when defining the load transmission from cask to SNF. It was hypothesized that the transportation shock and vibration loads were too small for the basket structure to have a relevant effect. The 30 cm drop has higher loads, so the structural dynamic contribution of the basket was studied. Both test data and modeling were used to evaluate the behavior of the basket. The test data were evaluated for channel correlation and secondary impacts of the fuel assemblies with the baskets due to natural gap formation. A modeling sensitivity study was also conducted, to study the effect of basket stiffness.

Section 4 discusses the SNL fuel assembly drop test (Kalinina et al. 2020). The transducer test data and video data were analyzed to gain an understanding of what happened during the test and to inform modeling and analysis methods. PNNL developed a new fuel assembly finite element model that includes grid permanent deformation capability, which is a necessary feature in the 30 cm cask drop loading regime. The grid impact forces are large enough that grid permanent deformation is a credible possibility, with a range that could include limited plastic compression, unstable buckling, or significant grid structural collapse.

Section 5 begins the general analysis of the 30 cm cask drop, which looks beyond the as-tested horizontal drop configuration to evaluate other impact orientations. Closing the SNF stress profiles knowledge gap from a 30 cm drop requires considering all potential drop orientations. The NCT shock and vibration loading regime is fixed in its orientation, because all SNF casks in the United States are designed for horizontal travel. In rail transportation, the cask remains parallel to the rails. In a cask drop scenario, the cask can hit the ground in any impact orientation. PNNL completed an initial modeling study of the ENUN-32P cask being dropped in several impact orientations (as described in Section 2) and determined that the 60° from vertical impact orientation was most limiting. Section 5 also describes

modeling work related to the general cask drop scenario that was completed this year, and identifies key additional work that needs to be completed to close the knowledge gap.

Section 6 describes a damage model that PNNL began developing this year as a specific predictive tool to help close the stress profiles knowledge gap. The general cask drop scenario includes many variables, including impact orientation, gap conditions, cask mass, and impact limiter performance metrics. The idea is to develop a software tool that can predict the loads in fuel assembly components and determine whether cladding or other fuel assembly components will fail as a result of the loading. The tool is immediately useful to the program in helping establish the boundaries of fuel cladding damage in the 30 cm cask drop scenario. It may be enough for the program to establish the maximum damage that any arbitrary 30 cm drop could cause. Klymyshyn et al. (2019) used validated models to demonstrate that the MMTT data set was enough to close the knowledge gap for NCT shock and vibration. The damage model is a similar concept, where the physical testing provides validation of the models, and the models will be applied to a variety of cask drop configurations to populate the library of data needed for the damage model. When the knowledge gap is closed, the damage model will remain, and can be used during actual SNF transportation campaigns to assess cask drops that happen in the field. Any SNF cask drop of 30 cm or less is currently expected to not require repackaging. If the program proceeds with 9 m cask drop testing, the damage model could be expanded to cover the consequences of cask drops up to 9 m. PNNL recommends completing the damage model for the 30 cm drop height in FY 2021.

Section 7 discusses the main conclusions of this work scope, which includes analysis of test data, development of finite element models, and an initial start on generalizing what was learned in testing of the 30 cm horizontal cask drop scenario. It highlights what was learned and proposes a path for closing the stress profiles knowledge gap with additional analyses and testing.

1.2   Usage, Models, and Methods

Note that this report uses the symbol uE to identify strain in the unit of microstrain to maintain consistency with previous reports. 1 uE is equal to .000001 mm/mm, and the multimodal transportation test recorded strains up to about 100 uE on the fuel cladding during NCT and handling (Klymyshyn et al. 2018; Kalinina et al. 2018). Rail transportation was typically below 50 uE at its peak, and a 2000-mile train transportation leg only recorded 4000 strain cycles above 10 uE in magnitude. The 30 cm drop scenario recorded much higher strains, up to 1500 uE. PNNL used a common frequency filter for all data channels with a 300 Hz upper cutoff frequency which affects the peak values discussed in this report. Unfiltered values are available from Kalinina et al. (2020). This report is focused on modeling the fuel assembly drop phenomenon to help close the stress profiles knowledge gap.

Also note that the models and analytical methods described in this study are evolved from previous structural dynamic modeling studies performed by PNNL. One important report is Klymyshyn et al. (2018), which describes how the MMTT data were used to validate structural dynamic models of fuel rods, fuel assemblies, and other key components of an SNF cask and railcar system. That report concluded that a single fuel rod finite element model was sufficient to predict loads on the fuel rods during normal conditions of transportation (NCT), because the mechanical shock and vibration loads were so small that rod-to-rod contact was not possible. The magnitudes of the loads were generally so small that no significant structural damage to the fuel rods, fuel assembly components, or any other components in the complete railcar conveyance system was expected. The peak instantaneous acceleration of the cask was recorded to be less than 0.3 g in the westbound rail transportation leg, and even with potential dynamic amplification of forces on the contents inside the cask PNNL saw no reason to formally calculate guide tube stresses or grid spacer contact forces. The 30 cm cask drop case is a very different dynamic loading scenario, and spacer grid loads and dynamic response is a significant topic in this report. Evaluating guide tube stresses is planned for future work.

This report treats the 30 cm cask drop mechanical loading environment as being an additional loading environment that is distinct from NCT shock and vibration. The 30 cm drop causes a high-momentum,

short-duration dynamic structural load. The cask travels 30 cm (1 foot) from a state of rest and achieves a velocity of 2.4 m/s when any part of the cask touches the impact surface. The freefall takes approximately 0.25 seconds. The linear travel distance, the change in velocity, and the duration of cask movement are all distinctly different from the shocks and vibrations that can happen to a cask while it is carried by a conveyance system during transportation.

The design of a railcar suspension system controls the gross range of movements of a cask during transportation. In the 50 mph pitch and bounce test case studied by Klymyshyn et al. (2018) as a pre-test prediction, the cask vertical velocity only varied within ±0.15 m/s, even though the peak cask acceleration was recorded to be about 0.24 g (2.35 m/s^2). This indicates that the 0.24 g peak acceleration had to be only 10s of milliseconds in duration. The point is that the gross cask motion is tightly constrained by the conveyance system, and the equations of motion of classical mechanics can be applied to test data to determine the range of motion. This is where the difference in loading from NCT shock and vibration and 30 cask drop scenarios is most apparent.

Railcar suspension systems are designed with springs and damping features that provide the railcar dynamic system (below the railcar deck) with a damped natural frequency of about 2 Hz. The vertical railcar deck motion is limited to moving as the suspension system allows, and the cask and cradle system sits on top of the railcar deck. This arrangement makes the cask motion tightly constrained by the surrounding structures and components. Nothing like the 30 cm cask drop can happen when the cask is connected to its conveyance – except under hypothetical accident conditions, which are not currently being evaluated by the SFWST program. The prominence of the ~2 Hz loading condition is clear in the frequency analyses of the test data (Kalinina 2018; Klymyshyn 2018).

Modeling the loading conditions of cask handling and NCT shock and vibration were covered previously (Klymyshyn et al. 2018, 2019). This report covers the 30 cm cask drop loading condition, which is a separate loading environment. This covers normal conditions of transportation. Normal conditions of dry storage loading is another, future task that is needed for cumulative effects analysis. Seismic loads are expected to be very important to the dry storage evaluation because earthquakes can potentially cause strong mechanical loads.

2   CASK IMPACT MODELING

This section discusses the development and implementation of a cask impact structural dynamics model to analyze 30 cm drop events. The cask impact modeling discussed in this work has two main objectives. The first is to simulate the shock and vibration environment to which SNF will be subjected during 30 cm drop events. Motion time histories extracted from the cask impact model can be used in downstream structural dynamic models of SNF to quantify the effects of drop events on fuel integrity. The second objective is to investigate the effects of parameter variations that cannot be tested easily or cost-effectively, such as evaluating multitudes of cask impact orientations and sensitivity analyses related to physical gaps within the system.

The cask impact model described in this work is similar to the one used for pre- and post-test analysis of the BAM drop (Klymyshyn and Ivanusa 2019), with a number of modeling simplifications used to improve computational efficiency. One very important simplification involves the impact limiter finite element representation. Instead of attempting to model all of the individual pieces of the impact limiters, they are homogenized as representative volumes of material that provide a similar crushing and reaction force behavior. The cask is relatively rigid, compared to the crushable impact limiter material, and, for the interests of this study, the only function the impact limiters have is to provide the correct deceleration forces on the cask body. The impact limiters are represented by two crushable material zones— representing the aluminum honeycomb and the polyurethane foam. The crushing behavior of these two materials is generally known, but the crush strength (the most important material parameter in this study) naturally varies over a known range. The impact limiter crush strengths of the current model were specifically selected to be consistent with the data collected from the 30 cm drop test of a 1/3-scale package at BAM in 2018, as well as various 9 m drops of a 1/3-scale cask at SNL in 2010 (Klymyshyn and Ivanusa 2019; Ammerman and Lum 2011).

It is well known that impact limiter behavior varies by design, and examples within a single design will vary by temperature and by the specific crush strengths of the pieces of material used in its construction. PNNL's approach is to model the behavior of specific tests where data are available to support model validation, and then to consider the more general case of the potential range of cask drop behavior, and the behavior of different cask designs. The key physical quantity from test data is cask deceleration, which is usually reported as a peak deceleration in units of gravity (g). Another key test datum is the impact pulse history over time. This report does not fully address cask impact variation and variability, but this topic is identified for follow-up work that is needed to close the stress profiles knowledge gap for the general 30 cm cask drop scenario. This report documents models that are validated against available test data and initial work on the general cask drop scenario.

Section 2.1 discusses the model of the 1/3-scale ENSA ENUN-32P cask and impact limiters used in previous package drop test campaigns. This includes a description of the LS-DYNA model as well as the general approach used to select the impact limiter parameters that appropriately match the response seen in the test data. This is a necessary precursor step to full-scale cask modeling. All of the available test data exist for 1/3-scale packages; a 1/3-scale model validated relative to these data can then be scaled up for full-scale analyses. The model response was consistent with both 30 cm and 9 m package drop data; peak package decelerations were within +12%, -1% of the test data.

Section 2.2 discusses a variety of full-scale drop analyses done to evaluate conditions other than the as-tested horizontal drops at BAM. A wide range of impact orientations were simulated, and five potentially limiting conditions were selected for further analysis with a structural model of fuel in Section 5.1. Several of these, corresponding to cask impacts oriented 20°, 40°, and 60° from vertical, had higher package decelerations than the as-tested horizontal (90°) configuration. A sensitivity study was also conducted to evaluate secondary impact caused by the gap between the basket and cask at impact. The cask dynamics were found to be negligibly affected by this parameter. Secondary impacts between the

basket and surrogate assemblies, and basket and a full fuel structural model, are investigated separately in Sections 3.2 and 5.1, respectively.

Section 2.3 summarizes the major findings of the cask impact modeling, which are the acceleration loads expected in a 30 cm drop scenario for the specific package and impact limiters tested, and the identification of a number of potentially limiting drop orientations. This section also highlights several research activities that would help to close the knowledge gap, namely generalization of the modeling results to different package and fuel designs.

2.1 Validation of 1/3-Scale Cask Model

The 1/3-scale cask model was developed to validate against available test data. This is an intermediate step in the analytical process because the real interest is in full-scale cask system response. The 1/3-scale system is 1/27 of the volume and mass of a real system, but the impact limiters provide 1/9 of the total impact force to the system. That makes accelerations in the 1/3-scale system nominally three times higher. If a 1/3-scale finite element analysis (FEA) model agrees well with 1/3-scale test data, the FEA model can easily be scaled up to calculate the full-scale response.

2.1.1 Model Description

An LS-DYNA model of a 1/3-scale ENSA ENUN-32P dual-purpose cask and its impact limiters was developed based on ENSA design drawings (Figure 2-1). It represents the actual configuration tested at BAM and SNL (Klymyshyn et al. 2018; Ammerman and Lum 2011). The model incorporates a level of detail similar to the model used for pre-test and post-test analysis of the BAM drop (Klymyshyn and Ivanusa 2019), in that it uses simplified, homogenized geometry. For instance, for each impact limiter, the crushable material, skin, and gussets are simplified into a single body that has uniform material properties. In the cask, the neutron absorber, steel body, lid, and fasteners are likewise condensed into a single body. Eliminating fine mesh detail allows the simulation to be done more efficiently. The current model has two more additional simplifications than the earlier work. First, the basket is constructed from shell elements instead of solids. Second, the surrogate assemblies are defeatured and represented as rectangular prisms that have dimensions, mass, and flexural rigidity that are identical to the actual components. These modeling simplifications are shown to be justifiable through favorable comparisons to package drop data in the following sections.
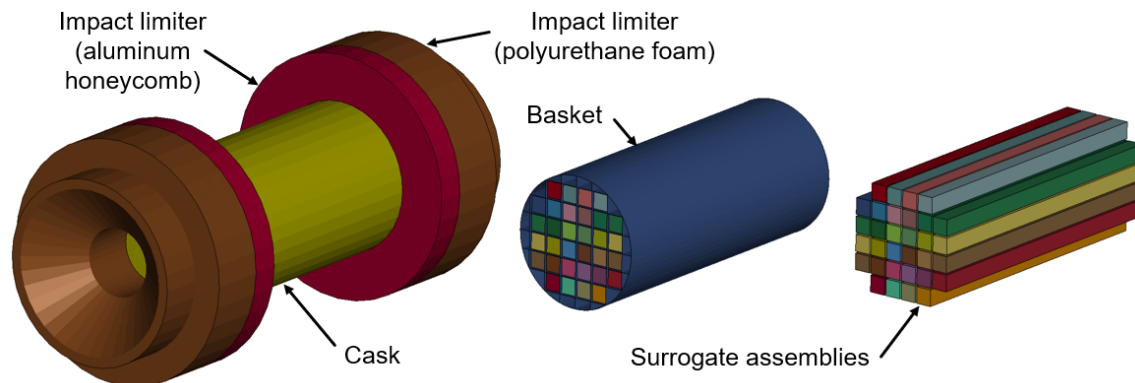
Figure 2-1. LS-DYNA Model of the ENSA ENUN-32P Cask and Impact Limiters

Additional technical details about the cask impact model are presented in Appendix A.

2.1.2 Overview of Model Validation

The cask impact model was compared to the cask acceleration magnitudes measured in the drop tests. Acceleration of the cask was chosen as the main variable to compare the model and test data, because it

represents the load imparted to SNF in a drop event. The impact limiter material response is the most important parameter needed to set the cask dynamics, because it is the main means of energy absorption during an impact.

Data from five different package drop conditions were used to select impact limiter parameters from a known range of values. The data sources and associated drop orientations are summarized in Table 2.1 and illustrated in Figure 2-2. In side and end drops, the cask is oriented such that it impacts on the side (cylindrical surface) or end (flat surface) of the impact limiters. In a slapdown drop, the cask impacts first on a corner and subsequently tips onto either the side or end face. The center of gravity over corner drop is a type of slapdown event where the center of gravity is oriented over the point of initial impact such that angular displacement is maximized between the initial and subsequent impact. The model validation process included data from both 30 cm and 9 m drops. This provides confidence that the model behaves correctly in both low- and high-energy impact regimes. The BAM test is documented by Kalinina et al. (2018). The SNL test is documented by Ammerman and Lum (2011).

Table 2.1.   Summary of Package Drop Data Used in Cask Impact Model Validation

Drop Height	Impact Orientation	Description	Test Location
30 cm	Side drop	Two tests were conducted, one with basket unrotated (orthogonal to the ground) and rotated 45°. Tests were conducted at room temperature.	BAM
9 m	Side drop	Test conducted with cask chilled to ~-29°C.	SNL
	End drop	Test conducted with cask chilled to ~-29°C.	
	Slapdown	Angled 10° from horizontal. Test conducted with cask chilled to ~-29°C and also heated to ~100°C.	
	Center of gravity-over-corner	Angled 69° from horizontal. Test conducted with cask heated to ~100°C.	
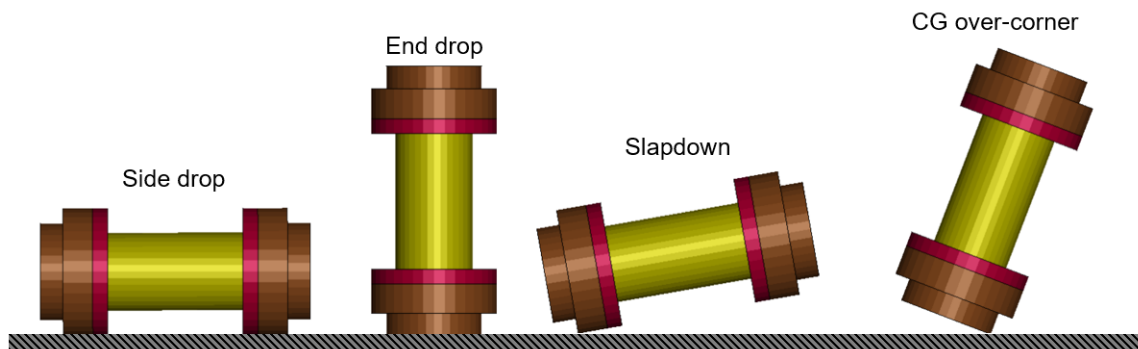
Figure 2-2.   Drop Orientations Represented in the Validation Data

Four parameters were used to inform selection of the impact limiter properties: the impact limiter crush strength and volume fraction at full compaction, for each of the two impact limiter materials (polyurethane foam and aluminum honeycomb). Literature values were used as starting points to inform selection of each parameter. A strategy for selecting the correct impact limiter properties was derived based on the known intensity and direction of each drop, as summarized here, but explained in full detail in Appendix A. Essentially, the relatively low-energy 30 cm drop was used to inform the crush strength, whereas the high-energy 9 m drops were used to inform the volume fraction at full compaction. The end

drop was used to inform the polyurethane foam properties, because that material is exclusively compressed in that test, whereas the side drops compress both materials.

All modeling and test data shown in this section are filtered to eliminate high-frequency noise and sensor drift. The BAM test data were filtered by PNNL with a 0.1–400 Hz band pass filter. The SNL test data were reported with a 300 Hz low-pass filter. The filtering applied to the model output is consistent with the filtering used on the test data in each case.

2.1.3   BAM Test Data Validation Results

Data for 30 cm package drops were available for the test at BAM in 2018 and also at SNL in 2010. Data from the BAM test were used for model validation, because they included additional instrumentation for the cask internals, including the surrogates and basket. The BAM and SNL tests also yielded very similar cask accelerations. Two drop tests were conducted at BAM, one with the basket in a nominal configuration (basket cells orthogonal to the ground) and one with the basket rotated 45°. Both configurations were modeled, but because the tests yielded very similar package accelerations, the drop with the nominal basket configuration was primarily used for model validation.

Efforts were made to model the actual conditions of the drop test as closely as possible. Analysis of the drop data showed that there was a slight angle to the drop, resulting in the "A" (lid) end of the cask impacting slightly (~2 ms) before the "D" (bottom) end. This was accounted for in the model by rotating the package a small amount from horizontal (0.12°). Delays in the onset of acceleration in the cask, basket, and surrogate assembly acceleration data suggest that there were physical gaps in the package at the moment of impact. Trial-and-error modeling found that a gap of 0.6 mm between the cask cavity floor and bottom of the basket provided the approximately 1 ms delay between cask and basket acceleration seen in the test data. Delays between the basket and surrogate assembly accelerometers varied between about 0.5 and 2 ms, which suggests that a range of basket-to-surrogate gaps were present during the test. As a simplification, a uniform gap of 0.5 ms was applied in the model, which provided a delay of between 1 and 2 ms.

Figure 2-3 compares the package acceleration in the model and the test. The data represent the average acceleration of each body; this is the nodal average in the model, and average of the accelerometers in the test. Good agreement is seen between the model and test. The duration of the acceleration pulse is similar, approximately 15 ms for both. The model tends to slightly overpredict the cask acceleration (43 g versus 38 g, a difference of 12%). This demonstrates that the impact limiter behavior is representative of and slightly conservative compared to the test article.
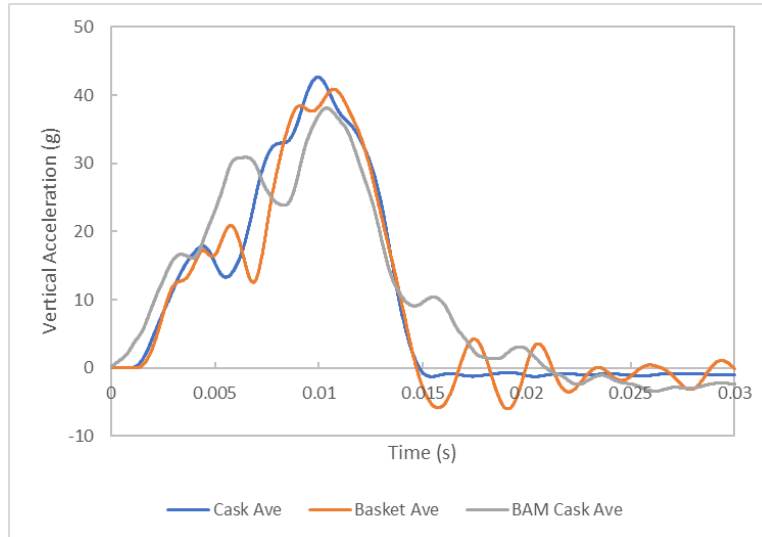
Figure 2-3. Comparison of Model and Test Package Acceleration in the BAM 30 cm Side Drop, Nominal Basket Configuration

Accelerations of the surrogate assemblies were used to validate the elastic properties of the basket and surrogate assemblies in the model. In the BAM test, 11 of the 32 surrogate assemblies were instrumented with accelerometers mounted at the lid or bottom end of the assembly, and in some cases, at both ends. For comparison, acceleration at each end of the surrogate assemblies was calculated in the model. Table 2.2 summarizes the acceleration of the surrogate assemblies in the nominal and rotated basket tests (full surrogate assembly acceleration data and their positions in the basket are shown in Appendix A, Table A.3 and Table A.4).

Table 2.2. Comparison of Model and Test Surrogate Assembly Acceleration in the BAM 30 cm Side Drop

| | Surrogate Assembly Acceleration, g | | | |
| | Nominal Drop | | Rotated Drop | |
	Test	Model	Test	Model
Lid avg.	117.3	95.1	111.8	107.3
Bottom avg.	168.0	136.8	155.9	147.2
Overall avg.	139.5	115.9	129.9	127.2
Lid peak	161.9	154.4	167.2	162.8
Bottom peak	244.6	232.0	223.8	229.3

The test and modeling results did not show a significant difference in surrogate assembly accelerations between the nominal and rotated drops. It was originally thought that the rotated drop might yield higher accelerations, because it would result in a larger contact area between the basket and surrogate assemblies, but this was not the case. In both the model and test, the surrogate assembly accelerations for the rotated and nominal drops were within 10% of each other. Nevertheless, the model data showed good agreement with the test data; the average and peak accelerations of the surrogate assemblies were within 19% and 6% of each other, respectively.

2.1.4   SNL Report Validation Results

Data from the 9 m package drops conducted at SNL in 2010 were used to validate the model against higher-energy impact data. These drops also included additional impact orientations, which afforded

opportunities to compare the model behavior in configurations besides the side drop. Unlike the BAM tests, the cask internals were not instrumented. Thus, comparisons between model and test are limited to the overall package acceleration. Additional information about modeling the 9 m drops is presented in Appendix A, and the results are summarized in Table 2.3. Hypothetical accident conditions such as 9 m drops are beyond the scope of this work, but they were included as part of the model validation so that the cask impact model could be used to model such scenarios in the future.

Table 2.3.   1/3-Scale Model Peak Package Accelerations and Error Compared to Test Data

Test Case	Model Package Peak Acceleration, g (% error)
30 cm side drop	43 g (+12%)
9 m side drop	134 g (+1%)
9 m end drop	113 g (+9%)
9 m slapdown	86 g (+5%)
9 m corner drop	89 g (-1%)

2.1.5   Summary of Model Validation

The cask impact model achieves good agreement with the available 30 cm and 9 m drop test data. Table 2.3 summarizes the package accelerations calculated in the validation studies. The maximum error was within +12% to -1% when compared to test data, which is within the expected level of modeling and test uncertainty. The model predicted greater accelerations than the test data in almost every scenario, which suggests that the model is conservative. It is also worth noting that the validation data set came predominantly from tests in which the package was chilled or at room temperature, rather than warmed by decay heat. This makes the impact limiter material stiffer and more unyielding than under normal operating conditions, which means that the model has been validated against a conservative data set.

Emphasis was put on comparing the model to the results of the 30 cm drop tests conducted at BAM, in particular, expanding on the previous post-test analysis (Klymyshyn and Ivanusa 2019). The model retained a similar level of agreement in terms of package acceleration, and improved the agreement in terms of acceleration pulse duration. Comparisons of the surrogate assembly accelerations showed good agreement between the model and tests, providing confidence that the model accurately represents the shock and vibration environment inside the cask for the specific conditions for which the model was validated to agree.

This model validation demonstrates that the model works well for the test data to which it was compared. This study goes on to study the model response under conditions that were not validated by test data. The philosophy is that the model works reasonably well according to the test data we do have, so it is reasonable to trust that the model results will represent cask performance beyond the range of the test data. The key is that the finite element model is fundamentally defined to obey the natural laws of physics and the theories of engineering mechanics. By showing the model is validated against a selection of impact conditions we can have confidence that the model works reasonably well under all similar impact conditions. At this point, we are aiming for reasonable confidence in the models to study the loading conditions on SNF and fuel assembly components. Future work will focus on formally closing the knowledge gap.

2.2   Full-scale Cask Analyses

The 1/3-scale cask model was converted to a full-scale package model by adjusting the model dimensions to match full-scale design drawings provided by ENSA. The majority of the model remained unchanged from the validated 1/3-scale model. The sole change was to update the surrogate assembly

dimensions, mass, and flexural rigidity to represent the 17x17 pressurized water reactor (PWR) fuel assembly used in Sections 4.2 and 5.1. The flexural rigidity of the surrogate assemblies was modified by adjusting the modulus of elasticity to achieve the same first bending mode as the detailed fuel assembly model. This model was used to study the effect of impact orientation and gap size on cask dynamics during 30 cm drop events.

2.2.1   Cask Impact Orientation Study

The objective of this study was to determine the effect of impact orientation on the cask shock and vibration environment, and to identify potentially adverse orientations besides the as-tested side drop configuration for future analysis.

The 30 cm drop was modeled using 19 different orientations of the full-scale cask model, ranging from a completely vertical configuration to a completely horizontal configuration. Figure 2-4 shows the coordinate system used to define the cask orientation, as well as a local coordinate system used to track acceleration along the longitudinal axis of the cask (X') and orthogonal to it (Z'). In terms of acceleration loads on SNF, the X' direction induces an axial compressive load on the fuel, while Z' induces a bending moment on the fuel. The horizontal impact configuration tested at BAM is 0°. A longitudinal end drop is 90°. The study evaluated many angles between 0° and 90°.

For this study, it was assumed that all gaps (such as basket-to-surrogate assembly, and cask-to-basket gap) were initially very small, and all bodies were nearly in contact (i.e., no secondary impacts). The presence of initial gaps in the structure and secondary impact are considered in Section 2.2.2 and Section 5.1.2.3. Rotation of the basket is not considered, because testing and modeling described in the previous sections showed that the effect on package and surrogate assembly acceleration is minimal.

The results of the impact orientation study are summarized in Figure 2-5. These data allow one to estimate the impact orientations that are most adverse in terms of the SNF shock and vibration environment, and to select potentially adverse orientations for further analysis (Table 2.4). Limiting scenarios were identified by looking for local maxima in the X' and Z' accelerations. The center of gravity (CG)-over-corner drop (20°) is one such orientation, because it featured the highest lateral acceleration at one end of the basket. The 40° case is another potentially interesting case because of the high axial acceleration on the surrogate assemblies (caused by secondary impact in slapdown) and relatively high lateral acceleration. The 60° case was also earmarked for further analysis, because it featured the highest lateral acceleration felt by the surrogate assemblies. The 0° case was chosen because of the high axial acceleration, and the 90° case was chosen because it was the as-tested configuration. The 90° case can be compared as the full-scale counterpart to the 1/3-scale BAM drop test. The cask acceleration drops by a factor of three—43 g to 14 g—and the acceleration pulse broadens threefold from about 14 ms to 40 ms. This corroborates the finding of the initial post-test modeling that indicated that the 1/3-scale drop acceleration magnitude and duration can be scaled by approximately a factor of three.

The orientation study is discussed in further detail in Appendix A, along with time histories for each of the drop orientations.
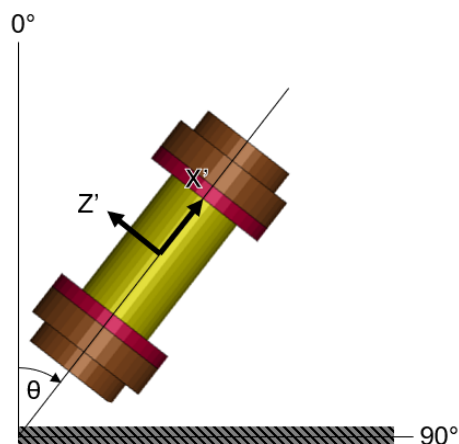
Figure 2-4. **Coordinate System for Cask Drop Orientation Study (90° = horizontal)**
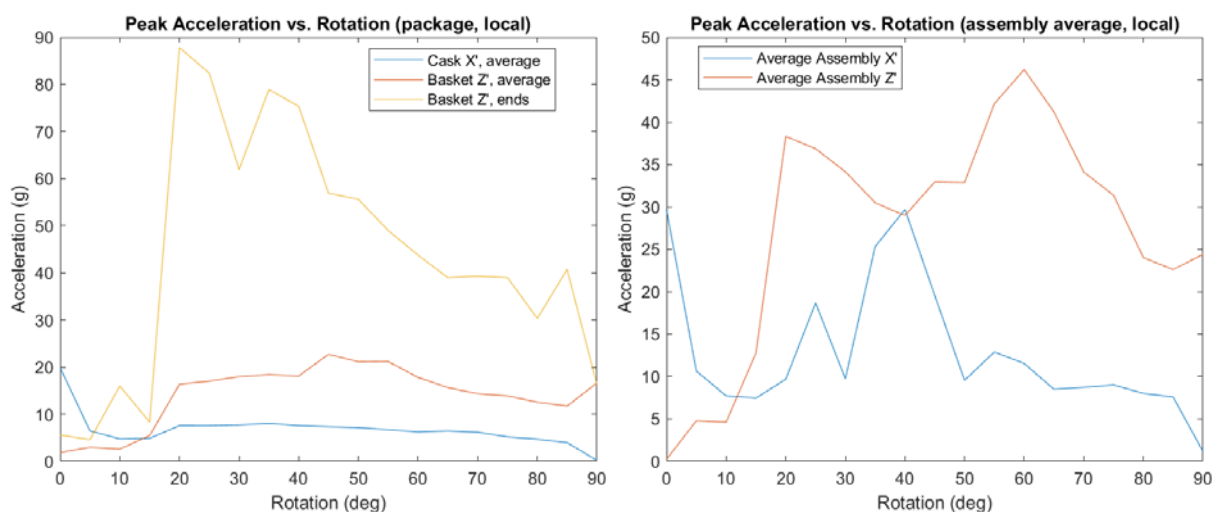
Figure 2-5. **Package (left) and Surrogate Assembly (right) Accelerations in Impact Orientation Study**

Table 2.4. **Cask Orientations Selected for Downstream Fuel Structural Dynamics Modeling**

Orientation	Justification
0°	Reference configuration. Highest axial acceleration on cask (19.9 g average) and high axial acceleration on surrogate assemblies (29.6 g).
20°	Highest local lateral acceleration of basket (87.8 g).
40°	Highest axial acceleration on surrogate assemblies (29.7 g), high lateral acceleration on basket (18.1 g, 75.3 g locally) and surrogate assemblies (29.0 g).
60°	Highest lateral acceleration on surrogate assemblies (46.2 g).
90°	Reference configuration. Lateral acceleration was 16.6 g on the basket and 24.4 g on the surrogate assemblies.

2.2.2   Cask-to-Basket Gap Sensitivity Study (Secondary Impacts)

The objective of this study was to identify the sensitivity of the cask dynamics to the gap between the cask and the basket at the moment of impact. Within the cask, there is clearance between the ends of the basket and the ends of the cask, and there is also radial clearance between the diameter of the basket and the diameter of the cask. In the full-scale cask modeled in this work, the longitudinal and radial clearances are about 10 mm and 5 mm, respectively. When this gap is fully closed on the impacting end of the package, the mass of the cask and the basket both participate in the initial impact. On the other hand, when a gap exists, a secondary impact occurs between the cask and the basket. The five cask orientations identified in Table 2.4 were run with three different gap conditions: zero gap, half gap, and full gap. Equal fractions of the longitudinal and radial gap were applied, i.e., in the zero gap case, the initial gap was 0 mm in both the longitudinal and radial directions, and in the full gap case, the initial gap was 10 mm and 5 mm in the longitudinal and radial directions, respectively.

Figure 2-6 shows the result of this sensitivity study. Accelerations were calculated for the cask, basket, and surrogate assemblies. No significant change in cask or basket acceleration occurred as a result of varying the initial gap. Some variations were observed, and the accelerations tended to increase with increasing gap, but the difference was always less than 5 g. Even less change was observed in the acceleration of the surrogate assemblies, with a difference of acceleration of less than 3 g. The sole exception was the lateral acceleration in the 60° cask orientation drop, which increased by 16 g.
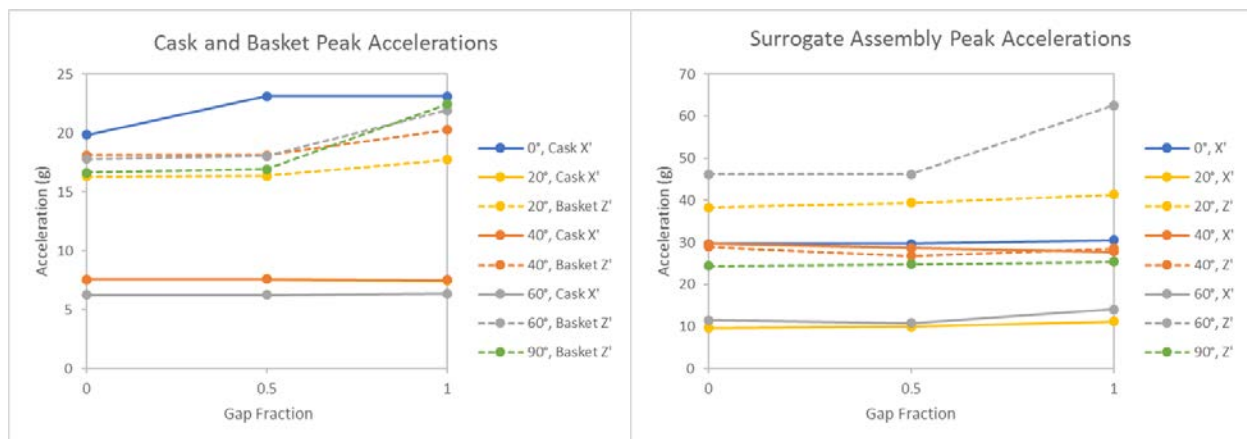
Figure 2-6.   Sensitivity Study Investigating Effect from Cask-to-Basket Gap on Cask and Basket Accelerations (left) and Average Surrogate Assembly Acceleration (right)

This study indicated a slight sensitivity of the cask dynamics to the basket-to-cask gap. Acceleration of cask components, including surrogate assemblies, tended to increase as the gap increased, showing that secondary impacts tended to yield higher shock and vibration loads during a drop. However, only 1 case out of the 15 analyzed had an increase in acceleration of above 5 g. It is worth noting that the surrogate assemblies modeled in this section are nearly rigid bodies, and the accelerations shown here are representative of the average acceleration that might be observed at the CG of a fuel assembly, not an individual fuel rod. This study addresses one of the sources of secondary impacts in a package drop; the effect of the fuel-to-basket gap is addressed in Section 5.1.2.3 with a more detailed structural model of the fuel.

2.3   Conclusion

A cask impact model has been developed that builds upon the pre-test and initial post-test modeling of the 1/3-scale 30 cm cask drop conducted at BAM in 2018. The model developed in this work uses optimized impact limiter properties that, when simulated with more precise modeling of the drop conditions, produces good agreement with the BAM test data, including accelerations of the package and

its surrogate assembly contents. The model also demonstrated good agreement with 9 m cask drop data from tests conducted at SNL in 2010. Compared to the available cask drop data used in this study, the peak package and surrogate assembly accelerations calculated in the model were within 12% and 6%, respectively, and the model tended to err toward conservatism. The validation study in this work compared the model to both room temperature (BAM) and chilled (SNL) test data. It is acknowledged that a range of ambient temperatures could be encountered in the field, which will influence the impact limiter properties, and thus, the cask dynamics. This study predicts the cask dynamics somewhere within the range of responses expected in field conditions, and further work is suggested to generalize the modeling results.

The validated 1/3-scale model was then enlarged to full scale to model an array of hypothetical 30 cm drop conditions. A suite of 19 different cask impact orientations were modeled, ranging from an end drop to a side drop, in equal rotation increments. In the side drop configuration, the package acceleration decreased by a factor of three (14 g package, 24 g average of surrogate assemblies) compared to the 1/3-scale as-tested configuration, which corroborates previous conclusions about the scaling of the test data. The maximum package acceleration lateral to the SNF occurred in slapdown events. The *average* lateral acceleration of the package did not exceed 25 g during these events. A *local* acceleration of 88 g was calculated at one end of the basket in the CG-over-corner drop (20° from vertical). The maximum average acceleration of the surrogate assemblies was 46 g, calculated in a slapdown impact of a cask dropped 60° from vertical. The maximum acceleration axial to the SNF occurred in the end drop event, where the package acceleration was 20 g and the average surrogate assembly acceleration was 30 g.

Five drop orientations were studied for further analysis using the crushable grid fuel assembly model introduced in Section 4.2. These included two reference orientations (0° and 90° from vertical) and three potentially adverse orientations (20°, 40°, and 60°) where large axial and/or lateral accelerations were observed. The motion time histories calculated from the cask impact model were applied to the fuel assembly model to evaluate their effect on cladding structural integrity. These generic 30 cm drop analyses are discussed in Section 5.1.

The full-scale cask impact modeling summarized in Figure 2-5 describes an envelope for the accelerations that can be expected for a similar cask and impact limiter design in a 30 cm drop. The average package acceleration was in the range of 12–25 g lateral to SNF and below 10 g axially, except in the case of the end drop, where the axial acceleration is maximized, at 20 g. Local accelerations of the package can be much higher in slapdown impacts, where the lateral acceleration at one end can be up to around 90 g. This is comparable to the approximately 50–80 g acceleration measured at the ends of the basket in the full-scale 30 cm fuel assembly drop test conducted at SNL in 2020 (Section 4). This suggests that the test conditions were toward the higher end of the range of accelerations expected for a 30 cm drop.

Thanks to previous pre- and post-test modeling of the ENSA ENUN-32P package and a substantial amount of test data used for model validation, the cask impact model is well-defined. The results presented here should be representative of packages of similar size, mass, and impact limiter design. However, it is recognized that the U.S. fleet of casks is not monolithic, and the 30 cm cask drop loading environment at SNF could feasibly be more adverse for different package designs, particularly those of lower mass and stiffer impact limiter behavior. PNNL is still working to generalize these results to estimate the comprehensive range of SNF loading from 30 cm cask drops. We eventually will relate what we have learned from this specific modeling study to a broad understanding of 30 cm cask drop loads that ultimately closes the knowledge gap. The damage model described in Section 6 is a step toward generalizing the loads and evaluating their challenge to SNF integrity.

This study addresses only the 30 cm NCT drop condition. However, the model has been validated against a variety of 9 m drop test data. Similar studies could be conducted to evaluate package dynamics under such higher-energy hypothetical accident condition (HAC) impacts.

As we work to close the knowledge gap, a number of technical issues remain to be fully understood. PNNL recommends these follow-up activities:

- Understand the range of cask design behavior. There are 17 cask systems in the USA that can be carried by the Atlas railcar and the 8-axle railcar currently in the design phase, and additional legal-weight truck casks like the NAC LWT and the GA-4. To close the knowledge gap we need to know the full range of 30 cm drop responses, or we need a sensitivity study that covers a broad range of cask responses. We currently understand the ENSA ENUN-32P behavior from test data, but more work is required to understand the behaviors of the full fleet of casks.

- Once we understand the full range of cask behavior, we can apply that understanding to evaluate the full range of fuel assembly behavior. A 17x17 PWR assembly is expected to be the most limiting fuel assembly design because of its diameter and cladding wall thickness, but some evaluation of boiling water reactor fuel assemblies and other types of PWR assemblies (like a 16x16, which has a different guide tube structure) is needed. The 17x17 PWR assembly is the first and most important assembly to be evaluated. The Atlas NCT analysis (Klymyshyn et al. 2019) concluded that it was not necessary to evaluate other fuel assembly types for NCT shock and vibration. The loads on the fuel assembly are so much higher in the 30 cm drop (as discussed in Section 3) that we still need to evaluate other fuel assembly types and hardware until we can conclude that the most limiting configurations have been considered. This point is discussed more in the conclusions section in Section 3.

- The damage model discussed in Section 6 is the way we envision resolving the knowledge gap in a generalized way. The damage model relates cask loads to fuel assembly component damage. Currently, that model is focused on cladding damage, but eventually we want to include fuel assembly hardware damage as well. This point is discussed more in the conclusions section in Section 6.

This page is intentionally left blank.

3   BASKET ANALYSES

The fuel basket within an SNF cask or canister is a significant structure. The design of baskets varies across the industry. The ENSA ENUN-32P cask is the focus of this study because it is the design that was tested. Technical details of the basket are available to PNNL and the models were constructed to closely resemble the actual design, but the details cannot be shared. PNNL's approach is to model the as-tested condition for validation purposes, and them perform parametric sensitivity studies to estimate how variations in basket design might affect the structural dynamic response. These basket analyses do not cover the entire range of baskets in the industry because the overall size and number of fuel assemblies the basket must accommodate varies by cask design.

Section 3.1 looks closely at the basket and fuel assembly response from data collected at the 2018 BAM 1/3rd-scale cask drop tests. There were two horizontal drops, a "parallel" case with basket walls parallel (and perpendicular) to the impact surface, and a "rotated" case with the basket walls aligned at 45-degrees relative to the impact surface. The cases were very similar in their responses. A cross-correlation analysis of the data channels was performed to see which channels are closely related in their impact responses. In addition, the test data provide indications of gaps naturally developing during the drop test—gaps between the fuel assemblies and the basket that delay the response of the fuel assemblies to the cask impact. These observations from the test data affect how the structural dynamic analysis must be performed and evaluated.

Section 3.2 evaluates the role of the basket in the LS-DYNA models of the ENSA ENUN-32P dual-purpose cask. Internal energy is a measure of the strain energy in deformable bodies, and the model calculates that the impact limiters experience the most internal energy by a wide margin (this is mostly by the crushing of impact limiter material to permanently dissipate impact energy). The basket holds a relatively small amount of elastic energy, which is released during the rebound phase of impact. A sensitivity study was performed to vary basket stiffness. While the amount of internal energy in the basket changes significantly over the range of interest, the effect on the fuel assembly impact response is much less significant.

Section 3.3 discusses the observation that the fuel basket had a negligible effect on the transmission of loads to the fuel rods during the NCT shock and vibration recorded during the MMTT. From a structural dynamic modeling perspective, Klymyshyn et al. (2018) found that the cask and basket could be considered rigid bodies to simplify the models and still achieve good agreement with MMTT test data. The situation for the 30 cm drop is different, and the basket is much more important to the accurate transmission of loads. This section explains why the basket is more important in the 30 cm drop.

3.1   BAM 30 cm Drop Analyzed Data

The BAM 30 cm drop consisted of two horizontal cask drop tests. In the first test the cask was dropped with the fuel assemblies parallel to the floor, and in the second test the cask was rotated 45º in relation to the first test. Both tests were analyzed in a similar manner: the data were read in their original form; then they were filtered with a low-pass, Butterworth filter with a half-power frequency of 300 Hz; and finally, the maximums and minimums were found for the accelerometers. In this section, only the filtered results are presented because the unfiltered results have high-frequency data that would not be useful or meaningful for modeling purposes.

Table 3.1 shows the summarized results for both the parallel and rotated drops. Only the Z-accelerometers are shown because they typically had the highest magnitudes of acceleration. In the parallel drop, the Z-accelerometers are the actual accelerometers as they were pointing vertically. In the rotated drop, however, the Z-accelerometers were no longer vertical, and thus, pseudo-Z-accelerometers were created for the purposes of evaluating the vertical motion experienced by the fuel assemblies, basket, and cask. The A and D sides come from the instrumentation naming convention and refer to opposite ends of the cask (A is the bolted lid end and D is the welded baseplate end). The dummy fuel

assemblies had accelerometers attached near the A and D ends. Kalinina et al. 2019 documents the test and the data in detail.

Table 3.1.   Summarized Accelerations for the Various Sections of the Cask

Section	Side	Max (g) - Parallel	Max (g) - Rotated
Cask	A	40	30
	D	51	42
Basket	A	63	64
Fuel Assemblies	A	110	120
	D	187	184

To create the pseudo-Z-accelerometer, the analysis used the respective Y- and Z-accelerometers in combination. If no respective Y-accelerometer existed, the negative of the Z-accelerometer data was used. The following equation shows how the data for the pseudo-Z-accelerometer was constructed:

$$Z' = Z \cos\left(-\frac{\pi}{4}\right) + Y \sin\left(-\frac{\pi}{4}\right)$$

where Z' is the pseudo-Z-accelerometer and Z and Y are the original Z- and Y-accelerometers. The reason for the negative rotation is that the cask was rotated clockwise in the YZ-plane.

Table 3.1 shows that the fuel assemblies had the highest accelerations by a significant margin, around two times higher than the basket. This table also shows that the D-side of the cask experienced greater shocks than the A-side because, when the cask was dropped, it was not dropped perfectly level, causing the A-side to impact first. In the two tests, both the basket and the cask had much lower shock responses than the fuel assemblies, but the basket always had higher shock responses than the cask. This result was not unexpected because the fuel assemblies would have the most higher frequency motion, while the basket and the cask both consisted of mostly bulk motion, lacking the higher frequency responses.

Also, in both tests, the parallel drop and the rotated drop had similar responses. The cask experienced similar responses for the two drops, but they were generally lower in the rotated drop. This decrease could be due to the difference in the structural integrity of the impact limiter. The basket, however, had a virtually identical response in both tests. The fuel assembly responses were also similar for the two tests. The highest response in both tests was from the top-center assembly D-side (A5D), while the bottom-corner assemblies had the lowest responses for both sides (A2A, A4A, A6A, and A7A). Interestingly, A2D, A4D, and A7D, had much higher responses on the D-side and were not among the lowest accelerations compared to the respective A-side accelerometers. Also, the parallel test had the highest A-side response in the center second row (A10A), while the rotated test had the highest response in the top-corner (A3A).

As for the most significant changes between the two tests, A2D, A3A, and A3D had significant increases, more than 23–31 g, in maximum accelerations from the parallel to the rotated test, while A4D and A7D decreased significantly, 24 g and 45 g, from the first to second drop. All other accelerometers had changes of less than 14 g.

The main conclusion from this analysis is that the parallel and rotated cases had a very similar response. This suggests that it is not necessary to explore the full 360-degree rotation range through modeling. Instead, the rotation could be accounted for in the general cask drop scenario by developing uncertainty bands on model input parameters, or by accepting some uncertainty on model results. The uncertainty effect of angular rotation on the general cask drop case is something to explore in future work. This topic is mentioned in Section 7, where topics needed to close the knowledge gap are discussed.

3.1.1   Correlations

Another method of analyzing the data for any similarities and patterns is using correlations between the various accelerometers. Figure 3-1 and Figure 3-2 show the correlation matrix of all accelerometers. For both figures, the accelerometers are grouped into the same sections as Table 3.1: the cask A-side and then D-side accelerometers, the basket accelerometer, and then the fuel assembly A-side and then D-side accelerometers.

The patterns are similar in both drops as well. The cask accelerometers had higher correlations with other accelerometers on the same side than with those on the opposite side. In fact, each cask accelerometer is highly correlated with the other one on the same side. For example, in the parallel drop, A13AZ and A14AZ have a correlation coefficient of 0.95, while A14AZ only has a correlation coefficient of 0.49 with A15DZ and A16DZ. The basket accelerometer is also much more correlated with the other accelerometers on the same side than on the opposite side. The fuel assembly correlations show that the fuel assemblies are essentially independent in their shock response when compared to the other side. However, on the same side, the correlations can trend to be significant. It is also interesting to note that, overall, the rotated drop has more significant correlations in all of the accelerometer channels than the parallel drop.

	A13AZg	A14AZg	A15DZg	A16DZg	A12AZg	A1AZg	A2AZg	A3AZg	A4AZg	A5AZg	A6AZg	A7AZg	A8AZg	A9AZg	A10AZg	A11AZg	A1DZg	A2DZg	A3DZg	A4DZg	A5DZg	A6DZg	A7DZg
A13AZg	1.00	0.95	0.44	0.45	0.62	0.09	0.43	0.35	0.44	0.33	0.55	0.42	0.42	0.39	0.23	0.41	0.14	0.05	0.10	0.25	0.16	0.32	0.26
A14AZg	0.95	1.00	0.49	0.49	0.65	0.02	0.44	0.44	0.44	0.39	0.57	0.45	0.48	0.46	0.31	0.49	0.11	0.01	0.08	0.21	0.13	0.25	0.22
A15DZg	0.44	0.49	1.00	0.98	0.36	0.09	0.24	0.30	0.20	0.29	0.33	0.25	0.34	0.31	0.23	0.33	0.21	0.18	0.21	0.27	0.21	0.37	0.36
A16DZg	0.45	0.49	0.98	1.00	0.35	0.07	0.24	0.30	0.20	0.28	0.33	0.26	0.34	0.33	0.25	0.35	0.29	0.18	0.30	0.31	0.29	0.39	0.41
A12AZg	0.62	0.65	0.36	0.35	1.00	0.01	0.38	0.59	0.54	0.59	0.62	0.57	0.67	0.62	0.52	0.65	0.03	-0.02	-0.03	-0.01	0.01	0.00	0.13
A1AZg	0.09	0.02	0.09	0.07	0.01	1.00	-0.01	-0.07	-0.09	-0.08	-0.03	-0.08	-0.04	-0.07	-0.08	-0.08	-0.06	-0.00	0.00	-0.06	-0.04	0.01	0.00
A2AZg	0.43	0.44	0.24	0.24	0.38	-0.01	1.00	0.08	0.45	0.22	0.62	0.35	0.49	0.49	0.00	0.48	-0.07	0.07	-0.18	-0.05	-0.12	0.09	-0.08
A3AZg	0.35	0.44	0.30	0.30	0.59	-0.07	0.08	1.00	0.38	0.60	0.42	0.63	0.61	0.50	0.67	0.61	0.01	-0.05	0.13	-0.02	0.04	-0.03	0.18
A4AZg	0.44	0.44	0.20	0.20	0.54	-0.09	0.45	0.38	1.00	0.48	0.51	0.46	0.54	0.54	0.33	0.70	0.21	0.20	0.07	0.19	0.05	0.17	0.21
A5AZg	0.33	0.39	0.29	0.28	0.59	-0.08	0.22	0.60	0.48	1.00	0.54	0.64	0.76	0.66	0.63	0.69	0.15	0.08	-0.04	-0.02	0.06	0.02	0.17
A6AZg	0.55	0.57	0.33	0.33	0.62	-0.03	0.62	0.42	0.51	0.54	1.00	0.62	0.71	0.60	0.36	0.65	0.08	0.13	-0.13	0.05	0.01	0.20	0.11
A7AZg	0.42	0.45	0.25	0.26	0.57	-0.08	0.35	0.63	0.46	0.64	0.62	1.00	0.68	0.60	0.51	0.65	0.11	0.03	0.10	0.05	0.15	0.14	0.23
A8AZg	0.42	0.48	0.34	0.34	0.67	-0.04	0.49	0.61	0.54	0.76	0.71	0.68	1.00	0.76	0.51	0.82	0.05	0.06	-0.06	-0.08	-0.01	0.08	0.15
A9AZg	0.39	0.46	0.31	0.33	0.62	-0.07	0.49	0.50	0.54	0.66	0.60	0.60	0.76	1.00	0.41	0.77	0.14	0.10	-0.02	-0.09	0.02	-0.01	0.13
A10AZg	0.23	0.31	0.23	0.25	0.52	-0.08	0.00	0.67	0.33	0.63	0.36	0.51	0.51	0.41	1.00	0.52	0.09	-0.00	0.08	0.00	0.06	-0.04	0.11
A11AZg	0.41	0.49	0.33	0.35	0.65	-0.08	0.48	0.61	0.70	0.69	0.65	0.65	0.82	0.77	0.52	1.00	0.17	0.07	0.11	0.03	0.08	0.00	0.15
A1DZg	0.14	0.11	0.21	0.29	0.03	-0.06	-0.07	0.01	0.21	0.15	0.08	0.11	0.05	0.14	0.09	0.17	1.00	0.55	0.56	0.63	0.70	0.57	0.71
A2DZg	0.05	0.01	0.18	0.18	-0.02	-0.00	0.07	-0.05	0.20	0.08	0.13	0.03	0.06	0.10	-0.00	0.07	0.55	1.00	0.14	0.51	0.24	0.61	0.44
A3DZg	0.10	0.08	0.21	0.30	-0.03	0.00	-0.18	0.13	0.07	-0.04	-0.13	0.10	-0.06	-0.02	0.08	0.11	0.56	0.14	1.00	0.52	0.76	0.37	0.68
A4DZg	0.25	0.21	0.27	0.31	-0.01	-0.06	-0.05	-0.02	0.19	-0.02	0.05	0.05	-0.08	-0.09	0.00	0.03	0.63	0.51	0.52	1.00	0.60	0.72	0.65
A5DZg	0.16	0.13	0.21	0.29	0.01	-0.04	-0.12	0.04	0.05	0.06	0.01	0.15	-0.01	0.02	0.06	0.08	0.70	0.24	0.76	0.60	1.00	0.53	0.71
A6DZg	0.32	0.25	0.37	0.39	0.00	0.01	0.09	-0.03	0.17	0.02	0.20	0.14	0.08	-0.01	-0.04	0.00	0.57	0.61	0.37	0.72	0.53	1.00	0.70
A7DZg	0.26	0.22	0.36	0.41	0.13	0.00	-0.08	0.18	0.21	0.17	0.11	0.23	0.15	0.13	0.11	0.15	0.71	0.44	0.68	0.65	0.71	0.70	1.00

Figure 3-1. Correlation Matrix for Parallel Drop

	A13AZg	A14AZg	A15DZg	A16DZg	A12AZg	A1AZg	A2AZg	A3AZg	A4AZg	A5AZg	A6AZg	A7AZg	A8AZg	A9AZg	A10AZg	A11AZg	A1DZg	A2DZg	A3DZg	A4DZg	A5DZg	A6DZg	A7DZg
A13AZg	1.00	1.00	0.73	0.72	0.65	0.45	0.73	0.52	0.73	0.50	0.81	0.58	0.56	0.43	0.45	0.58	0.38	0.36	0.35	0.39	0.24	0.34	0.39
A14AZg	1.00	1.00	0.71	0.71	0.64	0.46	0.71	0.51	0.72	0.50	0.80	0.56	0.55	0.43	0.45	0.56	0.36	0.35	0.33	0.38	0.22	0.34	0.38
A15DZg	0.73	0.71	1.00	0.99	0.49	0.34	0.53	0.37	0.58	0.38	0.56	0.42	0.47	0.34	0.35	0.46	0.55	0.52	0.50	0.53	0.33	0.50	0.55
A16DZg	0.72	0.71	0.99	1.00	0.49	0.34	0.51	0.35	0.56	0.38	0.53	0.39	0.47	0.35	0.38	0.43	0.55	0.53	0.49	0.55	0.31	0.52	0.56
A12AZg	0.65	0.64	0.49	0.49	1.00	0.43	0.62	0.54	0.69	0.70	0.51	0.59	0.77	0.71	0.76	0.73	0.31	0.13	0.08	0.22	0.11	0.16	0.15
A1AZg	0.45	0.46	0.34	0.34	0.43	1.00	0.22	0.64	0.40	0.61	0.18	0.56	0.42	0.30	0.42	0.48	0.17	0.11	0.24	0.11	0.12	0.28	0.09
A2AZg	0.73	0.71	0.53	0.51	0.62	0.22	1.00	0.30	0.80	0.44	0.77	0.58	0.58	0.40	0.43	0.57	0.26	0.28	0.12	0.28	0.05	0.09	0.25
A3AZg	0.52	0.51	0.37	0.35	0.54	0.64	0.30	1.00	0.47	0.55	0.36	0.59	0.42	0.38	0.42	0.56	0.19	0.33	0.11	0.20	0.02	0.48	-0.07
A4AZg	0.73	0.72	0.58	0.56	0.69	0.40	0.80	0.47	1.00	0.61	0.68	0.63	0.73	0.55	0.54	0.76	0.14	0.15	0.11	0.14	0.05	0.06	0.12
A5AZg	0.50	0.50	0.38	0.38	0.70	0.61	0.44	0.55	0.61	1.00	0.32	0.61	0.79	0.70	0.71	0.74	0.19	-0.01	0.15	0.07	0.11	0.16	0.14
A6AZg	0.81	0.80	0.56	0.53	0.51	0.18	0.77	0.36	0.68	0.32	1.00	0.48	0.38	0.29	0.26	0.45	0.24	0.25	0.20	0.25	0.13	0.19	0.24
A7AZg	0.58	0.56	0.42	0.39	0.59	0.56	0.58	0.59	0.63	0.61	0.48	1.00	0.52	0.35	0.37	0.70	0.27	0.24	0.16	0.24	0.21	0.18	0.12
A8AZg	0.56	0.55	0.47	0.47	0.77	0.42	0.58	0.42	0.73	0.79	0.38	0.52	1.00	0.80	0.73	0.82	0.14	-0.04	0.15	0.05	0.09	0.02	0.17
A9AZg	0.43	0.43	0.34	0.35	0.71	0.30	0.40	0.38	0.55	0.70	0.29	0.35	0.80	1.00	0.70	0.67	0.07	-0.05	0.04	-0.02	0.05	0.02	0.05
A10AZg	0.45	0.45	0.35	0.38	0.76	0.42	0.43	0.42	0.54	0.71	0.26	0.37	0.73	0.70	1.00	0.63	0.10	-0.02	-0.03	0.02	-0.08	0.10	0.10
A11AZg	0.58	0.56	0.46	0.43	0.73	0.48	0.57	0.56	0.76	0.74	0.45	0.70	0.82	0.67	0.63	1.00	0.12	0.04	0.14	0.05	0.09	0.01	0.04
A1DZg	0.38	0.36	0.55	0.55	0.31	0.17	0.26	0.19	0.14	0.19	0.24	0.27	0.14	0.07	0.10	0.12	1.00	0.57	0.52	0.73	0.55	0.43	0.66
A2DZg	0.36	0.35	0.52	0.53	0.13	0.11	0.28	0.33	0.15	-0.01	0.25	0.24	-0.04	-0.05	-0.02	0.04	0.57	1.00	0.09	0.80	0.01	0.79	0.35
A3DZg	0.35	0.33	0.50	0.49	0.08	0.24	0.12	0.11	0.11	0.15	0.20	0.16	0.15	0.04	-0.03	0.14	0.52	0.09	1.00	0.35	0.78	0.08	0.56
A4DZg	0.39	0.38	0.53	0.55	0.22	0.11	0.28	0.20	0.14	0.07	0.25	0.24	0.05	-0.02	0.02	0.05	0.73	0.80	0.35	1.00	0.31	0.61	0.55
A5DZg	0.24	0.22	0.33	0.31	0.11	0.12	0.05	0.02	0.05	0.11	0.13	0.21	0.09	0.05	-0.08	0.09	0.55	0.01	0.78	0.31	1.00	-0.06	0.53
A6DZg	0.34	0.34	0.50	0.52	0.16	0.28	0.09	0.48	0.06	0.16	0.19	0.18	0.02	0.02	0.10	0.01	0.43	0.79	0.08	0.61	-0.06	1.00	0.28
A7DZg	0.39	0.38	0.55	0.56	0.15	0.09	0.25	-0.07	0.12	0.14	0.24	0.12	0.17	0.05	0.10	0.04	0.66	0.35	0.56	0.55	0.53	0.28	1.00

Figure 3-2. Correlation Matrix for Rotated Drop

The main conclusion of this channel correlation study is that the channels are generally correlated on each end of the cask, as expected, but less correlated on opposite ends. If the impact was perfectly horizontal it is possible that all channels might be correlated, but with the slight angle it makes sense that the opposite ends behave like separate events.

Another observation is that the channel data on each end are not perfectly correlated. There is some variation in correlation, which indicates a variation of local response. The amount of variation is important to understand when it comes to modeling the general cask drop case. PNNL is primarily modeling the fuel assembly response analysis with a single fuel assembly model. The kind of variation in response observed in relation to basket location needs to be accounted for in some way in the general cask drop analysis. It is suspected that the variation by basket location has to do with differences in gaps and future work is recommended to investigate this relationship.

3.1.2   Delay Versus Maximum Accelerations

Another facet of the BAM 30 cm drop that needs to be considered is that there was a time delay from when the cask impacted the ground to when the internal components of the cask, the fuel assemblies and basket, impacted the interior of the cask. This delay had an impact on the acceleration experienced by each component. To analyze the effect of this delay, the accelerations of the first impact for the various accelerometers were compared, and a trend, either first or second order, was calculated.

The trend was calculated using the following method.

1. The time of the first impact was found for the A-side and D-side for each accelerometer. This was done by finding the first large peak in the acceleration data.

2. The average time of impact of the cask for each side was found.

3. A linear fit, of either first or second order, was calculated comparing the time of the first impact and the magnitude of the largest peak using only the cask and fuel assembly accelerometers.

Using the above method, results were found for the significance of the initial delay in the first impact, with several important caveats: (1) the basket accelerometer was not used in the fitting calculation but was plotted on the graphs for comparison purposes; (2) the average time of impact for the cask was used, which does allow for some of the cask accelerometers to have a negative delay; (3) the largest peak was used, not the first peak, for the magnitude because the goal was to compare the time of impact and its effect on the absolute maximum; and (4) the cask accelerations were used in the fit to help constrain the Y-intercepts (zero second delay accelerations) to reasonable values.

Table 3.2 shows the results for the different drops, which are split into A- and D-side and into first and second order for both drops. The zero second delay accelerations are shown, along with the R^2 and Adjusted R^2 statistics. The Adjusted R^2 takes into account the number of points and the order of the fit and reduces the traditional R^2 value. Figure 3-3 and Figure 3-4 show the respective graphs. On the graphs are several sets of data points and curves: the cask data, the dummy assembly data, the dummy basket data on the A-side only, the fitted curve, and the 95% prediction intervals. Although the prediction intervals do show unlikely answers, i.e., negative accelerations, they are included to show that the variability can still be high.

Overall, both drops show that there is a correlation between first impact delay and the magnitude of the largest acceleration. The parallel drop, overall, has higher correlations than the rotated drop for all but one of the fits, the first order D-side trend. Interestingly, the parallel drop has better correlations on the A-side trends, while the rotated drop has better correlations on the D-side trends. Also, the parallel drop shows that the second-order trends have higher R^2 and Adjusted R^2 values for both sides, but the rotated drop shows that the second order only has higher R^2 values. In general, if there was no delay between the cask impact and the fuel assembly impacts, the A-side assemblies might decrease to the 30–40 g range for their maximum accelerations, while the D-side assemblies might decrease to the 40–50 g range.

Table 3.2. Summarized Data for Trend Calculations of Maximum Acceleration Versus Delay of Initial Impact

		Parallel			Rotated		
Side	Order	0 Delay Acc (g)	R-Squared	Adj R-Squared	0 Delay Acc (g)	R-Squared	Adj R-Squared
A	1	31.0	0.876	0.863	36.2	0.617	0.583
D	1	45.7	0.748	0.712	43.9	0.773	0.741
A	2	33.3	0.902	0.880	30.7	0.644	0.572
D	2	49.9	0.797	0.729	41.6	0.776	0.701
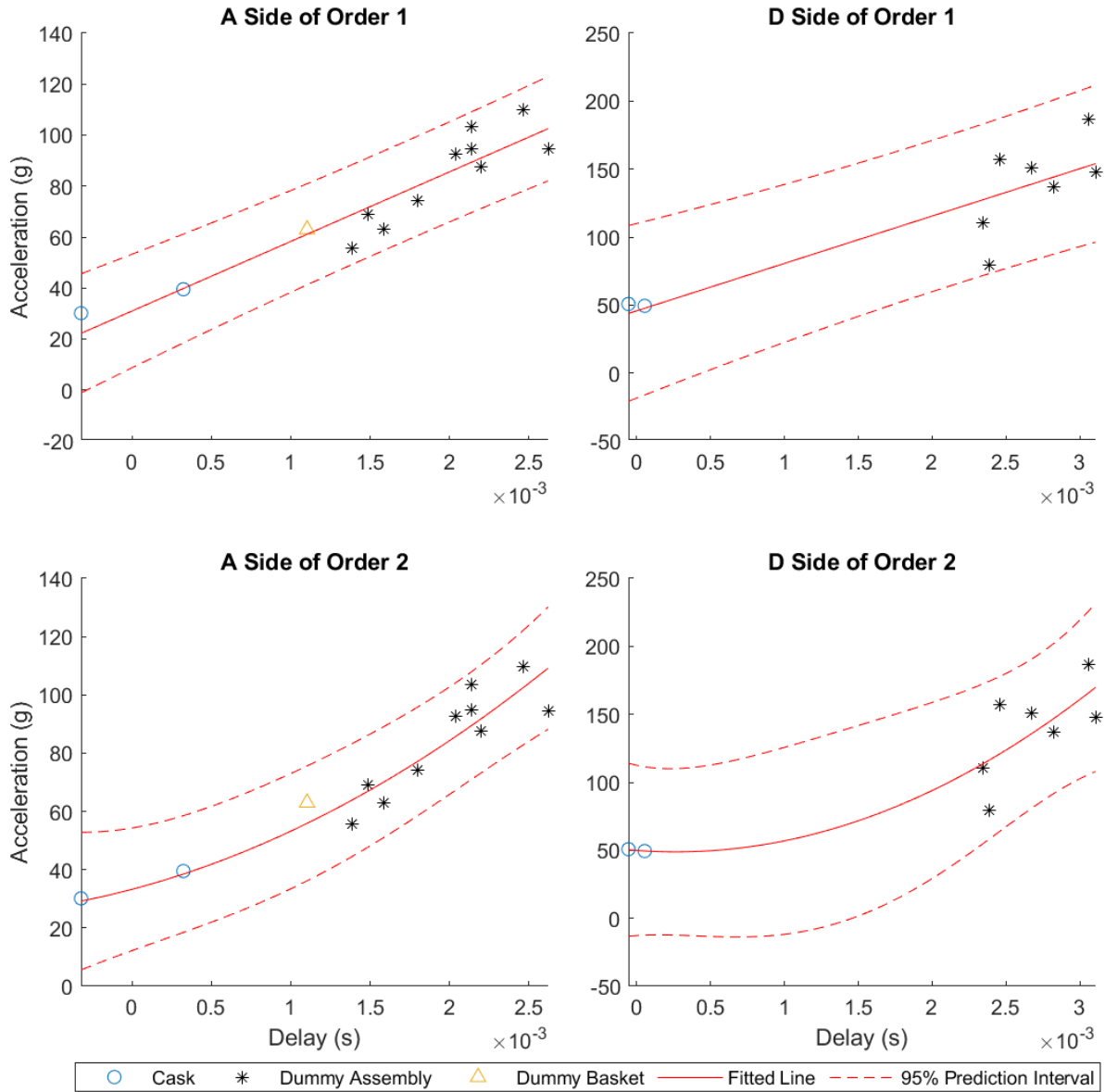
Figure 3-3. Acceleration of First Impact Versus Delay from the Cask Impact for the Parallel Drop
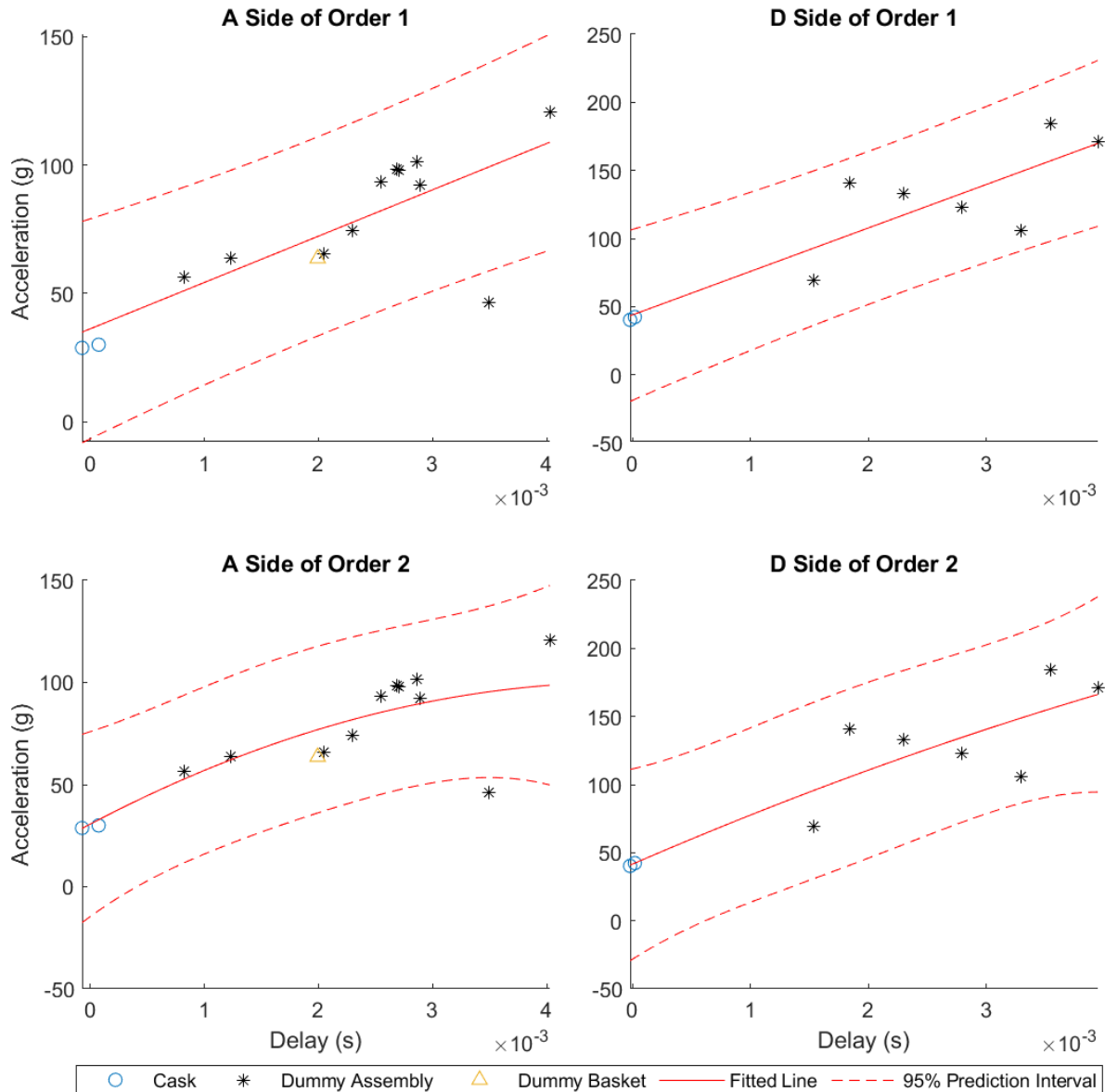
Figure 3-4. Acceleration of First Impact Versus Delay from the Cask Impact for the Rotated Drop

The main conclusion of this data study is that the delay in impact response of the transducers implies that gaps form between fuel assemblies and the basket during freefall. The data are shown with 1st order and 2nd order curve fits to define a 95% prediction interval. This information is useful for defining the general 30 cm cask drop initial conditions. Gaps should exist, but there is clearly a natural variation in gaps for each fuel assembly. The topic of including gaps is discussed in Section 7.

3.2 Basket Behavior in Cask Model

During a package drop, a portion of the kinetic energy is converted into strain energy as the impact limiters, cask, basket, and SNF deform. The strain energy is one means of evaluating the transmission of loads in a structure; a body that has a high strain energy has effectively absorbed a greater portion of the kinetic energy than the rest of the structure.

The peak internal energy in selected parts of the package from the BAM 1/3 scale cask 30 cm drop model from Section 2.1.3 are presented in Table 3.3. The impact limiters constitute a huge majority of the

internal energy in the package, which is intrinsic to their purpose and design. The remaining components account for relatively little. The internal energy of the basket is similar to the combined internal energy of the surrogate assemblies and is a non-negligible fraction of the total non-impact limiter components, at about 16%. This suggests that the basket influenced the impact dynamics inside of the cask. Note that the table reports peak internal energy values regardless of time. The sum of the energy in individual components exceeds the value reported for the entire package because the timing is different.

Table 3.3. Peak Internal Energy in the BAM 30 cm Drop Model

Component	Peak Internal Energy (J)
Entire package	17,800
Impact Limiters	17,750
Cask	87.1
Basket	20.9
Surrogate assemblies (total)	26.6

A sensitivity study was performed to investigate the effect of the basket, by adjusting its Young's modulus from a quarter of its nominal value to fourfold. Increasing the basket stiffness decreased its peak internal energy as well as the peak and average surrogate assembly acceleration, as shown in Figure 3-5. At first this seems counterintuitive, because it could be imagined that greater internal energy of the basket would mean a greater "cushioning" effect on the surrogate assemblies during an impact. However, as the basket stiffness decreases, the basket displaces more toward the impact surface, effectively increasing the gap between the surrogate assembly and the basket. This leads to more pronounced secondary impacts and higher surrogate assembly accelerations. The uniformity of the surrogate response throughout the basket is also dependent on the basket stiffness; the standard deviation (S.D. in the figure) of the peak accelerations increases as stiffness decreases (Figure 3-5, gray line).
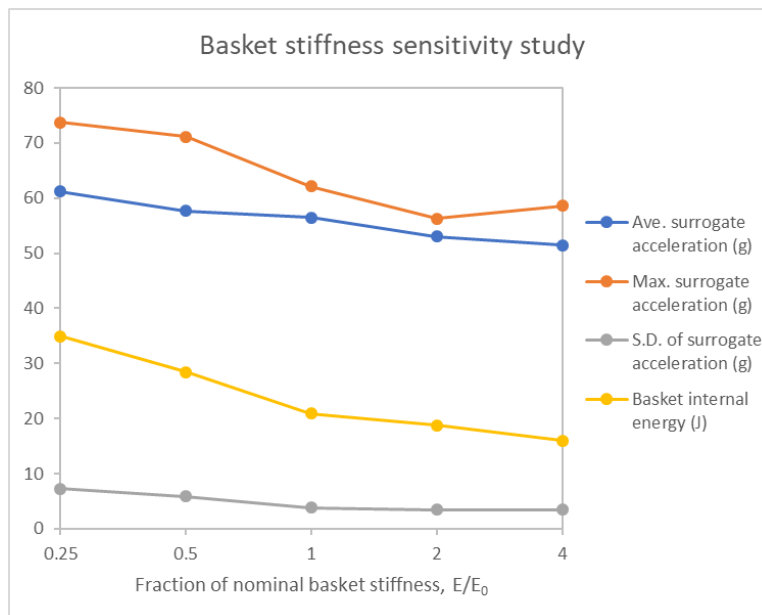
Figure 3-5. Summary of Basket Stiffness Sensitivity Study

The cask impact model also affords an opportunity to investigate the full spread of surrogate fuel assembly accelerations within the basket without the limitation of limited instrumented test data. Because the basket is a deformable structure, it is desirable to know if any "hot spots" exist where deformation of

the basket results in amplified impact loading to SNF. Figure 3-6 shows the peak surrogate assembly accelerations for each basket position in the BAM 30 cm drop model. In contrast to the values shown in Table 2.2 and Appendix A, Table A.3 and Table A.4, these values are nodal averages of acceleration, which tend to suppress acceleration due to local deformation. The surrogate assembly response throughout the basket is very uniform; no "outlier" cells exhibited significantly higher accelerations, but some cells showed notably lower acceleration. There appears to be a very slight trend toward greater acceleration in the cells distant from the impact surface, because the upper cells will exhibit more deflection than the lower cells, allowing for larger gaps to form between the basket and surrogates.

Dummy assembly acceleration, rigid body

	1	2	3	4	5	6
1	NaN	58.31	62.04	62.14	57.98	NaN
2	56.97	55.7	58.29	59.19	55.71	56.77
3	56.48	57.33	58.68	58.18	57.7	57.6
4	56.61	55.64	57.52	57.57	55.98	57.04
5	46.21	56.73	57.64	57.5	56.84	47.85
6	NaN	47.12	59.9	59.08	47.48	NaN

Figure 3-6. Peak Surrogate Assembly Acceleration (g) (Nodal Average) in the BAM 30 cm Drop Model (Non-rotated Basket) for Each Basket Position.

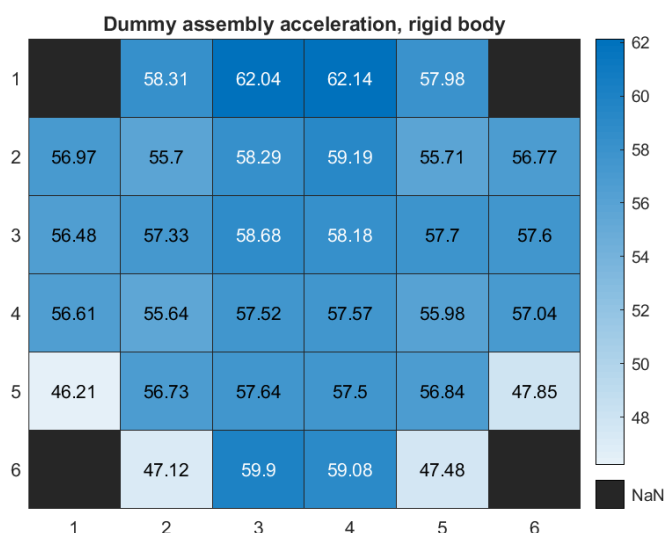The modeling results indicate that the basket affects the dynamics within the cask. This has to do with both the structural response of the basket and secondary impacts occurring between the basket and fuel assemblies. The basket deforms elastically during an impact, causing gaps to form between the fuel assemblies and basket, resulting in secondary impacts. Because the deformation is distributed throughout the basket, the intensity of secondary impacts can vary across basket cells. This study indicated that the range of fuel assembly peak accelerations were within about ±15% of the mean value, which cannot be ignored in assessments of fuel integrity. The effect of the fuel-to-basket gap during a 30 cm drop event has been characterized in a sensitivity study (in Section 5.1.2.3) and was found to have a significant effect on fuel cladding strains and grid crushing. Based on this finding, all of the analyses of fuel in this work incorporate a limiting condition where the basket-to-fuel gap is maximized.

3.3   Summary of Basket Effects in MMTT

The basket had little to no effect during the MMTT. The model architecture of Klymyshyn et al. (2018) considered the basket and cask to be essentially rigid structures. Cask motion, either recorded from the MMTT or calculated from railcar dynamics models, was applied directly as base excitation to a single fuel rod structural dynamic model. In the 2018 study, the peak cladding strain calculated with this method agreed with test data within about ±20 uE for the calculated cask motion and about ±10 uE for cask motion that was directly recorded during the MMTT. This modeling methodology achieved acceptable agreement with test data when it neglected basket effects, which demonstrates that the basket is not significant enough to require consideration in the NCT shock and vibration environment.

Klymyshyn et al. (2019) improved the single rod model by adding springs to represent interaction between the fuel rod and grid spacers. The rigid approximation of the fuel basket was maintained. Better

agreement with test data was achieved in the single rod model, although Klymyshyn et al. (2019) still reported the accuracy to be ±20 uE for the methodology as a whole.

Note that in both of these reports, the conclusion was that the basket was not significant enough to include as a structure, spring constant, or other parameter in the model. A practical judgment was made, based on the primary goal of predicting cladding strains to match test data. This does not mean that the basket has a completely neutral role in transmitting forces to the fuel assembly during dynamic excitation, just that the NCT shock and vibration loads are so small that the basket's behavior does not matter.

To put it in perspective, the westbound rail leg of transportation (the one that was fully recorded over 2000 miles) only registered an instantaneous peak of 0.3 g on the cask vertical acceleration. In contrast, the 1/3rd-scale cask 30 cm drop accelerations were 30–51 g at the cask accelerometers. For a full-scale cask the accelerations should be scaled down by a factor of 3, to approximately 10–17 g. The full-scale cask models of Section 2.2.1 predicted cask accelerations up to 25 g when considering all impact angles. So the cask accelerations of NCT shock and vibration are roughly 2 orders of magnitude smaller than the 30 cm cask drop loads.

It is concluded that the load magnitude in the NCT shock and vibration environment is sufficient to explain why the basket structural dynamic effects are not important. A peak acceleration load of just 0.3 g potentially causes less additional deformation energy in the basket than static gravity loading. The relative difference in loads compared to the 30 cm drop case (2 orders of magnitude) is sufficient to explain why the basket was negligible in the MMTT but more important in the 30 cm drop scenarios considered in this study.

3.4   Conclusions

This section considered the 30 cm cask drop test data, structural dynamic finite element models of the cask drop scenario, and the negligible role of the basket in the MMTT shock and vibration environment. The primary conclusions are that the basket structural dynamic behavior matters in the 30 cm drop, but it was negligible in the MMTT. The differences in momentum and total energy explain why the two loading condition cases are different. Structural dynamic cask drop models need to include accurate models of the basket to determine accurate loads on the fuel assemblies.

A sensitivity study showed that the average surrogate assembly accelerations are sensitive to the stiffness of the basket in the 30 cm drop scenario. Deformation of the basket leads to more pronounced secondary impacts, which tend to increase surrogate assembly loads. This suggests that the stiffness and structural dynamic behavior of baskets in structural dynamic models needs to closely match the behavior of the real system. Simplifying assumptions need to be made in such a way as to preserve the load transmission, energy absorption, and energy dissipation of the basket structure.

While not strictly a basket issue, secondary impacts are also important. The test data show that the fuel assemblies inside the cask experienced a delay in responding to cask impact. The delay varied by fuel assembly location. The variation in impact delays is associated with a variation of peak surrogate assembly acceleration of +/-15% of the mean value, which indicates a potentially significant variation in impact loads on the fuel assemblies within a single basket.

The impact delay is interpreted to be an indication of a physical gap between the fuel assembly and the basket closing and causing a secondary impact. This phenomenon (a gap developing during free fall and closing during impact) was confirmed to occur in the high-speed video clips of the SNL fuel assembly drop test where a window in the basket tube allowed for direct viewing.

This is less of a basket issue and more of a general observation of the impact physics—real SNF assemblies in a cask drop scenario are likely to experience a variable delayed impact response due to a gap condition at impact. The data suggest that the gap will be different throughout the cask. Structural dynamic models must make assumptions about the gap condition at impact, and this kind of modeling

choice is often made with conservatism in mind, such that stresses are calculated based on the most limiting gap condition. But the test data show that the gaps (and impact delays) will naturally vary throughout the cask. Gaps and secondary impacts are a real point of uncertainty in this type of stress evaluation. The gap condition could be any value within the geometrical constraints of the system. The general cask drop scenario needs to consider gap variation, gap sensitivity, or gap uncertainty in some way, and PNNL intends to include these effects in the damage model described in Section 6. For now, the best way to account for gap uncertainty remains to be determined. (Each of the models described in this study identify the gap conditions that were assumed.)

4   SNL DROP TEST ANALYSIS AND VALIDATION MODELING

The cask drop test scenario was conducted in two parts. The 3rd-scale cask drop test was conducted first (in December 2018 at BAM) to determine the shock pulse that a full-scale fuel assembly would experience in the cask drop scenario. With knowledge of the target shock pulse, single dummy assembly drop tests were conducted (in the summer of 2019 at SNL) to determine how to produce the desired shock pulse on a single fuel assembly. In 2020, an instrumented fuel assembly was dropped 30 cm at SNL in a test that achieved the target shock pulse (Kalinina et al. 2020). The experiment was designed to apply an impact load to the instrumented fuel assembly that was similar to and consistent with the cask drop scenario, without having to use a real, full size cask. The cask portion of this experiment is discussed in Section 3. This section focuses on the fuel assembly drop test.

The drop test data are valuable in their own right to help us understand what happens to a fuel assembly when it is inside a cask that is dropped 30 cm. Understanding what physically happens allows us to build accurate finite element models to predict the structural dynamic response of fuel assemblies to cask drop impact loads. The finite element method fundamentally implements the laws and theories of engineering mechanics as computer models, but the art of finite element modeling is in ensuring that all of the relevant physics are represented within the model. Validating finite element models is important because it confirms that the models apply all of the necessary physics behaviors required to reproduce the test data. Phenomena like friction, damping, and elastic-plastic material deformation are known to exist but can be difficult to accurately predict without test data to guide parameter choices. Practical finite element modeling concerns are also resolved by comparison to test data, such as selecting an adequate finite element mesh resolution. Once validated, the model can be applied to similar situations where test data are not available.

Section 4.1 describes some of the data collected from the 30 cm fuel assembly drop test at SNL that is important to the modeling. There are summaries of the transducer data (strain gages and accelerometers) and an analysis of the video data. A data correlation study was also performed on the transducer data, to identify strong or weak correlation relationships between channels. The data and analysis of data were used to inform the modeling.

Section 4.2 describes a new fuel assembly finite element model that was developed this year to include crushable grid behavior. The previous PNNL fuel assembly model did not have adequate grid compression capability to match the observed behavior of the spacer grids in the SNL fuel assembly test. The new fuel assembly finite element model is an evolution of the model in Klymyshyn et al. (2018) with the new features noted in this report. Model results are directly compared to test data using several metrics presented in several formats.

Section 4.3 concludes that the validation results demonstrate the current model is already reasonable, but it has clear room for improvement. A number of recommendations are made for refining and improving the model in future work scope. These refinements could not be completed this year because the test data were not available until late in the work cycle.

4.1   SNL 2020 30 cm Drop Data Analysis

The data for the 30 cm drop conducted at SNL used one surrogate fuel assembly and a basket tube from the ENUN-32P basket. There were 15 total accelerometer locations on the fuel rods, assembly, and basket and 2 additional ones on the platform of the drop. There were also 18 strain gage locations on the fuel rods themselves. The results shown are the filtered data, which were filtered using a six-pole, low-pass, Butterworth filter that had a half-power frequency of 300 Hz. However, before the data were filtered the data range was reduced to only focus on the drop, initial contact, and subsequent bounces. Table 4.1 shows the maximums for all the strain gages and accelerometers. Strains are measured in microstrains (uE), where 1 uE = 10^{-6} mm/mm, and accelerations are measured in g, where 1 g = 9.8 m s^{-2}. Some of

these values are different from the values in Table 4-2 of Kalinina et al. (2020) for several reasons: the PNNL bias correction was slightly different from the SNL bias correction, PNNL filtered the data while Table 4-2 is only bias corrected, and this PNNL report focuses on the initial impact pulse while the SNL report documents the full set of collected data. Some relatively large strain gage readings occur after the initial shock pulse as the system rebounds.

Table 4.1.   Summarized Maxima for All Strain Gages and Accelerometers

Strain (uE)		Acceleration (g)	
Sensor	Absolute Max	Sensor	Absolute Max
SG1-0	929	A1Z	39.6
SG1-90	301	A2Z	52.8
SG1-225	507	A3Z	43.5
SG2-0	533	A4Z	67.7
SG2-90	132	A5Z	55.5
SG3-0	777	A6Z	54.3
SG4-0	440	A7Z	84.2
SG4-90	184	A8Z	59.3
SG4-225	297	A9Z	66.1
SG5-0	371	A10Z	82.1
SG5-90	109	A11Z	56.3
SG6-0	599	A12X	11.0
SG7-0	639	A12Y	35.2
SG8-0	988	A12Z	118
SG8-90	195	A13X	18.1
SG8-225	628	A13Y	46.7
SG9-0	434	A13Z	76.3
SG9-90	105	A16X	12.0
SG10-0	1430	A16Y	35.4
SG11-0	736	A16Z	53.1
SG12-0	1010	A17X	7.40
SG13-0	431	A17Y	57.8
SG14-0	418	A17Z	101
SG15-0	403	A18Z	1.00
SG16-0	406	A19Z	1.50
SG17-0	462		
SG18-0	595		

Most of the strain gages experienced 100s of microstrains as the maximum strain, but this maximum was not necessarily right at the initial impact. Some strain gages showed a clear initial peak (either positive or negative), others showed a double peak or a wider time-response instead of a perfect peak. In all cases, the 0° strain gage experienced a larger than the respective 90° and 225° gages. SG10-0 and SG12-0 saw the largest and second largest strains, and both strain gages were placed in the middle of the longest spans. Figure 4-1 shows the strain response graph over the course of the drop for SG10-0.

For the accelerometers, the highest acceleration of 118 g was experienced by A12Z, located on the bottom nozzle of the fuel assembly and shown in Figure 4-2, and the second highest acceleration of 101 g was seen by A17Z, located on the basket on the same side as A12Z. The respective accelerometers on the opposite end, A13Z and A16Z, showed much lower accelerations of 76.3 g and 53.1 g. In fact, A17Y, 90° off vertical, showed a higher acceleration than A16Z. This difference could be due a slightly uneven drop, causing one side to impact before the other.
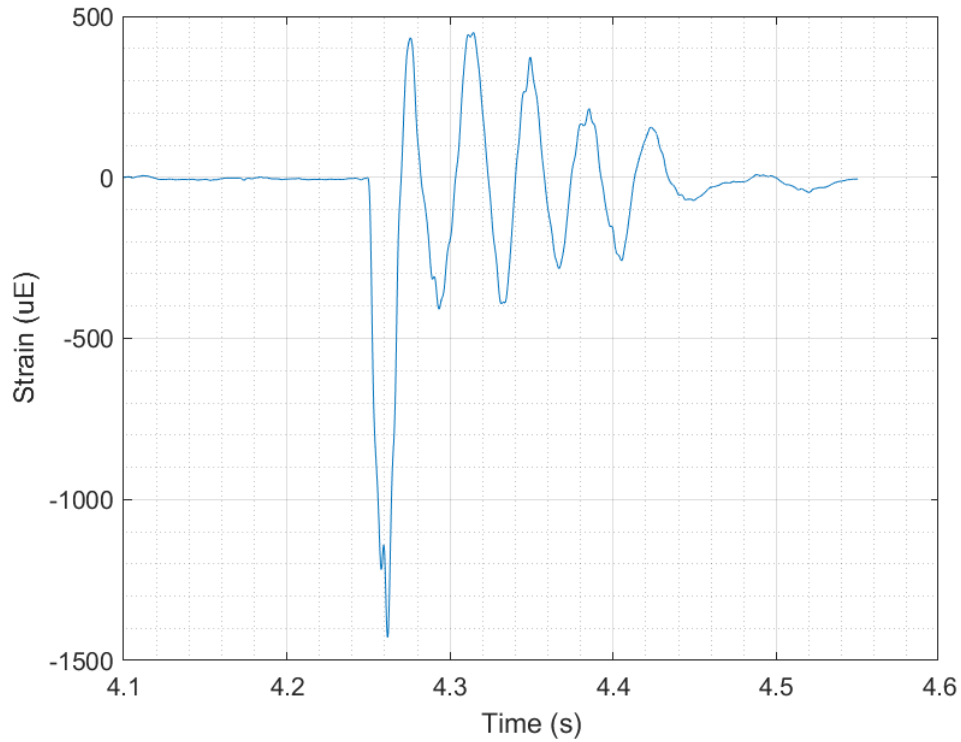
Figure 4-1. SG10-0 Filtered Strain Response (in uE)
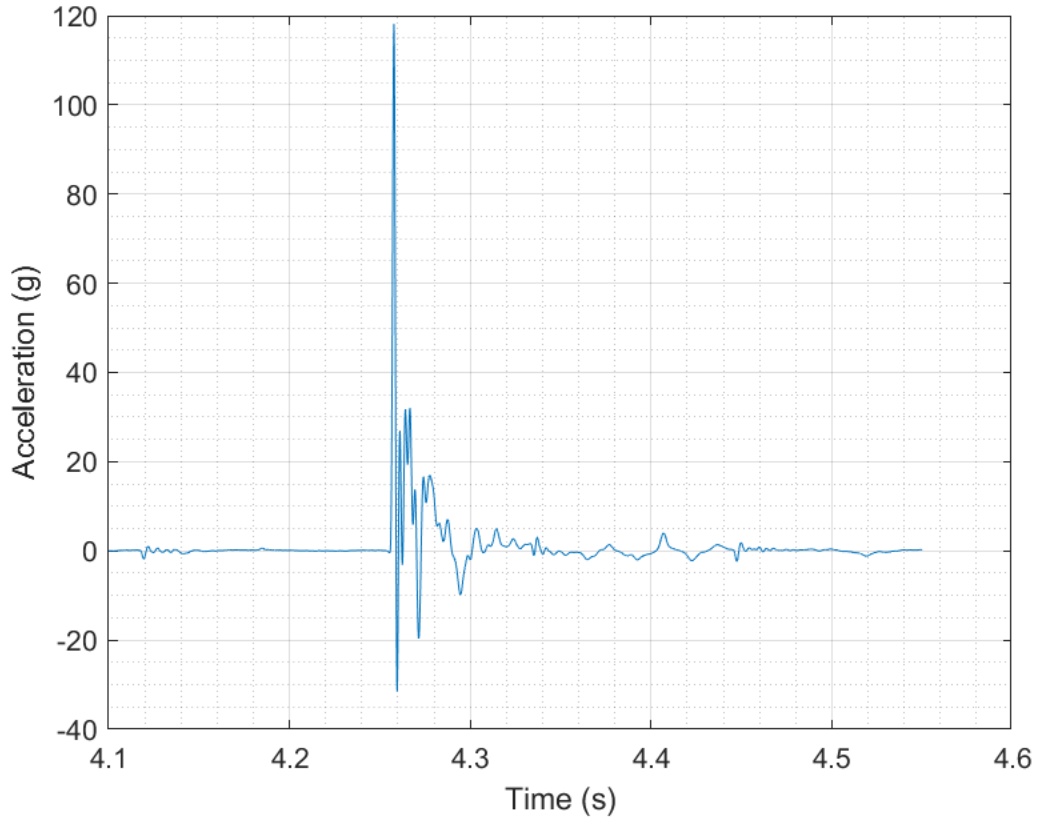
Figure 4-2. A12Z Filtered Acceleration Response (in g)

The two highest fuel rod accelerometers were A7Z, shown in Figure 4-3, and A10Z, both located at grid spacer locations. Besides those two, the rest of the fuel rod accelerometers experienced accelerations less than 70 g. A1Z was the accelerometer that had the lowest maximum magnitude of 39.6 g. The two platform accelerometers did not have any significant accelerations; A19Z reported the higher acceleration at 1.50 g. A19Z was on the same side as A17Z.
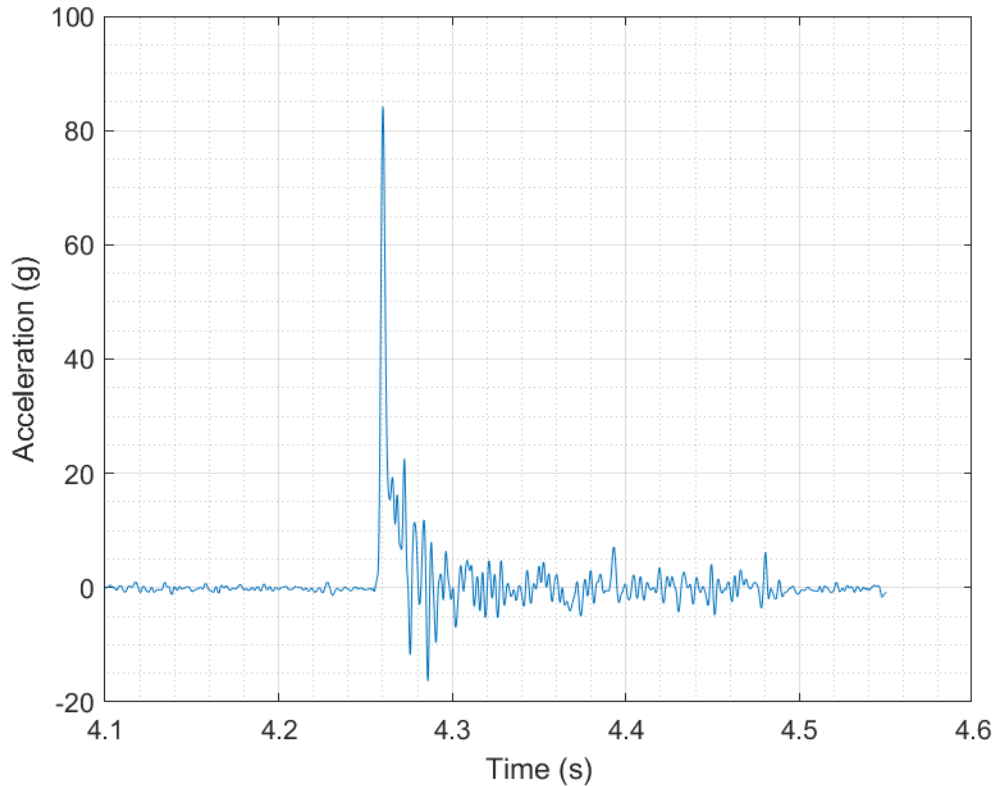
Figure 4-3. A7Z Filtered Acceleration Response (in g).

4.1.1   Video Analysis

Aside from the instrumented fuel assembly, high-speed cameras were used to film different portions of the assembly system during the drop. The video setup had several fiducial reference markers that had a Secchi disk pattern to help track the position of the assembly and basket. However, no such markers were used on the fuel assemblies; positions on the assemblies were tracked through the video and then reviewed after analysis to ensure that no significant erroneous motion was captured. Two virtual markers were used, labeled as "top" and "bottom." For future drop tests it is recommended that target markings be added to the fuel assembly for video tracking and specifically to each visible fuel rod in the mid-span to aid in video processing rod motions and rod-to-rod contacts. A dot from a permanent market would be sufficient.

The motion data that could be extracted from the video was then used to find the velocity and acceleration of the rods, assembly, and basket. The acceleration was further filtered using the same filter that was used for the accelerometer data, and the two filtered data sets were compared. In total, there are three videos. The first video, with the results shown in Figure 4-4, is a video from the "top" of the fuel assembly. The top of the fuel assembly, in this context, does not relate to the top and bottom distinctions of the fiducial markers; the top of the fuel assembly is in reference to the vertical position in which it sits when placed in a nuclear reactor. This top of the fuel assembly is on the south side of the system, i.e., to the far right when placed horizontally. The second video, with results shown in Figure 4-5, is also from the south side of the system but situated more inwards. It shows the basket with a window cutout to also show the motion of the fuel rods. The last video, with results shown in Figure 4-6, is from the north side of the system, also situated inwards toward the center. The basket with a window cutout for the fuel rods is shown in this video as well.

The maximum fuel rod acceleration was from the second video at 119 g, much higher than the 84 g from the accelerometers. This maximum acceleration was on a fuel rod that experienced rod-to-rod

contact, limiting its motion and causing the acceleration to spike. The rod-to-rod contact can also be seen in the position graph. Interestingly, there is no clear evidence of rod-to-rod contact in the accelerometers when comparing the maximums. None of the other rods analyzed in the videos showed rod-to-rod contact, and the next largest acceleration was around 65 g, on par with the accelerometer results.
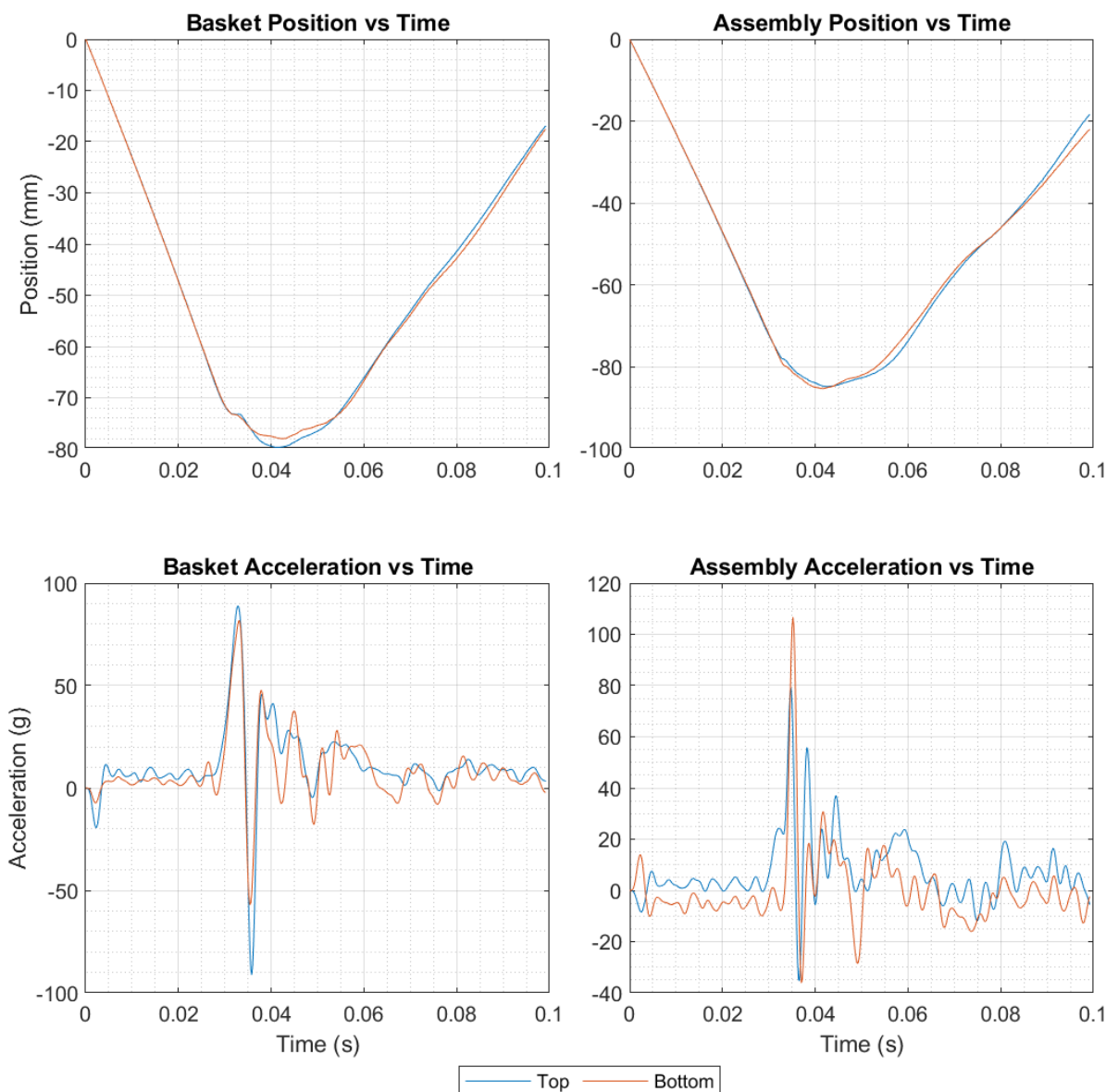
Figure 4-4. Position and Acceleration Graphs for the Top of the Fuel Assembly and Basket Video, on the South Side of the System

The maximum assembly acceleration was from the first video at 107 g, which is on par with the maximum fuel assembly accelerometer. However, this acceleration from the videos was measured on the same side as A13Z, which has a maximum acceleration of only 76 g. However, A13Z was placed on top of the assembly, and the maximum video acceleration was from the bottom fiducial markers. Using the top fiducial marker's position only led to a maximum of around 80 g, in line with the results from the accelerometers. With these comparisons, there seems to be a correlation between the acceleration and the position on the assembly, whether top or bottom. This correlation could be due to grid spacer deformation, where this deformation acts as a shock absorber for the top of the assembly; the bottom of

the assembly, however, would not benefit from this deformation, and thus would experience higher accelerations. The modeling sections discuss the behavior of the fuel assembly in more detail.

The maximum basket acceleration was from the second video at 94 g, comparable to the 101 g from the accelerometers. However, the maximum accelerometer was on the north end of the assembly, while the maximum video acceleration was on the south end closer to the center. The comparable accelerometer, A16Z, only had 53 g, more than 40 g lower than the video. Video from the very south end also shows a maximum acceleration of about 91 g. Discovering the reason behind this discrepancy is beyond the scope of this video analysis.
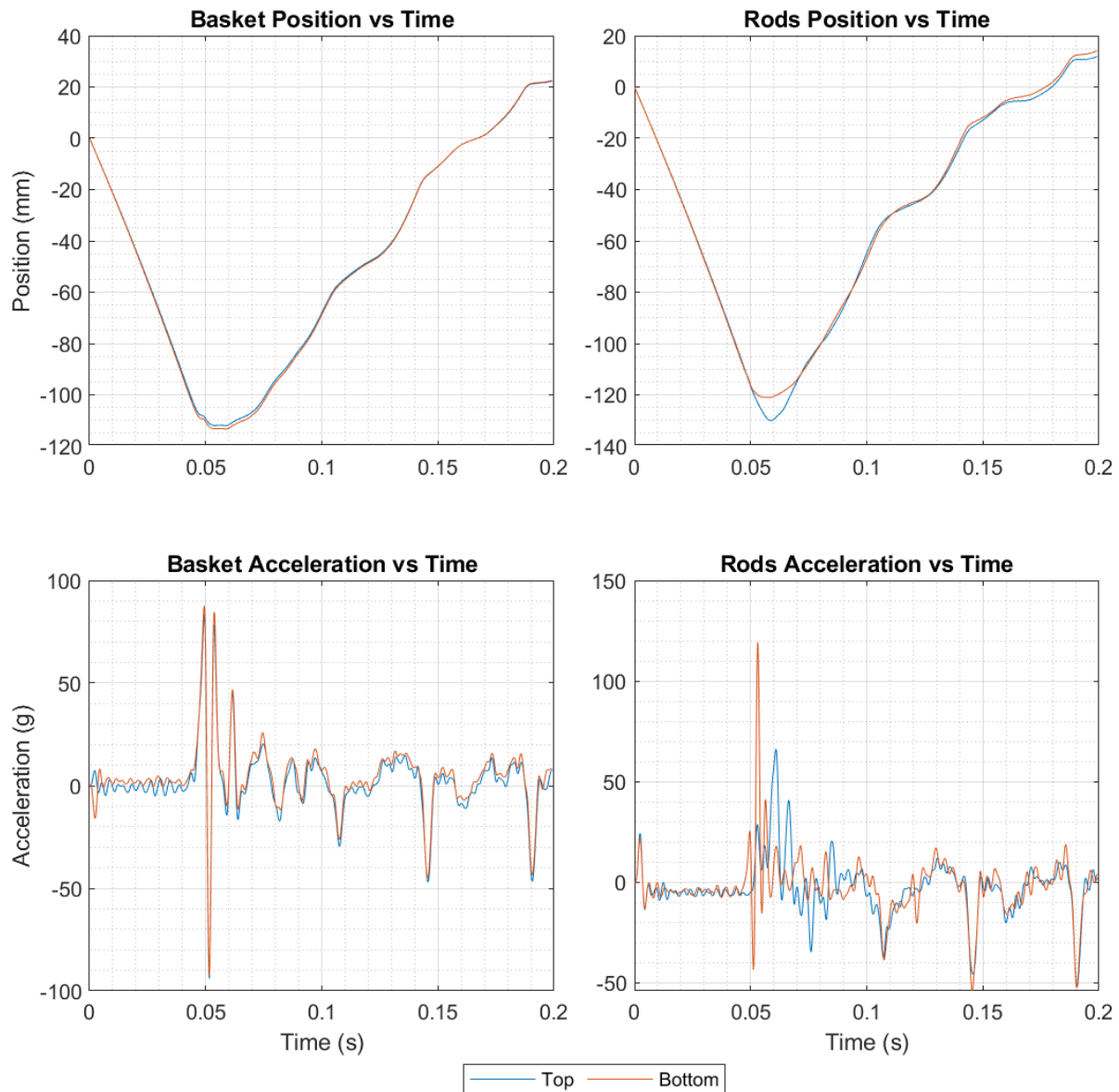
Figure 4-5. Position and Acceleration Graphs for the Window Cutout of the Basket and Fuel Rods, on the South Side of the System
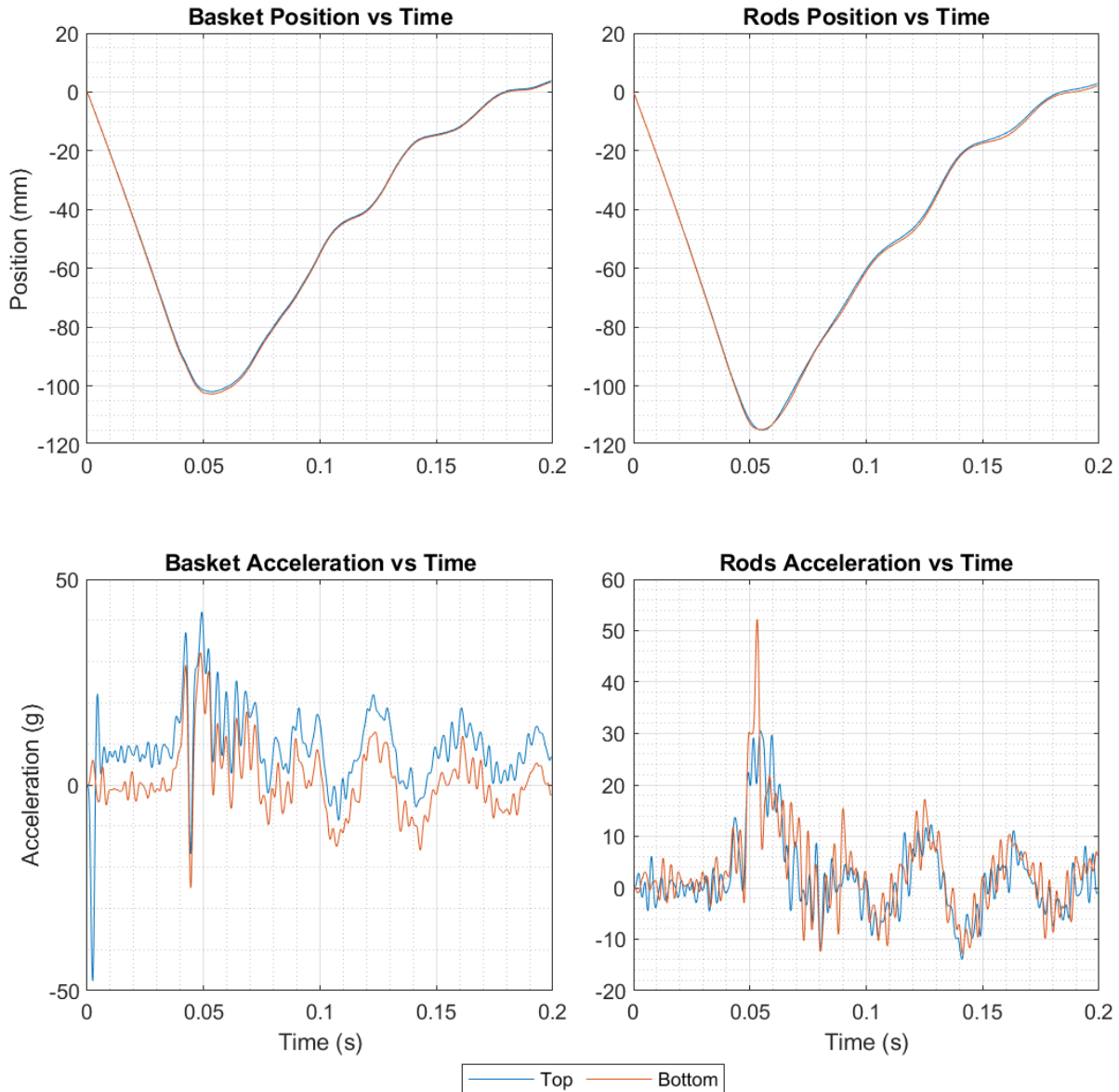
Figure 4-6. Position and Acceleration Graphs for the Window Cutout of the Basket and Fuel Rods, on the North Side of the System[1]

4.1.2   Fuel Assembly Drop Test Data Correlation

Another method of comparing the instrumented data is to calculate correlation matrices for all the accelerometers (Figure 4-7) and strain gages (Figure 4-8). The strain gages and accelerometers had different sampling rates, so to avoid any errors caused by aliasing during down sampling, these two data sets were not correlated.

Overall, in the accelerometer correlation matrix, a few patterns stand out. First, the fuel rod accelerometers have some strong correlations among themselves. Second, the fuel rod accelerometers have moderate correlations with A12Z and A16Z, and less strong correlations with A13Z. A17Z does not

---

[1] The initial acceleration of the "top" fiducial marker in the basket is an artifact of the video analysis and not a physical acceleration.

seem to have any significant correlations with the fuel rod accelerometers. Third, the fuel assembly accelerometers are not significantly correlated with each other. Fourth, the fuel basket accelerometers are also not well correlated with each other. Fifth, if there is a strong correlation, the correlation is most likely positive, meaning that the two data sets have motions in the same direction. Only A16X has significant negative correlation with several other accelerometers, meaning the two accelerometers trend in opposite directions. All other strong negative correlations between two accelerometers are localized and do not necessarily follow a pattern. With these five patterns in the correlations, it seems that the fuel rod and fuel assembly local motions are not strongly influenced by the basket motion.

While the rigid body motion of the fuel assembly and basket has to be similar due to the physical constraints of the system, this correlation analysis of the accelerometer channels indicates that local accelerations are significantly independent of each other. In the correlation analysis of the MMTT data it was noted that the frequency range significantly affected correlation. PNNL concludes that local behavior of individual fuel rods is important to understand to close the stress profiles knowledge gap. The test data supports the conclusion that the variation of loads throughout a fuel assembly and the variation of loads on fuel assemblies throughout a cask are both significant and need to be understood.

As an aside, the accelerometers on the ground do have some moderate correlations with fuel rod accelerometers, but no conclusions can be drawn from these correlations.

As for the strain gages, significant correlations are not confined to only positive values. There are strong correlations both in the positive and negative directions. Overall, there also seems to be a stronger correlation between the strain gages than between the accelerometers. The average magnitude of correlation is 0.31[1] between all the strain gages versus 0.26[2] between all the accelerometers. Although 0.05 is not a large value in a singular correlation, as an average among more than 20 data sets, it does show a measurable difference. This difference is likely because the strain gages are only on the fuel rods, while accelerometers include data from many other sources. However, using only the accelerometers from the fuel rods, the accelerometer correlations increase to 0.49, significantly higher than the strain gages. As for individual correlations between strain gages, there does not seem to be an easy pattern to follow like for the accelerometers. However, there are some strong correlations between co-located strain gages, meaning they are in the same horizontal location on the fuel assembly but vertically displaced. A good example is the combination of SG1-0, SG4-0, and SG8-0. There also seems to be a pattern of strong negative correlations between the 0°, 90°, and 225° strain gages in the same location.

---

[1] This average does not include self-correlations, which are always equal to unity. Including the self-correlations increases the values artificially.

[2] This average does not include the accelerometers on the ground. Including A18Z and A19Z, however, lowers the correlation by 0.007.
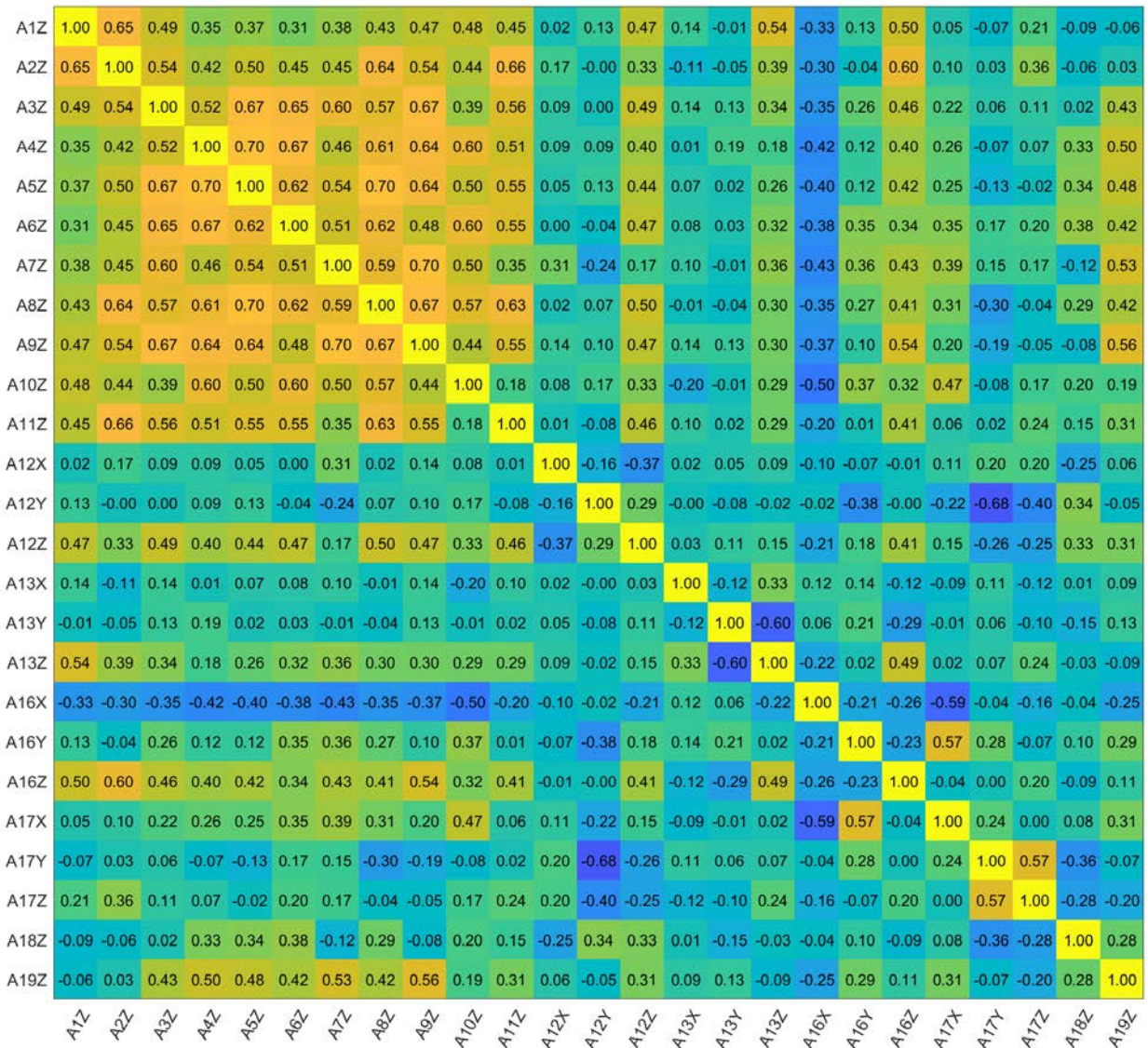
Figure 4-7. Correlation Matrix of All Instrumented Accelerometers Using the Filtered Data
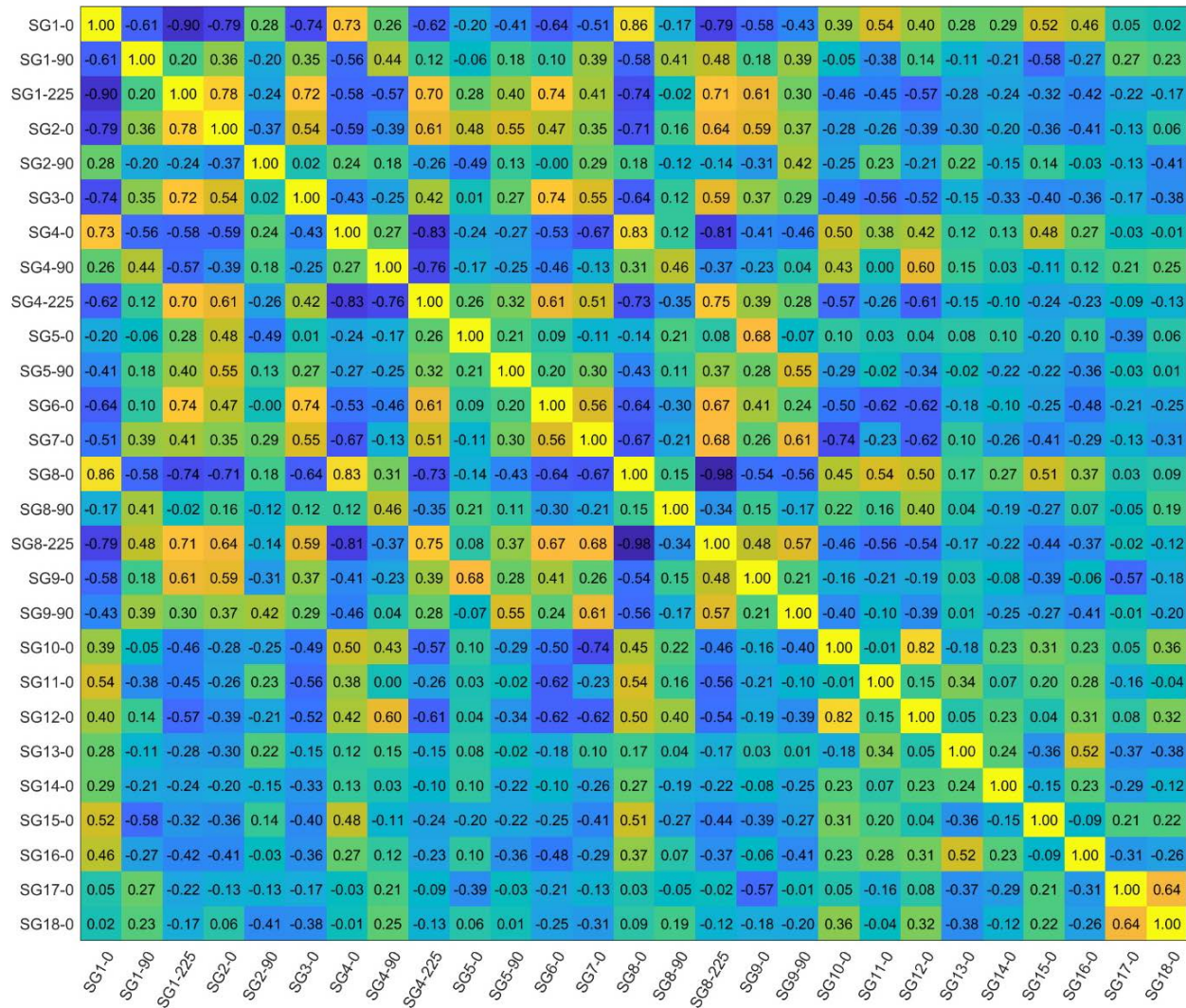
Figure 4-8.   Correlation Matrix of All Instrumented Strain Gages Using the Filtered Data

4.2   Crushable Grid Fuel Assembly Model Validation

A new, crushable spacer grid model was developed for this study. The previous PNNL fuel assembly model used a defeatured and simplified spacer grid model that was represented by shell elements. The grid worked reasonably well in applications where the grid maintained its original shape, and under extreme impact loads it exhibited a racking deformation mode that resembled realistic spacer grid buckling. In the very low magnitude loads recorded during the MMTT, it was discovered that the shell elements of the grid needed a small amount of stiffness damping to avoid some spurious behavior. Klymyshyn et al. (2018) demonstrated that the old model agreed with MMTT test data, but PNNL recognized that a new grid model was needed to calculate grid permanent deformation that occurs during the 30 cm drop. The old grid was capable of calculating grid impact forces in the 30 cm drop scenario, but it could not match the grid deformation behavior from testing. This new grid is needed to calculate spacer grid response in cask drops of 30 cm or higher.

4.2.1   Model Description

An LS-DYNA model of the 17x17 PWR fuel assembly used in the SNL assembly drop test (Kalinina et al. 2019) was developed (Figure 4-9) based on previous full fuel assembly models developed for

analysis of the MMTT (Klymyshyn et al. 2018). The model presented in this work follows the same overall structure and geometry, with the exception of the spacer grids, which are designed in the model to realistically buckle and deform. In contrast, previous fuel assembly models used a coarse representation of the spacer grids that did not attempt to resolve such behavior during lateral loading. This was not necessary for modeling of the MMTT, because the loads were too low to induce any meaningful grid deformation. On the other hand, the SNL assembly drop clearly demonstrated that grid crushing can occur during a drop event. Grid crushing is important to model because the grids are part of the load path to the fuel in a lateral impact. A grid that buckles and crushes will tend to convert more of the kinetic energy of a lateral impact into elastic and plastic strain energy than a grid that does not. In addition, as a grid crushes, the fuel rod pitch decreases, effectively changing the boundary conditions of the fuel rod.
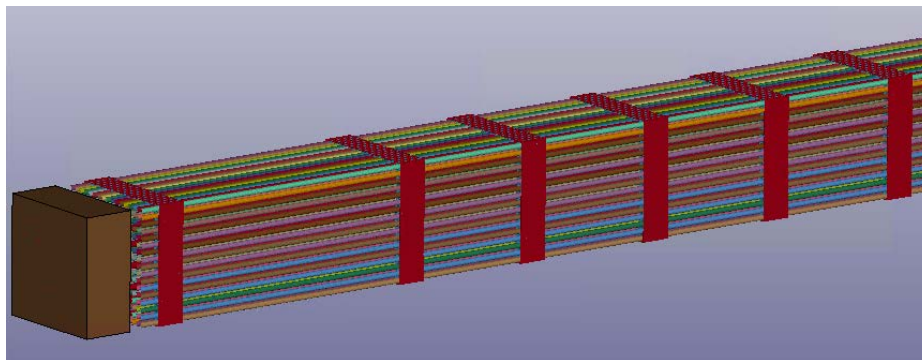
Figure 4-9. Fuel Assembly Model with Crushable Grids

Grids are complex structures that would require a significant amount of mesh detail and computational resources to model with perfectly precise geometry. Previous models (here referred to as the "MMTT grid" model) used coarse shell elements to represent the grid (Figure 4-10, left), which precludes buckling behavior. In contrast, this model (referred to as the "crushable grid model") uses grids constructed from beam elements (Figure 4-10, right)—four elements to each side of a grid cell. It was found that this provided realistic grid buckling behavior without detailed modeling of the grid geometry. Instead of directly modeling geometric details such as slots and spot welds, representative elastic modulus, yield strength, and tangent modulus of the grid material are selected to produce the correct amount of buckling and residual deformation. The discrete springs used to represent the grid springs and dimples in each cell are retained from the previous model. Refer to Appendix B for additional details on the crushable grid fuel assembly model.

Note that this approach to grid modeling relies on test data from a specific grid design. Grid impact compression behavior is commonly tested by fuel vendors for use in in-reactor seismic analyses. Grid impact behavior is known to be design-dependent, nonlinear, and when a critical buckling limit is exceeded grids can exhibit relatively unpredictable racking deformation. In an operating nuclear reactor, unpredictable rearrangement of the fuel rods is not acceptable for safety. In a SNF transportation application, the fuel assembly deformation is limited by the walls of the basket. The deformation will be more predictable inside the fuel basket, and the level of precision necessary to calculate fuel rod loads is believed to be relatively low. The plan is to first validate the grid model to the observed grid behavior, and then look for ways to generalize the grid model for application to other grid designs. PNNL is planning to perform mechanical tests on other grid designs to help expand the applicability of the crushable grid model in the future.
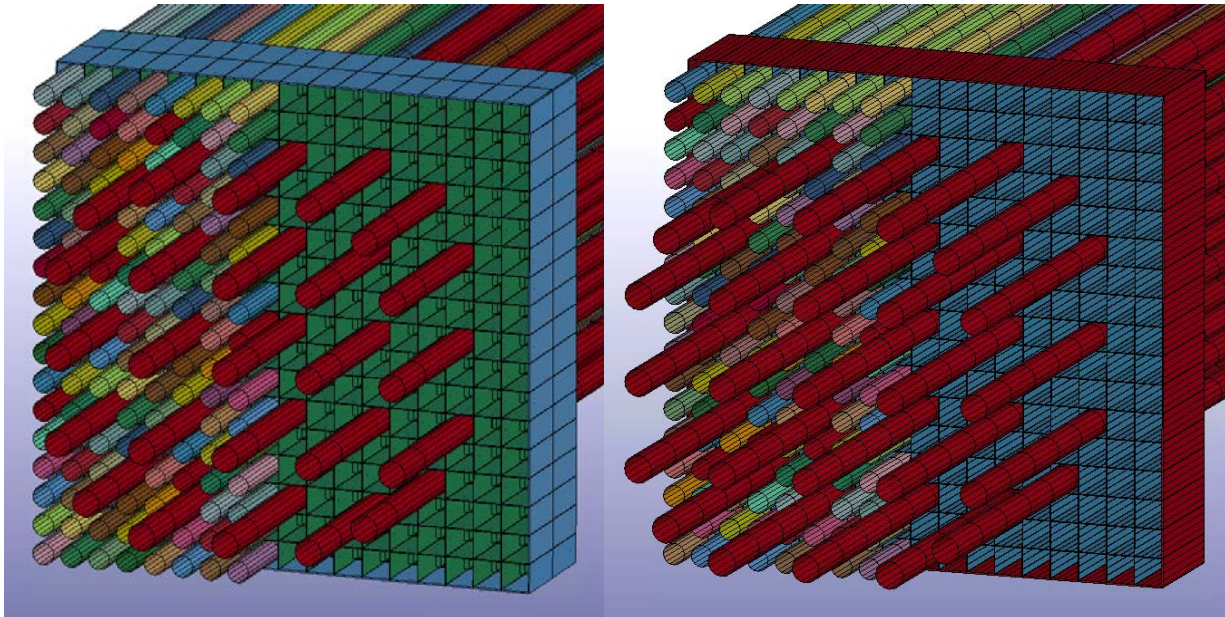
Figure 4-10. Comparison of Grid Spacers Between the MMTT Grid Model Using Coarse Shell Elements (left) and the Crushable Grid Model Using Finer Beam Elements (right). The top nozzle and some fuel rods are hidden for illustrative purposes.

Like the validation study of the BAM 30 cm cask drop test, efforts were made to accurately match the drop conditions of the SNL 30 cm fuel assembly drop test in the finite element simulation. The basket cell used in the test was modeled as a rigid body to which motion was prescribed based on analysis of the high-speed video (Section 4.1.1). Position versus time data from the north and south window videos were used to estimate the translation and rotation of the basket CG (Figure 4-11). Accelerometer and strain gage data from the test showed a 6 ms delay between the north and south ends of the basket, which was accounted for in the model by introducing a slight angle to the drop (about 0.2°). The video was also used to estimate the gap between the bottom of the fuel assembly and the basket floor, approximately 4 mm.
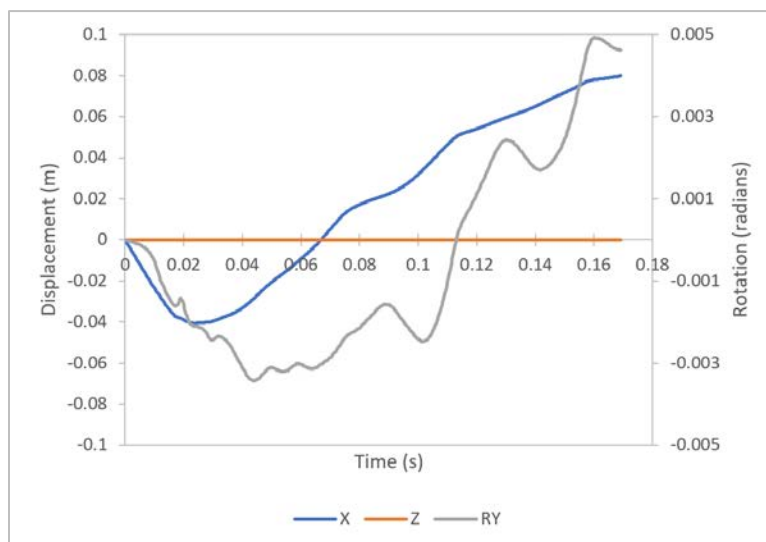
Figure 4-11. Motion Time History Applied to Basket in the SNL Assembly Drop Model

4.2.2 Model Validation Results

The response of the model in the SNL assembly drop was compared to four sets of test data: fuel assembly accelerometer data, fuel rod strain gage data, fuel rod deflections, and grid residual deformations. Each of these topics is discussed in turn.

Accelerometers mounted on the top and bottom nozzles (A13Z and A12Z, respectively) showed good agreement with the model output (Figure 4-12). The peak accelerations in the model for the top and bottom nozzles were 79.3 g and 106.7 g, compared to 76.3 g and 118.1 g in the test, or within 10%. This provides confidence that the ends of the fuel assembly were subjected to similar loads. The bottom nozzle was subjected to higher accelerations and strains in both model and test, possibly due to the slight angle of the drop. Note that the model results show a longer duration of response than the test data, which is an indication that damping and energy dissipation in the model are too low relative to the test conditions. PNNL recommends studying the data in more detail to establish realistic damping parameters.
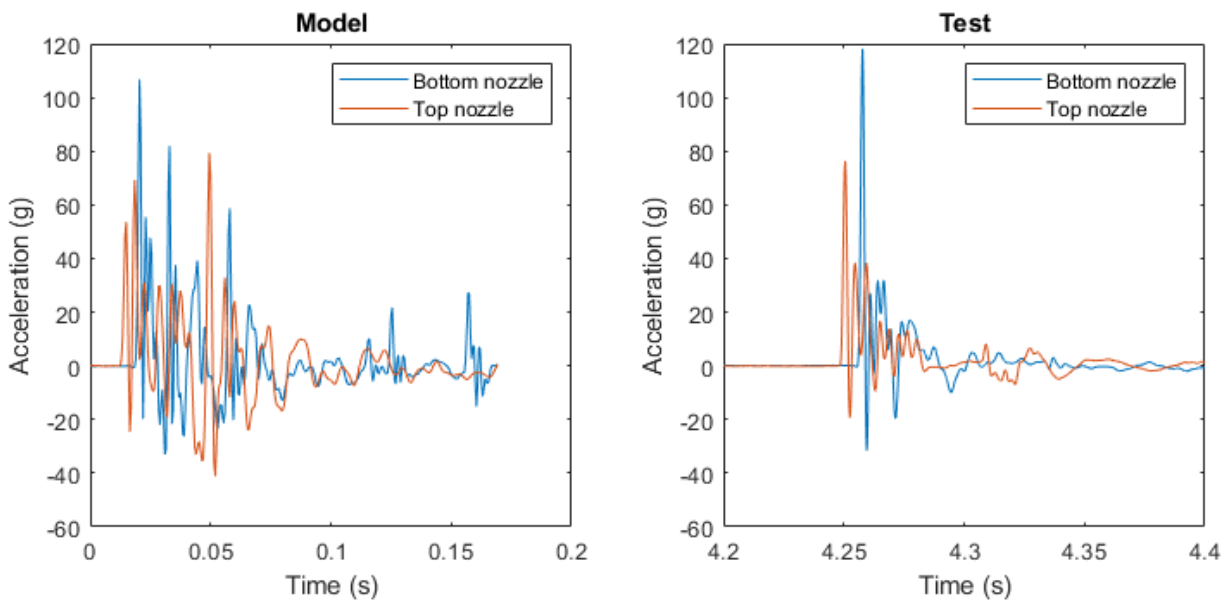
Figure 4-12. Comparison Between Top Nozzle and Bottom Nozzle Acceleration in the Model and Test

Accelerometers mounted on the fuel bundle (A1Z-A11Z, depicted with peak values in Figure 4-13) showed good agreement with the model output compared to the peak nodal average accelerations of the fuel rods in the test. The average of the peak values of A1Z-A11Z was 60.1 g, which agrees well with the average peak acceleration of the instrumented rods in the model, at 55.4 g, within 8% of the test average. This concurrence suggests that the dynamic behavior of the fuel assembly model is representative of the as-tested assembly. Figure 4-14 shows the nodal average accelerations for all 264 fuel rods in the fuel assembly model. Most of the fuel rods fell between 45 and 62 g, while the bottom two rows had accelerations up to 81.8 g due to their proximity to the impact surface.

SNL Test (Filt. 300 Hz)	39.55 g	52.80 g	43.52 g	56.34 g	82.06 g	66.07 g	59.29 g	84.19 g	54.35 g	67.75 g	55.53 g	60.13 g
	A1	A2	A3	A11	A10	A9	A8	A7	A6	A4	A5	Average
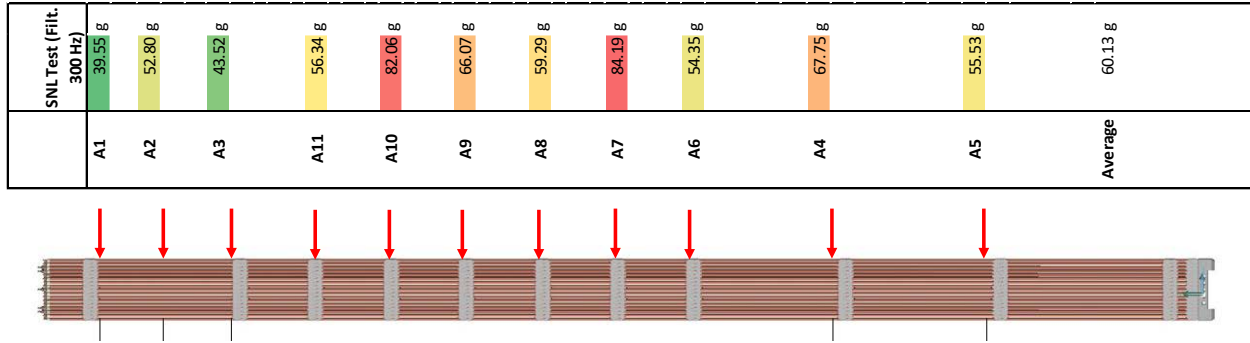
Figure 4-13. Peak Accelerations Measured on the Fuel Bundle in the SNL Assembly Drop Test
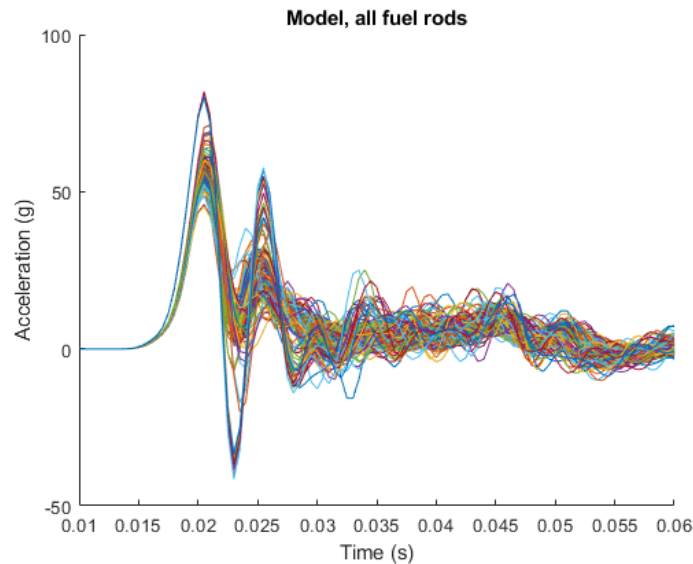
Figure 4-14. Nodal Average Accelerations for All 264 Fuel Rods in the Fuel Assembly Model

Comparisons of strain gage data from the test and strains extracted at corresponding locations in the model showed a mixed level of agreement, as depicted in Figure 4-15. The model predicted the peak strain gage location in the same location as the test, in the bottom span (SG10). However, the model predicted a higher strain than was observed in the test (1806.9 uE versus 1428.4 uE, a difference of 26%). The model overpredicted the strain for every strain gage location by an average of about 500 uE. Possible reasons for this discrepancy are discussed in the conclusion of this section.

	SNL Test (Filt. 300 Hz)	Model (Filt. 300 Hz)	Model (Filt. 100 Hz)
SG1/4/8	988.4 uE	1453.5 uE	1485.3 uE
SG2/5/9	533.4 uE	805.6 uE	597.4 uE
SG18	594.9 uE	836.4 uE	536.5 uE
SG17	461.6 uE	798.7 uE	439.4 uE
SG16	405.6 uE	849.2 uE	366.9 uE
SG15	402.9 uE	941.1 uE	447.3 uE
SG14	418.0 uE	946.6 uE	537.9 uE
SG13	430.6 uE	947.2 uE	588.5 uE
SG12	1006.7 uE	1633.2 uE	1379.0 uE
SG3/6	776.8 uE	1345.3 uE	1097.8 uE
SG11	735.7 uE	1600.6 uE	1309.9 uE
SG7	638.6 uE	1325.8 uE	1111.1 uE
SG10	1428.4 uE	1806.9 uE	1706.0 uE

Figure 4-15. Comparison of Peak Strain Gage Values Measured in the SNL Assembly Drop Test and Calculated in the Fuel Assembly Model

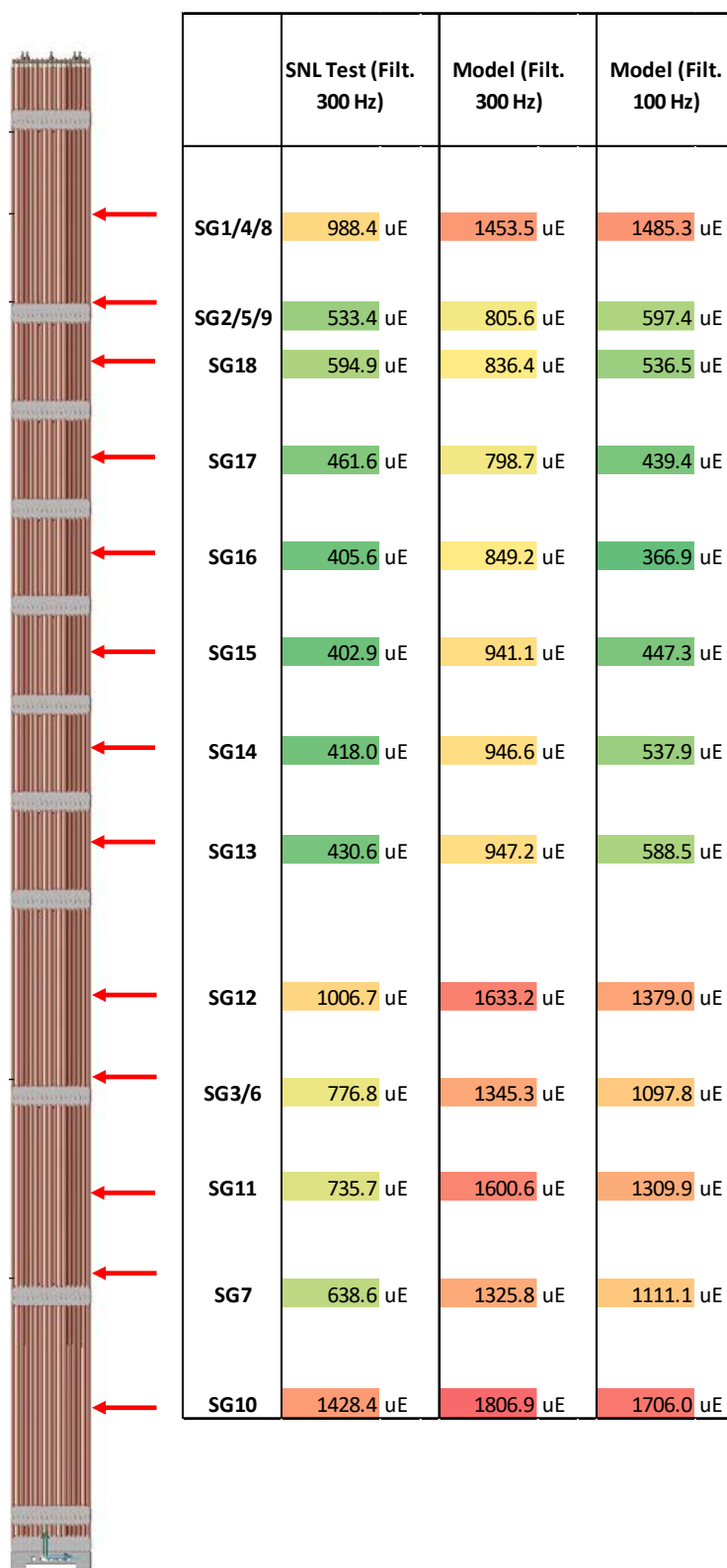Figure 4-16 shows a snapshot of the model corresponding to the moment of maximum fuel rod strain, which was 2652.9 uE. This is 47% higher than the value at the model's strain gage locations. The maximum fuel rod strain occurred in the grid adjacent to the bottom span. Though the maximum strain occurred at a location other than the strain gage locations in the test, it was unavoidable because this area is inaccessible to instrumentation. The cutaway in Figure 4-16 shows that the fuel rods positioned above guide tubes exhibited slightly greater strain, but for the most part, the strain is distributed uniformly throughout the fuel bundle.
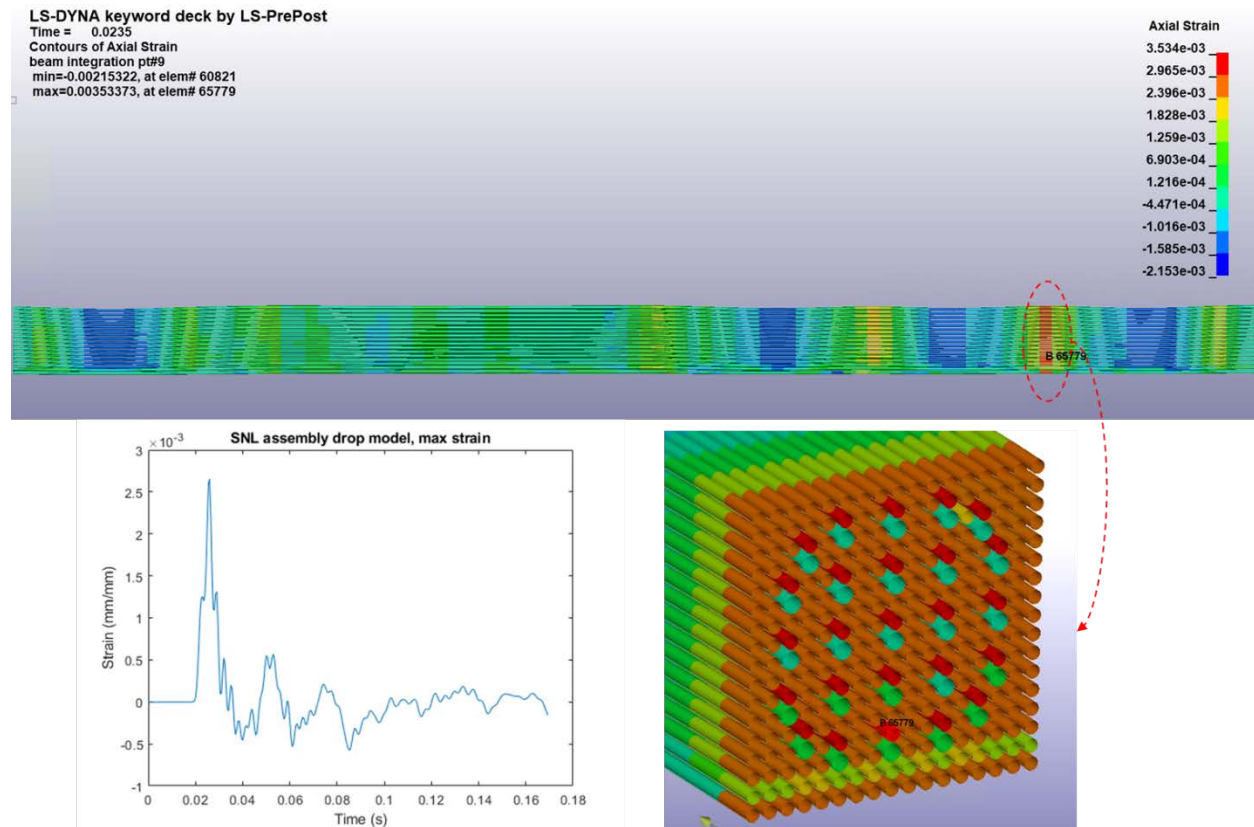
Figure 4-16. Axial Strain Fringes for the Fuel Rods in the SNL Assembly Drop Test (top), with a Cutaway Showing the Location of Maximum Strain (bottom right), and Time History of the Maximum Strain Element with a 300 Hz Low-pass Filter Applied (bottom left). The strain fringes are shown without filtering.

Fuel rod deflection in the top and bottom spans matched reasonably well with deflections estimated from the high-speed video. Because the north and south windows were the only openings in the basket, only comparisons with these two spans can be made. In the model, the peak deflections of the top and bottom spans were 7.5 and 9.1 mm, respectively. In the test, the peak deflections were estimated to be around 6 mm in the top span, and between 10 and 12 mm in the bottom span. Low contrast between the fuel rods in the foreground and background made it difficult to precisely estimate the peak deflection.

Residual deformation of the spacer grids was also a good match with the test data, as illustrated in Table 4.2. Here, Grids 1 and 12 correspond to the grids at the top and bottom of the assembly, respectively. The test data are shown as the average of the two measurements taken from each side of the grid. The model data represent the average crushing across the width of the grid. In terms of the maximum grid crushing observed over the entire fuel assembly, the model and test agree well—5.5 mm in the model compared to 5.8 mm in the test. The maximum was observed in different grid spacer locations, Grid 10 in the model versus Grid 9 in the test, but both of these are adjacent to the longest spans in the

assembly and thus support the greatest load, so the maximum occurring in either of these would be a reasonable outcome. One shortcoming of the model is that it tends to underpredict the amount of crushing when the impact force is relatively low, for instance in the cases where the crushing in the test measured about 2 mm or smaller.

Table 4.2. Comparison of Grid Crushing Observed in SNL Assembly Drop Test and in the Model

	Grid Crush (mm)	
	Test	**Model**
Grid 1	0.6	0.0
Grid 2	1.5	0.0
Grid 3	1.6	0.1
Grid 4	0.9	0.2
Grid 5	1.2	1.1
Grid 6	1.0	0.6
Grid 7	2.0	0.9
Grid 8	2.3	1.4
Grid 9	3.6	5.5
Grid 10	5.8	5.0
Grid 11	1.3	0.0
Grid 12	0.6	0.0

The final shapes of the two most deformed spacer grids (9 and 10) in the model and test are compared in Figure 4-17. Buckling in the test occurred over approximately the lower third of the grid, and the outer grid straps took on a shear-racking pattern. The grids in the model deformed in a similar shape, with all of the buckling behavior taking place in the lower third of the grid.
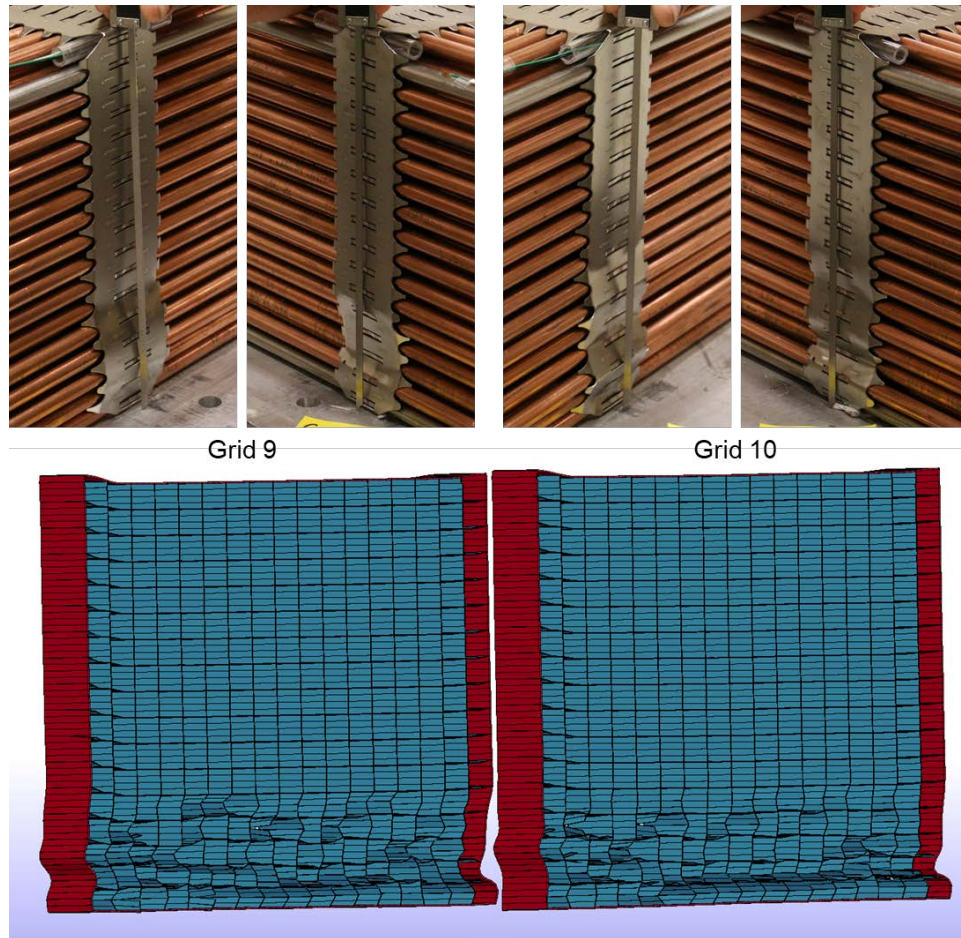
Figure 4-17. Comparison of Buckled Shape of Grids in Model and Test

Rod-to-rod and rod-to-basket impacts were observed in both the model and the test. The upper bound on the impact force is difficult to discern from the test data, because the pressure paper provides only an indication that a certain range of contact pressure has been exceeded. The fuel assembly model was defined to output the total contact force exerted on each of the fuel rods with respect to time. The model contact data were used to estimate the peak rod-to-rod and rod-to-basket contact force in the SNL assembly drop, which were 831 and 440 N, respectively. The corresponding peak contact pressure was 1035 and 511 MPa. This far exceeds the 8000 psi (55 MPa) trigger point of the contact pressure in the test. These values are approximate and likely conservative, because the contact force measurement in the model does not separately resolve contributions from multiple points of contact at a given instant. Nevertheless, the contact pressure is below the threshold needed to induce local yielding, which occurs when the contact pressure is at least 1.6 times the yield strength (Barber 2018), which is 1250 MPa at 200°C and 10 GWd (Geelhood et al. 2008). This discussion is a summary of the larger contact force analysis done in Appendix C, which describes the analytical solution and the FEA justification for the values reported here.

4.2.3   Discussion

The crushable grid fuel assembly model corroborates the results of the SNL assembly drop test, albeit with some caveats. The model predicted a strain of 1806.9 uE at the highest strain gage location in the test, which measured 1428.4 uE in the test. The model predicted a peak strain of 2652.9 uE near the spacer grid adjacent to the peak strain gage. This indicates that the actual maximum strain in the fuel bundle in the test was greater than the reported strain gage value. Despite this, there is still a significant

margin with respect to the yield strain of the cladding, which is about 9800 uE for low burnup (10 GWd) fuel at 200°C (Geelhood et al. 2008).

Overpredicting strain means that the model is conservative. The model overpredicted the peak strain at all of the strain gage locations, by an average of 500 uE. Though this level of overprediction is comparable to the strain gage values themselves (e.g., SG13-SG18, Figure 4-18), this error only constitutes about 5% of the cladding yield strain, and the peak strain in the model consumed only about 27% of the available margin to yield. If the test and model results suggested that cladding was very close to yielding during a drop event, this level of disagreement would be more concerning.

Slight differences between the behavior of the fuel assembly in the model and the test can be seen in the high-speed video footage of the south window, near where the peak strain occurred. While both the model and test indicated about 10 mm of fuel rod deflection in this span, the deformed shape of the instrumented fuel rod is quite different (Figure 4-18). The deformed shape in the model was similar to a fixed-fixed beam, where the slope is near zero at the supports (grids). In the high-speed video, the shape was more akin to a simply supported beam; the grid appeared to buckle in a way that allowed more rotation at the end of the span. For a given displacement, a beam with less rotational stiffness at the supports will have a lower strain, confirmed by a simple calculation from beam theory. These differences do not necessarily reflect a flawed model, because buckling is a partly stochastic behavior influenced by imperfections in the complex grid structure and gross deformation of the basket due to previous impacts (evident in the bottom-center of high-speed video frame in Figure 4-18).
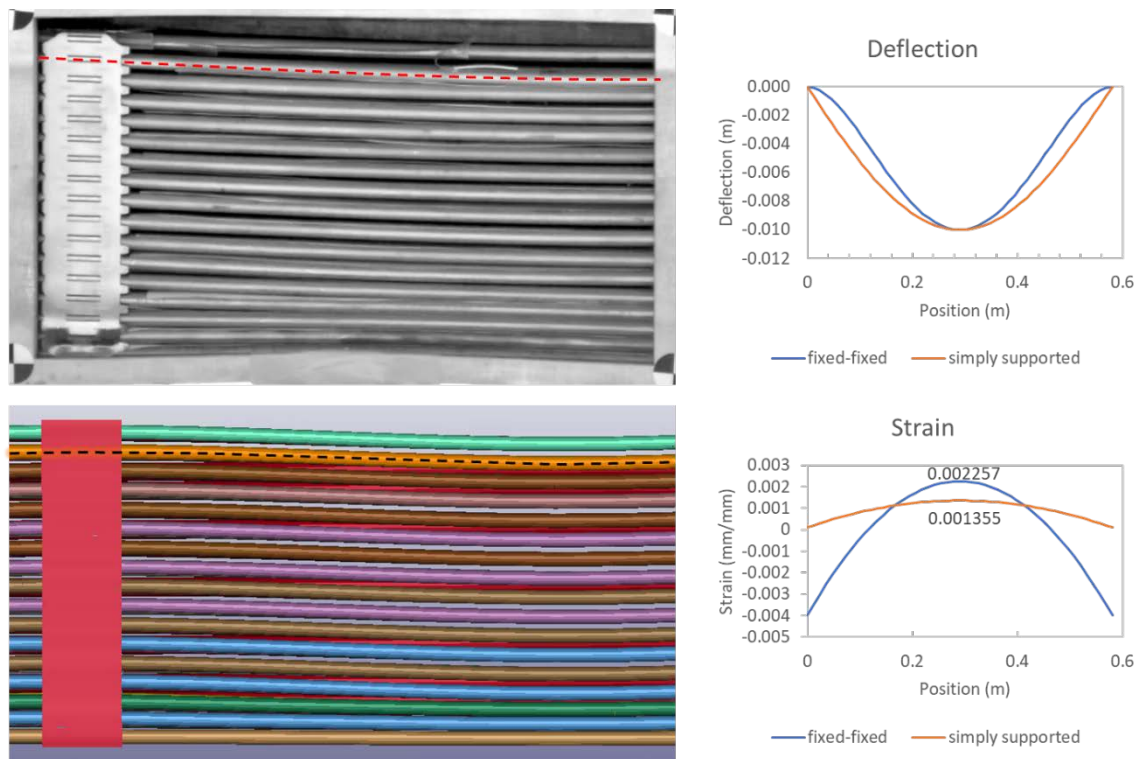
Figure 4-18. Deformed Shape of Fuel Rods in the Model (bottom left) and the Test (top left), and Comparison of Boundary Conditions in Beam Theory (right)

Another possible reason for the overprediction of strain is that the fuel rods in the model showed a more pronounced high-frequency response, above 150 Hz. Reducing the low-pass cutoff frequency applied in Figure 4-15 to 100 Hz effectively eliminates this high-frequency response and shows much better agreement for strain gages in the short spans. It is postulated that the grids in the model are too stiff

in the low deformation regime and transmit more of the high-frequency content of the impact. This may also explain the underprediction of small residual deformations (<2 mm) evident in Table 4.2.

Other measured aspects of the test, such as fuel assembly acceleration, grid crushing, and fuel rod deflections, showed good agreement with the model. The model is not perfect, but it provides a reasonable and conservative estimate of cladding strain. This provides confidence that the model can be used for generic analyses of 30 cm drop events, as is done in Section 5.1.

While this model represents a step forward in modeling SNF during drop events, several things could be done to improve it. First, the amount of damping and energy dissipation in grids during impact should be more closely studied and implemented in the model. Comparisons to test data suggest that the amount of damping is too low when grid deformation is small, transmitting too much high-frequency content from the impact into the fuel. Secondly, the discrete springs used to represent the springs and dimples in the model tend to exhibit instability when the grid becomes extremely deformed, which can lead to a non-physical response. Though this has a minimal effect on the current analysis, this behavior should be corrected before modeling higher-energy impacts, such as a 9 m drop. Verifying that the model works well for such HAC drops is another future objective, because both the model response and actual grid behavior are relatively unexplored for drops larger than 30 cm. Finally, further development of the contact stress analysis initiated in this work is warranted. This work presents likely conservative estimates of contact stress, but the results could be further refined by modifying the model to report contact forces at greater spatial resolutions. This work also uses the onset of local yielding as a failure criterion, but a more realistic value would be the contact pressure needed to cause gross yielding through the cladding thickness, which could be calculated using a plastic FEA of the cladding.

4.2.4   Conclusions

A fuel assembly model with crushable spacer grids was developed, which allows the modeling of the permanent deformation induced by loads lateral to the fuel during a drop event. This model was used to simulate the SNL 30 cm assembly drop, and a reasonable level of agreement with the test data was achieved in terms of fuel cladding strains, grid permanent deformation, and fuel rod accelerations. The level of agreement achieved between the model and test data provides confidence that the crushable grid fuel assembly model can be used to model the fuel structural response in generic 30 cm package drop conditions, as is done in Section 5.1.

The model predicted conservative estimates of cladding strains compared to strain gage data from the test. Nevertheless, the results still indicate that fuel in the as-tested condition at SNL retains its structural integrity. The peak strain predicted in the model was 2652.9 uE, which is far below the yield strain of the cladding. Initial estimates of cladding contact stresses (e.g., rod-to-rod and rod-to-basket impact) were developed that suggest that the contact forces in a 30 cm drop are below those needed to initiate yielding.

Additional development work on this model is needed to further refine its predictions beyond the conservative estimates given in this work. Further studies are needed to establish the appropriate amount of damping and energy dissipation in the model's crushable spacer grids, and to improve the numerical stability of the model. A comparison of the overall system damping in the model to damping observed in the SNL 30 cm assembly drop would contribute to a better understanding of the role of energy dissipation during drop events. Further spatial refinement of the cladding contact stress model is needed to capture individual rod-to-rod or rod-to-basket contact events without having to make conservative assumptions about the distribution of contact forces.

4.3   Conclusions of Test Data and FA Model Validation

This section looked specifically at the as-tested 30 cm fuel assembly drop scenario. The data and the models are all consistent with the test that was conducted at SNL in 2020, which used a non-irradiated fuel assembly and surrogate fuel mass. The question of how a real, irradiated fuel assembly with low

burnup or high burnup properties would respond to the 30 cm drop remains to be determined. The test conditions were as real as practical, and the test is expected to be a close analogue to the behavior of low burnup SNF, but there is a logical step remaining to translate what was learned from the test data to a realistic SNF scenario. This step of estimating what real SNF would experience during a 30 cm cask drop is considered to be part of the "general" 30 cm drop scenario that is discussed in Section 5.

One key phenomenon observed in the 30 cm fuel assembly drop is the permanent deformation of the spacer grids. Several grids permanently compressed, which implies that grid deformation is dissipating fuel assembly impact energy as plastic strain energy. Damping and energy dissipation of the system is one key area where the model can be enhanced. The indications are that the current model does not remove enough energy from the system in its current state. While that is a conservative feature of the model, it would be better to reduce the conservatism to match reality. Damping is a real, physical phenomenon, and the current body of test data can guide the selection of damping parameters. This has not been done yet for 30 cm drop or NCT shock and vibration because it is easier to assume minimal damping than to determine accurate damping. But it is recommended to determine realistic damping parameters to help close the stress profiles knowledge gap because damping matters in the 30 cm drop scenario.

The new crushable grid fuel assembly finite element model agreed reasonably well with the test data. The model predicted a peak strain gage value of 1806.9 uE, compared to 1428.4 uE in the test, which is reasonably good agreement in this kind of model. The amount of grid crushing was also predicted well by the model (about 5-6 mm of permanent deformation). The models and test data both agree that there is significant cladding strain margin, so failure from a single 30 cm horizontal cask drop is not expected. As noted above, the as-tested scenario is similar to a low burnup SNF assembly 30 cm drop in a horizontal impact orientation. The general SNF cask drop scenario is discussed in the next section.

5   GENERAL 30 CM DROP ANALYSES

The 30 cm cask drop is often performed in the horizontal orientation. In Europe, the NCT 30 cm drop is always horizontal, and by regulation they do not need to consider other impact orientations. In the United States, 10 CFR 71.71 requires a drop test, but does not directly specify an impact orientation:

> (7) Free drop. Between 1.5 and 2.5 hours after the conclusion of the water spray test, a free drop through the distance specified below onto a flat, essentially unyielding, horizontal surface, striking the surface in a position for which maximum damage is expected. (The drop height is specified in a table to be 30 cm for packages of 33,100 lbs or greater, which is effectively all SNF casks. The NAC LWT is 80,000 lbs.)

Because DOE partnered with European organizations (ENSA, BAM), the impact orientation for testing was chosen to be horizontal to match European regulatory requirements, and the evaluation of non-horizontal drop conditions was to be completed by PNNL using structural dynamic finite element models that were validated with test data. This section reports the progress made on the evaluation of the general 30 cm cask drop scenario. These analyses still use the ENSA ENUN-32P cask and the SNL Westinghouse 17x17 fuel assembly as the basis for the analyses. PNNL recommends expanding the general analysis case in future work to include all casks in the U.S. fleet and fuel assembly types (similar to the way Klymyshyn et al. [2019] evaluated the general case of SNF NCT shock and vibration).

One example of a 30 cm cask drop analysis is documented in a report by the Electric Power Research Institute, Inc. (EPRI; Rashid et al. 2007). In that analytical study, the horizontal drop orientation was selected based on the observation that a previous analytical study (SAND90-2406, by Sanders et al. 1992) predicted the highest loads for all anticipated fuel rod failure modes is developed in the horizontal drop orientation. In addition, the cask drop analysis by Rashid et al. 2007 modeled the impact of a partial cask section onto a theoretically rigid surface, without including the contribution of impact limiters. The EPRI study and the current PNNL study make substantially different assumptions, and arrive at different conclusions. PNNL recommends follow-up work to describe the differences in modeling approaches and conclusions between the current work and the EPRI study; it is too much to attempt to complete in this work scope.

Section 5.1 describes the modeling architecture used in this study to explore the general case of a 30 cm cask drop. It describes model validation relative to existing test data and calculates an initial estimate of cladding strains and grid crush over the range of all possible 30 cm drop scenarios. Importantly, this study only considers the as-tested material state, which is similar to low-burnup SNF. The high burnup SNF condition has not yet been analyzed but needs to be in follow-up work to close the knowledge gap. In NCT shock and vibration the low-burnup (low stiffness) fuel rod case was most limiting, but it is possible that the difference in loading environment could make the high burnup case more limiting in the 30 cm drop. The peak cladding strain from this study is 4637 uE in the 60° drop, which is greater than the 1430 uE recorded in the test.

Section 5.2 discusses some initial progress on a modeling task to relate PNNL structural dynamic modeling to phenomena observed in the PNNL Sibling Pin test program (see Saltzstein et al. 2020 for details of the Sibling Pin test campaign). Gas communication test results inspired inquiry into the phenomenon of fragmented fuel pellets and what that might mean for local cladding stresses. The study is not complete, but the process of translating bending loads from the PNNL fuel assembly model to a fuel rod segment submodel raised an important point about the difference between transient loads and static loads.

Section 5.3 discusses the potential to simplify the analysis from a full fuel assembly to something smaller in scope that might be equally effective. PNNL has not attempted to reduce the model complexity yet, but it would be very useful in defining the range of loads in the general 30 cm drop scenario. The section outlines some thoughts about how to approach the problem.

Section 5.4 summarizes the conclusions and describes the work that remains to be done to close this stress profiles knowledge gap.

5.1   Modeling Architecture and Execution

5.1.1   Background

The cask impact model described in Section 2 and the crushable grid fuel assembly model described in Section 4.2 were brought together in a modeling architecture for analysis of generic 30 cm drop scenarios (Figure 5-1). In this architecture, the cask impact model is first run to calculate package motion time histories in a drop event of a given height and cask orientation. These motion time histories are then applied to a rigid basket cell surrounding the crushable grid fuel assembly model. This is the same concept as the simulation of the SNL assembly drop in Section 4.2, except that the prescribed motions applied here are based on the cask impact model, instead of being derived from high-speed video footage from an experiment. Modeling the cask and fuel separately was a consideration for computational efficiency, because the fine detail of the latter requires a much smaller time step in the explicit dynamics calculation. For comparison, on an ordinary desktop computer, the cask impact model takes about 2 hours to run 1 second of simulation time, compared to about 50 hours for the crushable grid fuel assembly model.
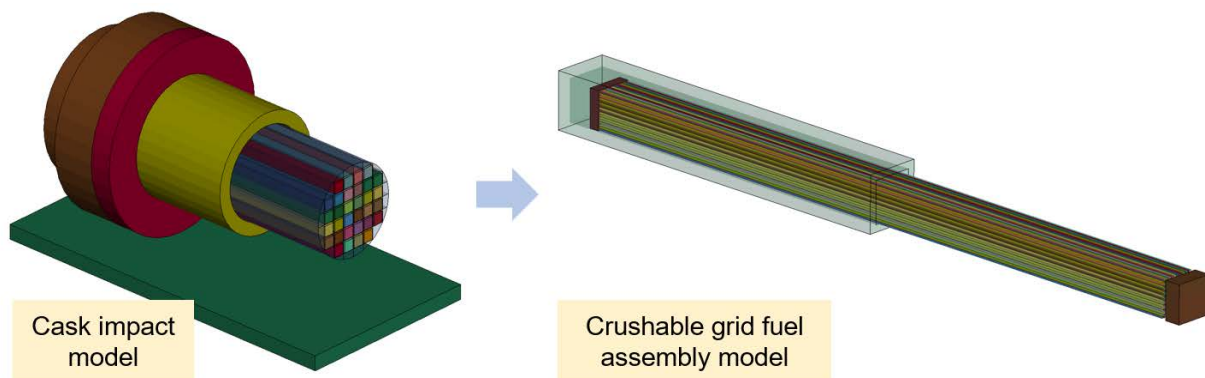
Figure 5-1.   Overview of the Modeling Architecture for Generic 30 cm Drop Analyses. The package (left) and rigid basket (right) are sectioned in this illustration to show the internal components of each model. The fuel assembly model is shown with grids hidden.

Table 5.1 summarizes the results of the various SNF 30 cm drop analyses conducted in this work. This includes all of the modeling scenarios where the shock and vibration environment of a drop was prescribed for the fuel assembly model. A more complete discussion of the results is presented in Section 5.1.2 and Appendix B. In addition to the SNL assembly drop simulation discussed in Section 4.2, the five drop orientations identified as potentially adverse or reference cases in Section 2.2.1 were modeled. Four sensitivity studies were conducted to assess the modeling simplifications and assumptions and the effects of secondary impacts.

Table 5.1.   Summary of SNF 30 cm Drop Analyses Conducted in this Work

Set	Time History	Basket-fuel Gap	Cladding Properties	Peak Cladding Strain (uE)	Peak Grid Crush (mm)
SNL drop	Basket time history from test	4 mm (18% lateral gap)	Room temperature, unirradiated	2653	5.5
Potentially adverse drop conditions and reference cases	0° cask (end drop)	260 mm (99% longitudinal gap)		1133	0.0
	20° cask (CG-over-corner)	22 mm (99% lateral gap)		4651	16.6
	40° cask	22 mm (99% lateral gap)		4515	14.9
	60° cask	22 mm (99% lateral gap)		4673	12.0
	90° cask (side drop)	22 mm (99% lateral gap)		3122	5.7
Windowed analysis check	60° cask, initial impact	0.2 mm (1% lateral gap)	Room temperature, 10 GWd (low burnup)	368	0.0
		22 mm (99% lateral gap)		1562	0.0
Basket-fuel gap sensitivity study	0° cask (end drop)	2.6 mm (1% longitudinal gap)		1103	0.0
		130 mm (50% longitudinal gap)		848	0.0
	90° cask (side drop)	0.2 mm (1% lateral gap)		924	0.0
		11 mm (50% lateral gap)		2771	5.0
Fuel assembly orientation sensitivity study	90° cask (side drop)	0.2 mm (1% lateral gap)		944	0.0
		11 mm (50% lateral gap)		2618	6.7
		22 mm (99% lateral gap)		2603	9.2
Effects of cladding temperature	90° cask (side drop)	22 mm (99% lateral gap)	200°C, 10 GWd (low burnup)	3319	6.0

The first study validates the approach of separating longer drop events into multiple analysis "windows." In drop orientations between 0° and 90°, the cask impacts first on a corner and then tips onto either the side or end face (slapdown) as the package reaches an equilibrium position. In orientations such as the 20° CG-over-corner case, there is substantial time between these impacts where little is happening to the SNF (Figure 5-2). The initial impacts are relatively benign, with package accelerations below 5 g, and it was assumed that this would result in no permanent deformation of the SNF that could affect its response in subsequent impacts. Thus, for the 20°, 40°, and 60° drop orientations, a windowed approach was taken where only the second, more substantial, slapdown impact was simulated in the fuel assembly model. This assumption was checked by simulating the initial impact in the 60° case, which exhibited the largest lateral package acceleration (3 g, in the orientation most likely to cause grid crushing).
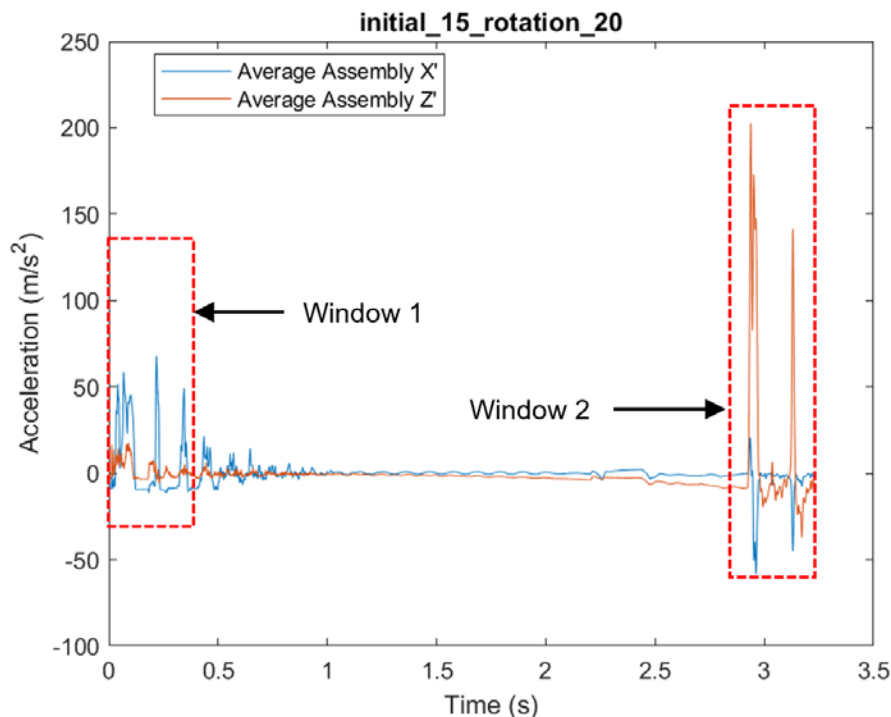
Figure 5-2. Average Surrogate Assembly Acceleration in the 20° CG-Over-Corner Drop, Showing the Shock Pulses from the Initial Impact (Window 1) and from Slapdown (Window 2)

The second sensitivity study investigates the effect of the basket-to-fuel assembly gap, which is a counterpart to the sensitivity study on the cask-to-basket gap in Section 2.2.2. The gap between the basket and the fuel assembly controls the degree to which secondary impact loads the SNF. When no gap is present at the time of impact, the shock on the package will be transmitted to the SNF. When a gap is present, a secondary impact between the fuel assembly and basket will occur when the gap closes. The SNF response was simulated in both side and end drops where the lateral or longitudinal gaps (respectively) were fully closed, half open, and fully open.

The third sensitivity study investigates the effect of the orientation of the SNF during the drop. The side drop was modeled with the basket and fuel rotated 45° about its longitudinal axis. The same configuration was tested at BAM in 2018. Both test data (Section 4.1) and simulations (Section 2.1.3) found practically no difference between the rotated and non-rotated configurations in the package or surrogate assembly accelerations. However, because that model and test used surrogate assemblies, the effect on fuel integrity could not be assessed.

The fourth and final sensitivity study investigates the effect of elevated temperature material properties on the SNF response. Room temperature material properties of Zircaloy-4 were used throughout this work, because they represented the as-tested configuration in the SNL assembly drop. In this study, a side drop was simulated using properties calculated at 200°C, which is thought to be reasonably representative of in-field conditions where SNF is warmed by decay heat. On the other hand, the effect of irradiated material properties on SNF response was not thoroughly studied. A representative low burnup of 10 GWd was used throughout this work (except for the SNL drop, which was done on unirradiated material), which is a conservative assumption. Higher burnup leads to irradiation hardening and increased cladding yield strength.

5.1.2   Results

The results of the generic drop analyses and sensitivity studies are summarized here. For additional details such as contour plots and time histories of the maximum strain, see Appendix B.

5.1.2.1   *Potentially Adverse and Reference Drop Conditions*

The results of the three potentially adverse (20°, 40°, and 60°) impacts and two reference (0° and 90°) impacts are summarized in Table 5.2. All of the cases were simulated with the maximum possible gap between the basket and the fuel. This corresponds to a 22 mm lateral gap in the 20°, 40°, 60°, and 90° configurations, where the peak acceleration occurs lateral to the fuel, and a 260 mm longitudinal gap in the 0° configuration, where the peak acceleration occurs axial to the fuel. This configuration was chosen because the sensitivity study in Section 5.1.2.3 indicated that a larger gap tended to yield higher strains, and thus a more conservative analysis. The fuel assemblies were also oriented within the cask such that the longest spans would be subject to the greatest local acceleration (at the package end with highest velocity during slapdown).

**Table 5.2.   Summary of Results in the Five Potentially Adverse and Reference Drop Conditions Simulated**

Case	Peak Cladding Strain (uE)	Maximum Grid Crush (mm)
0° (end drop)	1133	0.0
20° (CG-over-corner)	4651	16.6
40°	4515	14.9
60°	4673	12.0
90° (side drop)	3122	5.7

The maximum cladding strain (4673 uE) was observed in the 60° drop orientation. This corresponds to the drop orientation with the peak lateral surrogate assembly acceleration in the cask impact model (Figure 2-5). The maximum grid permanent deformation (16.6 mm) was observed in the 20° drop orientation. This corresponds to the drop orientation with the peak package end acceleration in the cask impact model (Figure 2-5). Figure 5-3 shows a contour plot of cladding strains at the instant of maximum strain in the 60° drop. The peak strain and grid crush always occurred within the longest span adjacent to the bottom nozzle.
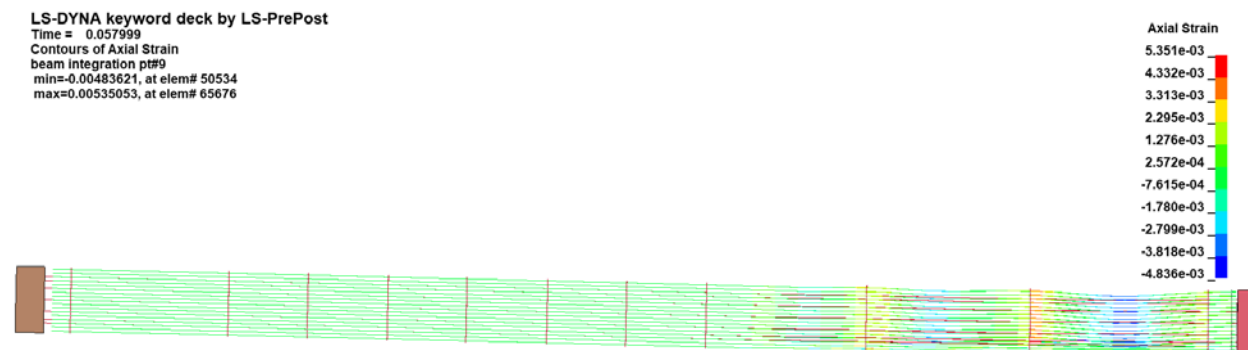
Figure 5-3.   Contour Plot at the Moment of Maximum Strain in the 60° Drop. The strain shown in this figure is unfiltered.

Figure 5-4 compares the final shape of the most deformed grids in the SNL assembly drop simulation, the 30 cm side drop, and the 30 cm CG-over-corner drop. The amount of grid crushing in the SNL test and simulation and the generic 30 cm drop were very similar, all in the range of 5–6 mm. The CG-over-corner drop showed much more extreme grid crushing up to 16.6 mm, with buckling occurring throughout the bottom 60% of the grid.
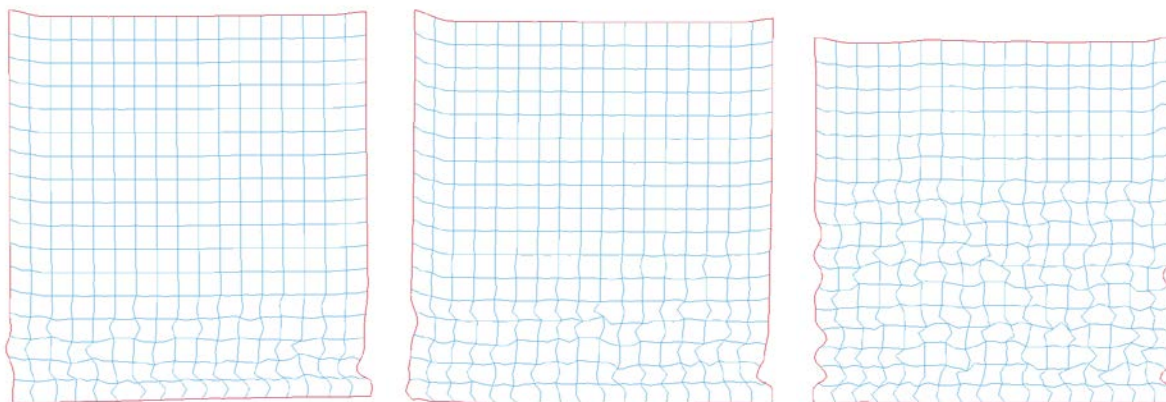
Figure 5-4. Final Shape of Most Deformed Grids in the SNL Assembly Drop Simulation (left), Generic 30 cm 90° Side Drop (center), and Generic 30 cm 20° CG-Over-Corner Drop (right)

Rod-to-rod and rod-to-basket impacts were observed in all of the drop scenarios except for the 0° end drop. The contact forces and stresses were analyzed in the 60° drop orientation, which is thought to be the limiting scenario because it featured the highest cladding strain and thus the largest cladding deflection. Contact stress analysis of the other cases are left as potential future work, because it is a time-consuming manual process to extract the contact force and fuel rod curvatures needed to calculate the peak contact stress. The peak rod-to-rod and rod-to-basket contact forces were 1010 and 1590 N, respectively. The corresponding contact pressures were 1107 and 784 MPa. These values are higher than those calculated for the SNL assembly drop in Section 4.2, but are still below the value needed for onset of local yielding in the cladding (at least 1.6 times the yield strength, or 1250 MPa at 200°C and 10 GWd [Geelhood et al. 2008]). This discussion is a summary of the larger contact force analysis done in Appendix C, which describes the analytical solution and FEA justification for the values reported here.

5.1.2.2   *Windowed Analysis Check*

The initial impact in the 60° drop orientation was studied and checked for any permanent deformation in the model that could invalidate the windowed approach used to simplify the analyses of the 20°, 40°, and 60° drop simulations. The initial impact in these cases, corresponding to a corner of an impact limiter contacting the ground, tended to feature much lower package accelerations than the second impact when the side of the impact limiters contact the ground. The 60° case was checked because it had the highest lateral package acceleration (albeit benign at 3 g) in the initial impact. The simulation was configured with no fuel-to-basket gap and with a full fuel-to-basket gap in order to load the SNF with the cask acceleration pulse and by a secondary impact, respectively. The results are summarized in Table 5.3. No buckling or crushing of the grids was observed, and the peak cladding strain was far below the yield point, in both cases. No permanent deformation of the fuel assembly was observed that might affect its response in a subsequent impact event, thus validating the windowed analysis approach.

Table 5.3.   Summary of Results in the Windowed Analysis Check Simulations – Prior to Maximum Impact Load

| Case	Peak Cladding Strain (uE)	Maximum Grid Crush (mm)
60°, initial impact (no gap)	368	0.0
60°, initial impact (full gap)	1562	0.0

5.1.2.3   *Basket-to-Fuel Gap Sensitivity Study*

The end drop (0°) and side drop (90°) drop configurations were modeled using fuel-to-basket gaps that were fully closed, half open, and fully open. The results are summarized in Table 5.4. The cladding strain in the end drop showed virtually no sensitivity to the fuel-to-basket gap. This is because the gap between the ends of the fuel rods and the nozzles ensures that a secondary impact occurs in this configuration regardless of fuel-to-basket gap. In contrast, the cladding strain in the side drop showed a strong sensitivity, exhibiting a 3.4-fold increase from the no gap case to the full gap case.

Table 5.4.   Summary of Results in the Basket-to-Fuel Gap Sensitivity Study

Case	Peak Cladding Strain (uE)	Maximum Grid Crush (mm)
0° (end drop), no gap	1103	0.0
0° (end drop), half gap	848	0.0
0° (end drop), full gap	1133	0.0
90° (side drop), no gap	924	0.0
90° (side drop), half gap	2771	5.0
90° (side drop), full gap	3122	5.7

Figure 5-5 shows the difference in the strain time history at the position of maximum strain in the no gap case and full gap case. The strain "pulse" is significantly taller and narrower in the full gap case, pointing toward a stronger impulse exerted on the fuel in a secondary impact.
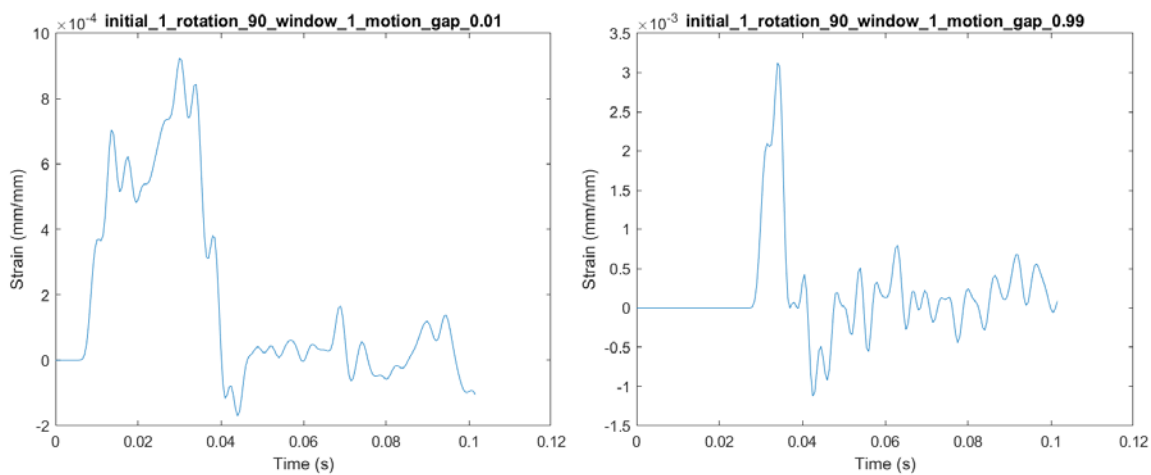
Figure 5-5.   Strain Time History in Element of Highest Peak Strain, for the 90° No Gap Case (left) and 90° Full Gap Case (right)

5.1.2.4   Fuel Assembly Orientation Sensitivity Study

The side drop (90°) configuration was modeled with the fuel assembly and basket rotated 45° about its longitudinal axis. A range of lateral basket-to-fuel gap conditions was evaluated. The results are summarized in Table 5.5. The peak cladding strains of the rotated and unrotated fuel assembly simulations were similar, particularly for the no gap and half gap cases. The behavior diverged somewhat in the full gap case, where the rotated fuel assembly exhibited a lower strain but higher grid crush than the non-rotated assembly. The greater grid crushing in this case may have "cushioned" the SNF in the secondary impact. In terms of cladding strain, the unrotated configuration appears to be more limiting. This validates the choice to use the as-tested orientation throughout the majority of this work, and also strengthens the observations from the BAM test and modeling that the orientation of the basket was inconsequential.

Table 5.5.   Summary of Results in the Fuel Assembly Orientation Sensitivity Study

Case	Peak Cladding Strain (uE)	Maximum Grid Crush (mm)
90° (side drop), no gap, rotated	944	0.0
90° (side drop), half gap, rotated	2618	6.7
90° (side drop), full gap, rotated	2603	9.2
90° (side drop), no gap, unrotated	924	0.0
90° (side drop), half gap, unrotated	2771	5.0
90° (side drop), full gap, unrotated	3122	5.7

5.1.2.5   Elevated Cladding Temperature Sensitivity Study

The side drop (90°) configuration with full gap was simulated using cladding and guide tube properties calculated at 200°C (Table 5.6). The material properties for the fuel rods and guide tubes were calculated using the correlations of Geelhood et al. (2008) assuming a representative low burnup of 10 GWd (Table 5.6). Compared to the room temperature properties, all measures of stiffness and strength are lower. The results of the sensitivity study are summarized in Table 5.7. At elevated temperatures, the peak cladding strain increased by 6.3%, and the grid crush increased by 5.3%.

Table 5.6.   Zircaloy-4 Material Properties Used in the Elevated Cladding Temperature Sensitivity Study

	Fuel Rods		Guide Tubes	
	RT (22°C)	200°C	RT (22°C)	200°C
Young's Modulus (GPa)	89.3	78.7	104	93.1
Tangent Modulus (GPa)	13.4	10.8	14.7	11.8
Yield Strength (MPa)	985	769	778	607
Yield Strain (uE)	11000	9780	7500	6520

Table 5.7.   Summary of Results in the Elevated Cladding Temperature Sensitivity Study

Case	Peak Cladding Strain (uE)	Maximum Grid Crush (mm)
90° (side drop), full gap, 200°C	3319	6.0
90° (side drop), full gap, RT	3122	5.7

5.1.3   Discussion

Numerous generic 30 cm drop simulations were performed by exercising the cask impact model and crushable grid fuel assembly models described in this work. The simulations aimed to identify the range of cladding strains that may occur during a 30 cm package drop, to validate modeling simplifications and assumptions, and to identify model sensitivities.

Five potentially adverse and reference drop orientations were modeled, yielding a range of peak cladding strains. This included an end drop (0°), side drop (90°), CG-over-corner drop (20°), and two slapdown events (40° and 60°). The CG-over-corner and slapdown events were the most adverse, all had similar peak cladding strains ranging between 4515 and 4673 uE. The end drop (1133 uE) and side drops (3122 uE) were considered reference configurations, because they are orientations likely to be encountered during package handling and transportation. All of these strains are far below the yield strain of the cladding (about 11,000 uE at room temperature).

The effects of elevated temperature on the SNF response was quantified in a sensitivity study, which showed a 6.3% increase in the peak strain between models simulated at room temperature and at 200°C. After applying a conservative scale factor of 1.1x to account for reduced fuel rigidity at elevated temperature, the maximum strain observed in this work only consumes 53% of the yield strain at 200°C (9780 uE).

Secondary impact appears to be a significant factor in the load transmitted to SNF during a drop event. When there was no initial gap between the basket and SNF at the moment of impact, cladding strain was minimized, and grid buckling did not occur. Introducing a gap—and thus secondary impact—between the basket and SNF increased the cladding strain by up to 3.4 times and caused the grids to buckle. This demonstrates that secondary impact is an important phenomenon to consider in drop events. This behavior was also observed in the SNL assembly drop test and initial gaps were incorporated in all simulations in this work.

The generic 30 cm drop study predicts cladding strains and grid crushing that exceeds measurements from the SNL assembly drop test. This is due to the difference between the as-tested side impact and more adverse CG-over-corner and slapdown impacts that were simulated. These events have a much higher impact velocity than the 30 cm side drop because one end of the package continues to accelerate after the initial impact. In the 20°, 40°, and 60° impacts, the impact velocity at one end of the package was 7.8, 7.3, and 6.7 m/s, respectively, much higher than the 2.4 m/s of a standard side drop. This translated to cladding strains and grid crushing that exceeded the as-tested configuration (2653 vs 4673 uE and 5.5 versus 16.6 mm). Test data such as those from the SNL assembly drop provide important data points used to benchmark the structural dynamic models of SNF, which can then be used to assess additional and potentially more adverse drop conditions.

It should be noted that several assumptions contribute to the conservatism of this analysis. First, as identified in Section 2.3, the impact limiter properties were chosen to corroborate data from tests conducted at or below room temperature, which likely leads to stiffer behavior and higher package accelerations. Second, the fuel cladding in the model does not account for any contribution of the pellets to its flexural rigidity. Third, the fuel cladding properties were calculated at low burnup; irradiation hardening at higher burnups would lead to an increased margin for cladding yield. Finally, maximum

fuel-to-basket gaps were assumed in the most adverse drop orientations to provide for conservatively bounding estimates of strain.

Potential opportunities for continued development and improvement of the cask impact model and crushable grid fuel assembly model used in this generic 30 cm drop analysis are identified in Sections 2.3 and 4.2.4. One piece missing from the current analysis is a more in-depth analysis of secondary stresses and total stress state in the cladding. This could include a more thorough analysis of rod-to-rod and rod-to-basket contact stress, rod-to-grid pinch loads, and circumferential stress induced by internal gas pressure. The overall FEA architecture could also be applied to HAC drop conditions from up to 9 m, because the cask impact model has already been validated to drop test data from up to this height.

The key conclusions of this study are as follows:

- The as-tested horizontal drop condition is not the most limiting.

- Modeling and analysis is the key to resolving the knowledge gap.

- Additional work is needed to resolve the knowledge gap of what loads SNF assemblies experience during the 30 cm cask drop, including the range of SNF loads for:
  - generic impact orientations
  - the full fleet of cask designs and loadings
  - generalization of loading conditions based on observable 10 CFR 71.71 test data, such as peak 1/3-scale accelerations, and
  - high burnup material properties of fuel cladding and other fuel assembly components.

5.2   Sibling Pin Fuel Phenomena Analysis

PNNL began analyses to evaluate phenomena observed in the Sibling Pin test campaign in fuel integrity structural dynamic models. This work bridges the experimental and modeling work being done in parallel at PNNL. This task was not completed in FY20, but the technical issues that came up from starting this task need to be discussed because they affect many tasks in the SFWST program. This section describes the modeling task that was started (an assessment of fuel fragmentation effect on cladding strain) but will concentrate on the technical observations from the baseline stress calculation and how they relate to the general cask drop scenario.

This study was initiated based on preliminary observations from the Sibling Pin gas communication test at PNNL. It was found that gas pressure of the magnitude expected during vacuum drying could be enough to cause the cladding to expand away from the fuel pellets. PNNL is still evaluating these preliminary experimental results for documentation in a future technical report, but the working assumption is that the expanded cladding would permit a reorganization of fractured fuel pellet material. Figure 5-6 shows a sketch of this hypothetical fuel configuration, with the sketch on the right showing a fragment of fuel that has slipped between an intact pellet and the cladding wall. The concept looks feasible and depending on the size and shape of the fragment it could cause a significant local stress concentration. But before the fuel fragment feature was added to PNNL's fuel rod segment model, an initial stress state was calculated as a baseline for comparison. The baseline stress calculation is the focus of this section.
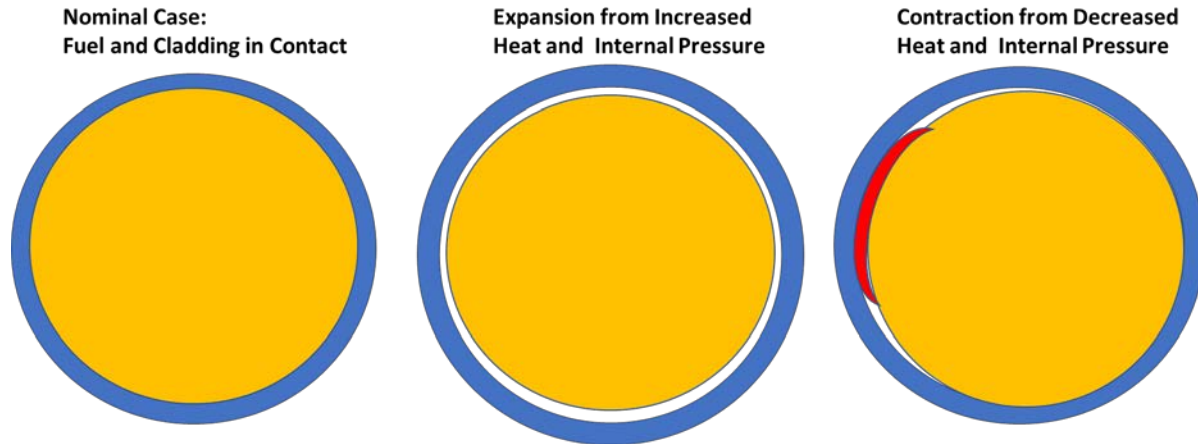
Figure 5-6. Fuel Fragment Study Sketch

The bending moment is an important structural dynamic load on fuel rods. Fuel rods supported at spacer grids are very similar to the classic beam problem where the mass of the fuel rod causes a bending moment under static gravity loads. During dynamic excitation, bending moments can happen due to inertia and vibration. In the NCT shock and vibration loading environment, bending moments were responsible for the axial strains recorded in the MMTT and the maximum axial strains calculated in Klymyshyn et al 2018 and Klymyshyn et al 2019. The NCT shock and vibration loading environment is so benign that rod-to-rod contact is not expected to occur under normal conditions. The 30 cm drop loading conditions are strong enough that rod to rod contact develops impact forces that must be considered and the normal forces at the grid spacers also need to be considered. This discussion is focused on the bending moment load, but analysis of the normal forces also needs to be completed in future work.

The previous section described PNNL's use of a detailed fuel assembly model to calculate the response of SNF to the general 30 cm drop scenario. The peak instantaneous bending moment was calculated to be 14 N-m, and this was selected to be the initial structural loading condition for this fuel fragmentation study. The same fuel rod section model described in Klymyshyn et al. 2019 was used, with the intention of modifying the model geometry to include the fuel fragment shown in Figure 5-6 in a later step. This task was halted after the baseline stress state was calculated due to time constraints.

The 14 N-m bending load was applied as a static load to the fuel rod segment model of Klymyshyn et al. (2019). The model replicates ORNL's CIRFT test by using boundary conditions on a fuel rod segment to apply a uniform state of bending. This version of the model has discrete fuel pellets modeled inside the cladding tube. The pellets have the ability to slide inside the cladding tube and friction effects are included. Note that the SNF rod section model matches the geometry and composition of a specific test sample discussed in Wang et al. 2016 (the HB Robinson fuel sample) so it is not consistent with the as-tested fuel assembly. The inconsistency of geometry was accepted as a simplification in this initial analysis, but the implications of the inconsistency are very important to note when it comes to relating test results and fuel assembly model results to the Sibling Pin data, and this point is discussed in more detail later in this section. The axial strain state that results from the applied bending moment is plotted in Figure 5.7, with a displacement amplification of 10x to show the bending shape. The fuel pellets are not shown, but their effect on the distribution of cladding strains can be observed in the orange contour band, which has a square-wave shape. Figure 5.7 shows that the peak cladding strain from bending is 2.792E-3 m/m (which is 2,792 uE). This amount of quasi-static load causes a maximum deflection in the approximately 55 mm long fuel rod section of about 0.2 mm. An important feature of this calculated response is that the quasi-static bending moment causes strains and a gross deflection of the fuel cladding

section. Real 30 cm drop loads are transient, not static, and their time of duration is at least as important as the magnitude.

The source of the 14 N-m bending moment was a single beam finite element that represents a segment of the fuel rod in a structural dynamic model. The beam model was dynamic, so the instant that the beam element calculated the 14 N-m bending moment, the strains, deflections, and other response parameters were all consistent with beam theory for the homogenized elastic fuel rod representation. But when we translate the dynamic load to the more detailed submodel shown in Figure 5.7, and start to consider nonlinear effects, such as fuel fragments sliding, it is not clear that a static model will be sufficient because of potential path-dependency. For this type of modeling study, time history effects need to be evaluated, particularly because the loading is so short in duration.
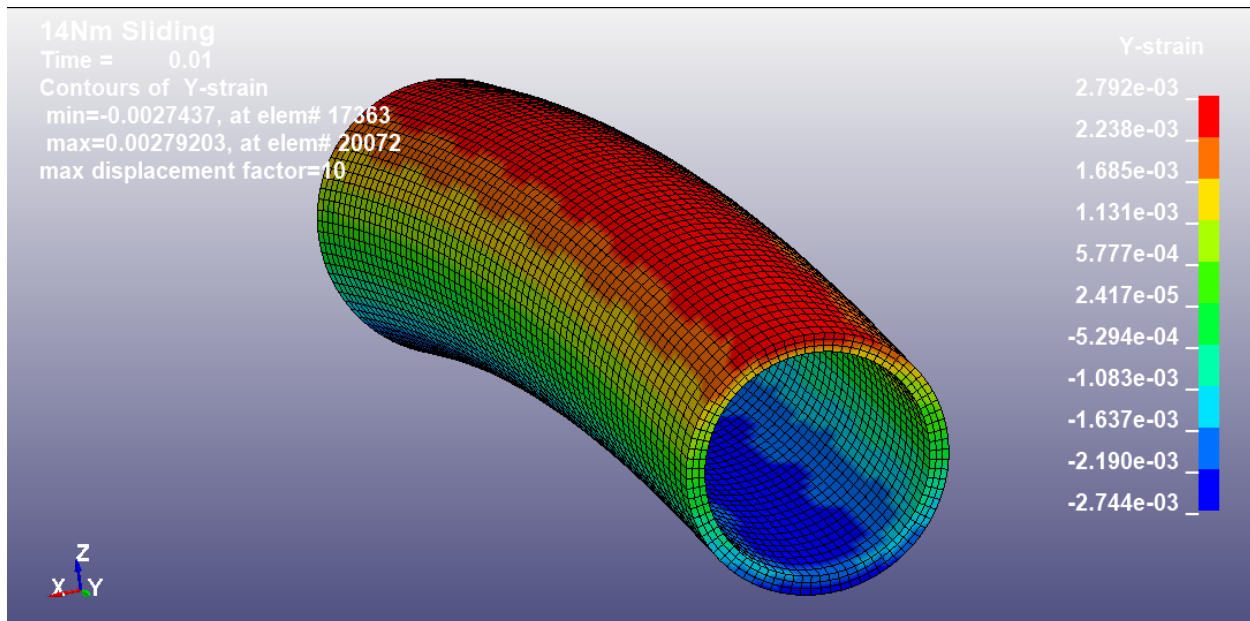
Figure 5-7. 14 N-m Bending Moment Applied to Fuel Rod Segment (Fuel Pellets not Shown). Note that the displacements are exaggerated by a factor of 10 to emphasize the deflection shape.

Figure 5-8 shows the time history associated with the 14 N-m peak bending moment. This is a calculated bending moment in one beam finite element over about 160 ms. The 14 N-m peak is negative in sign and is close to -15 N-m. The negative sign in this case simply indicated the direction of the bending, relative to the elements coordinate system. The plot shows the bending moment pulse is only about 20 ms in total duration and the peak lasts for only a fraction of that time. It is not clear that a detailed fuel rod segment (with realistic geometry and sliding fuel fragments) will behave the same as the homogenized linear-elastic beam element that was used to calculate the dynamic loads. PNNL recommends evaluating this scenario using the transient load history shown in Figure 5-8 in addition to the static loading method shown in this section to determine if static loading is sufficient or if transient loading is required.
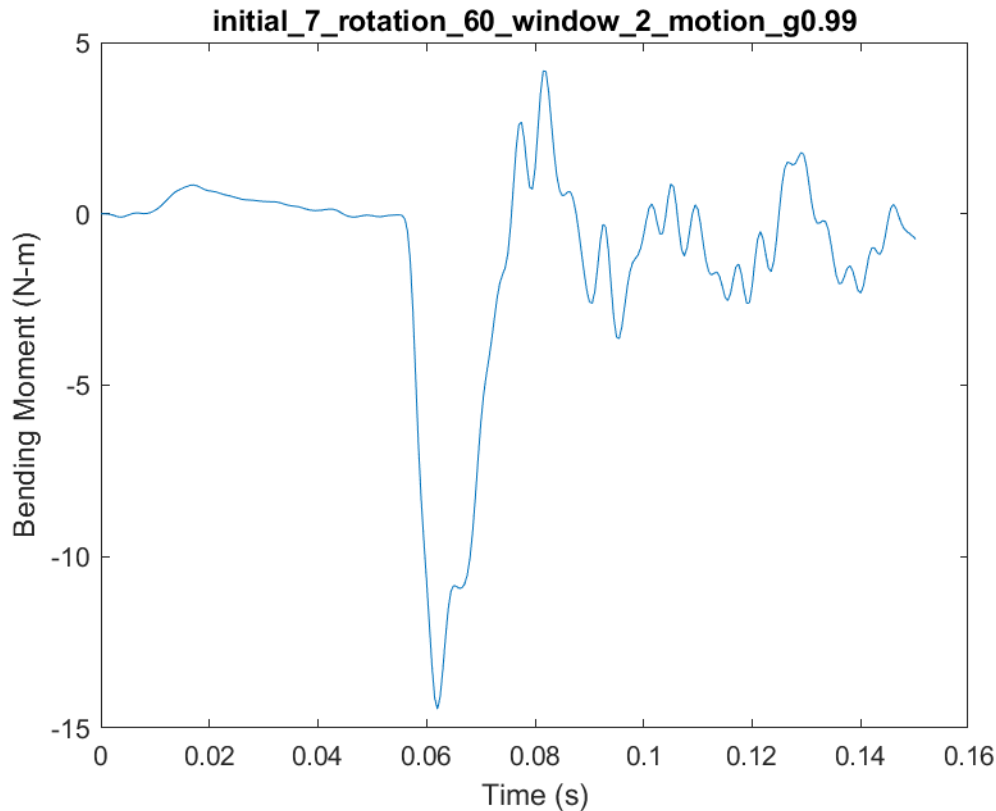
Figure 5-8. Bending Moment vs. Time

The timing of mechanical loads on SNF is a vital technical point that is often neglected for simplicity or conservatism in this kind of modeling and analysis work. But this can lead to physical inconsistencies in analyses. One example of physical inconsistency in modeling appears in Jiang and Wang 2016. The authors selected a 20 g acceleration load for analysis in a fuel rod segment model. The source of the 20 g was the SNL truck test of 2014 (McConnell et al. 2014), but the timing information of the 20 g accelerometer peak was not carried through to the analysis. Instead, the authors used analytical methods to create a hypothetical time history in their model that did not match what was observed in the test. Their assumed acceleration shock pulse would move a body 40 mm in 40 ms, but there is not 40 mm of room inside a fuel basket. There is no way for that hypothetical load to happen within the physical confines of a fuel basket. The physical inconsistency in the time history component of the assumed load was one reason Jiang and Wang's conclusions were not valid, and that lesson needs to be remembered as the program works to close the knowledge gap in SNF stress profiles.

The inconsistency in geometry noted above is significant when translating loads from one fuel rod design to another. The 17x17 PWR fuel design selected for testing by SNL (and modeled extensively by PNNL) was chosen as a conservative design for data collection because the fuel rod diameter, cladding thickness, and bending rigidity (EI) are all relatively low compared to the range of SNF designs in the US inventory. These design features contribute to relatively higher strains, stresses, and fuel rod deflections than other fuel designs in the inventory.

The HB Robinson (HBR) fuel modeled in this section offers a perfect illustration of the problem of applying inconsistent loads to fuel rod segments. The 14 N-m bending moment was calculated in a model that represented the 17x17 PWR SNL test assembly in a 30 cm cask drop scenario. According to beam theory, the HBR and SNL fuel rods should not behave the same to a 14 N-m bending moment because the

HBR fuel segment is 41% longer than the beam element that calculated the load, and the HBR fuel cross section has nearly 100% greater bending rigidity (EI). From classical beam theory:

- The HBR segment should have a 41% lower peak strain
- The HBR segment should have a 27% lower peak strain energy
- The HBR segment should have a 3% higher peak deflection

While the effect of the inconsistency can be calculated if we assume the 14 N-m bending moment is the correct load, the 14 N-m bending moment is almost certainly the wrong load because the HBR fuel characteristics will affect its response to the 30 cm drop scenario. If the HBR fuel assembly is subjected to a cask drop loading scenario, its higher bending rigidity will most likely result in lower bending strain, lower strain energy, lower deflections, and lower bending moments. In order to generate appropriate loading conditions for the HBR fuel rod segment, the HBR fuel assembly should be modeled in the 30 cm drop scenario using the validated modeling methods described in this report. PNNL will determine if this study needs to include the HBR fuel type or if the modeling should select a different fuel design from the Sibling Pin fuel inventory.

Going forward, PNNL recommends continuing this study in FY2021 to determine how best to relate fuel rod dynamic test data and calculated fuel rod transient loads to a submodel of a cladding segment with fuel pellets inside it. One task is to compare static versus transient analysis methods. Another task is to determine if the HBR fuel geometry is worthwhile to consider in this study, or if a specific fuel sample from the Sibling Pin test program should be selected. The goal is to study the influence of fuel pellets on the local cladding stress state and to align with the Sibling Pin test campaign to help close the stress profiles knowledge gap.

5.3   Feasibility of Using a Single Rod Model in 30 cm Drop Scenarios

The MMTT modeling study (Klymyshyn et al. 2018) concluded that the mechanical shock and vibration loads associated with NCT were small enough that a model of a single fuel rod was sufficient to predict the cladding stress and strain under those loading conditions. The follow-up study (Klymyshyn et al. 2019) applied the model methodology to a realistic NCT rail transportation configuration and found that the MMTT loads remained bounding. The 30 cm drop loading scenario has much higher loads and the current modeling and the test data suggest that rod-to-rod contact is almost assured in this loading scenario. This makes the use of a single rod model inadvisable in the horizontal impact orientation.

There is one specific 30 cm drop scenario for which a single rod model might be sufficient to judge fuel rod performance—the vertical or end drop scenario, where fuel rods are aligned parallel to the cask impact velocity vector. The U.S. Nuclear Regulatory Commission has used a single rod model for this specific loading condition in the past (NRC 2007, NUREG-1864). PNNL recommends using the model methodology described by NUREG-1864, appendix C and comparing it to the full fuel assembly model discussed in this report.

One feature the single rod model of Klymyshyn et al. (2018 or 2019) did not include was a way to model secondary impacts, which are discussed in Section 2.2.2 of this report. This analysis shows that the fuel assembly-to-basket gap has a significant influence on the loads, and the DOE test data discussed in this report have shown that secondary impacts are a natural occurrence in cask drop scenarios. When considering how to simplify 30 cm drop structural dynamic models, the gap condition is a key phenomenon that must be included.

PNNL has not attempted to simplify the fuel assembly impact response analysis yet. In the report by Klymyshyn et al. (2018) it was clear that a full fuel assembly was not necessary. In this work, the full fuel assembly model is the best current option because it can calculate a full 3D response. Note that in Figure 4-17 and Figure 5-4, the grid deformation is 3D. The single column model discussed by Klymyshyn et al. (2018) can model rod-to-rod contact, but it assumes lateral deformations are zero, which is not accurate compared to what was observed during testing. PNNL is moving forward assuming that a full 3D model

is necessary to evaluate fuel assembly structural dynamic behavior in a 30 cm drop scenario, but recommends a follow-up study to compare the full 3D model with a 2D single column model to determine if the 2D model can provide adequate results. Such a model would save considerable computation time, potentially reducing calculation time by a factor of 17 (the ratio of element reduction from the full 3D model).

Another idea PNNL has to reduce the scope of the model is to focus on the most limiting span. The trends in the modeling and test data suggest that the most limiting locations of a fuel assembly can be identified based on their geometry. It may be sufficient to model and study the response of the longest unsupported spans to predict the maximum loads on the fuel. PNNL recommends a follow-up study to determine whether this approach is fully supported by the test data. This could potentially benefit the industry and DOE when it comes to assessing the potential damage to fuel in a 30 cm drop scenario.

5.4   Conclusions About the General 30 cm Drop Loading Environment

Understanding the general 30 cm cask drop loading environment is vital to closing the stress profiles knowledge gap. The cask and fuel assembly physical drop tests provide validation data for structural dynamic finite element models. Application of the models to other 30 cm drop impact orientations indicates that other impact orientations are more limiting in terms of structural dynamic loads on SNF. Of all the cases evaluates so far, the 60° impact orientation is currently the most limiting 30 cm cask drop configuration.

To close the stress profiles knowledge gap, the full range of 30 cm drops needs to be considered because the loads change depending on a number of parameters. Here is a list of parameters that are expected to affect the structural dynamic loads (like forces) or response metrics (like strain):

<div align="center">

Parameters that Affect Impact Loads

</div>

- Impact angle orientation
- Cask rotational orientation
- Fuel-to-basket gaps
- Cask design
- Fuel design
- SNF burnup
- SNF temperature

To close the knowledge gap, we need to understand how these parameters affect the loads, or at least understand the range of variation and the maximum loads. As this work is completed, there is likely to be a single most limiting configuration that maximizes loads, but so many factors would need to align that it would be practically impossible to occur under real world conditions. Rather than focusing on the single most limiting case, something like a 95% confidence interval appears more practical and useful. Both of the test configurations (cask and fuel assembly) showed that it was not practical to achieve a perfect horizontal impact, so PNNL does not recommend focusing this analytical effort entirely on the most limiting condition. Knowledge of the variation of impact forces in the general 30 cm drop scenario is at least as important as determining the most limiting condition.

One high priority analysis that needs to be done is the high burnup configuration of the as-tested systems (ENSA ENUN-32P, WE 17x17 PWR assembly). The current analyses assume the fuel assembly is in the as-tested condition (non-irradiated, room temperature, free sliding fuel pellets) which is similar to low burnup. The high burnup condition is expected to cause a significant change in impact response because the stiffness of the fuel rods is expected to increase significantly.

Another important area to pursue next year is a comparison to other 30 cm drop analyses and models in the open literature. Rashid et al. 2007 models a conservative 30 cm cask drop without impact limiters impacting a theoretically rigid surface. That appears to be a very conservative analysis that does not agree with the conclusions of the DOE 30 cm drop test program. A direct comparison study is recommended.

It is also recommended to explore modeling methods with a lower computational cost than the PNNL full fuel assembly model. In the axial (end drop) case there is an example of a single rod model used by NRC. Rashid et al. 2007 used a single span model in the horizontal drop configuration. PNNL's recommended approach is to continue using the fuel assembly model to advance our understanding of the 30 cm drop, and also to consider options to reduce the computational cost to facilitate broad sensitivity studies of the parameters listed above.

6   GENERAL SNF CASK DROP DAMAGE MODEL

Closing the SNF stress profiles knowledge gap requires an understanding of the range of variation in the general case of a cask 30 cm drop. If we only focus on the maximum loads, the most limiting loads, or the loads with the highest potential for damage, that does not answer the question of what loads are typical in a 30 cm cask drop scenario. The program needs to understand maximum loads, typical loads, average loads, and minimum loads to effectively guide the R&D in this area. PNNL's proposed solution to this need is the development of a damage model, which is a tool for aggregating and simplifying a broad library of test data and modeling results into a useful predictive tool.

Given the differences between transportation casks, variation in fuel types, and the potential for a multitude of impact shock pulses, it is not feasible to explicitly test or model all possible conditions that could be experienced by SNF. PNNL has been working on a generic loading and damage prediction model to help fill this gap. Currently, a prototype damage prediction model has been developed with a focus on the ENSA ENUN 32P cask and 17x17 PWR fuel. This prototype model is currently capable of predicting peak accelerations experienced by the fuel during 30 cm drop conditions at various orientations. This model could easily be expanded to provide more input data for comparison purposes, but in its current limited capacity it serves as a proof-of-concept for a more generic damage model. A more detailed description of the process used to generate the model can be found in Appendix D.

6.1   Model Creation

The prototype model was developed based on drop conditions modeled using FEA in LS-DYNA. Regression analyses were performed to determine the relationships between controlled parameters of the drop and the resulting conditions simulated for the fuel. Functional relationships were developed for each output parameter depending on each of the varied model parameters. For the prototype model, the varied parameters included the axial rotation of the cask and the spacing of the internal gap between the cask and the basket containing the fuel (see Section 5.1).

For the variation of the axial rotation of the package in the drop, a known difference in drop outcomes also had to be accounted for: the cask falling onto its side or the cask falling onto its lid. For the simulated data of the ENSA ENUN 32P cask with 17x17 PWR fuel in which a drop angle of 0 degrees meant an end drop and 90 degrees meant a side drop, angles from 0-15 degrees resulted in the cask coming to rest on its end and angles from 20-90 degrees resulted in the cask coming to rest on its side. The difference in final orientation of the cask has a significant impact on the resulting conditions of the fuel, effectively creating a discontinuity for the functional dependence on axial rotation of the cask. As such, further simulations omitted the state in which the cask ended on its lid because it was the less damaging scenario.

When considering variations in the spacing of the internal gap between the cask and the basket using the current library of model results, it was found that insufficient model simulations had been performed to yield a satisfactory estimate of its impact on the results. While trends were observed qualitatively with the number of simulations completed, finding a functional fit to the two additional parameters of the internal gap would require additional runs.

All of the parameters in the list below can be incorporated into the damage model with a sufficient number of FEA cases calculated. A parametric study of the full fuel assembly model on these parameters is needed to establish the general 30 cm drop response of the ENSA ENUN-32P cask design and the WE 17x17 PWR fuel assembly design. Different cask designs and different fuel assembly designs would take additional effort to determine the appropriate shock pulse and modifying the fuel assembly model to represent other designs. While it is not necessary to model every combination of cask and fuel assembly design, the damage model will be more accurate and comprehensive the more analysis cases it draws from to compute its regressions.

Parameters that Affect Impact Loads

- Impact angle orientation
- Cask rotational orientation
- Fuel-to-basket gaps
- Cask design
- Fuel design
- SNF burnup
- SNF temperature

6.2 Results

The prototype damage model used the time histories of the simulated 30 cm drop scenarios described in Section 5.1. For these simulated drops, the maximum internal gap was used both vertically and longitudinally (based on the standard horizontal cask orientation) and the axial rotation was varied in increments of 5 degrees. As previously discussed, the different regimes of the drop further limited these rotations to between 20° and 85°, where 0° is vertical and 90° is horizontal. The time histories were all filtered with a sixth order Butterworth, 300 Hz cutoff frequency low-pass filter.

Peak accelerations were found using the magnitudes of the cask and basket accelerations based on the filtered values of the component accelerations. From these magnitudes, a simple maximum was taken for each drop orientation. These magnitudes were then used with the regression technique described in Appendix D to yield a functional relationship between the drop orientation and the expected maximum acceleration. The peak accelerations are provided below.

Note that the current capability of the damage model prototype is to define aspects of the loading environment, the cask peak acceleration vs. impact angle and the basket peak acceleration vs. impact angle. The intent is to expand the damage model's capabilities such that it can show the same trends for peak cladding strain, peak fuel rod bending moment, or any other result of the FEA model that is of interest. This kind of tool is needed to explain the broad range of loads and outcomes that can happen during a 30 cm cask drop.

6.3 Cask Fit

Two functional relationships between drop angle and peak acceleration of the cask were developed using the R^2 value to determine goodness of fit. Figure 6-1 shows the two functions compared to the simulated data calculated by the FEA model. The term simulated data is used here to distinguish it from test data, which is also discussed in this report. Of the two functional relationships, the second-order polynomial fit had a slightly better goodness of fit at $R^2 = 0.963$. The sinusoidal fit was similar at $R^2 = 0.958$. The parameterized equations are provided in Equations (6.1) and (6.2) for the polynomial and sinusoidal fits, respectively.
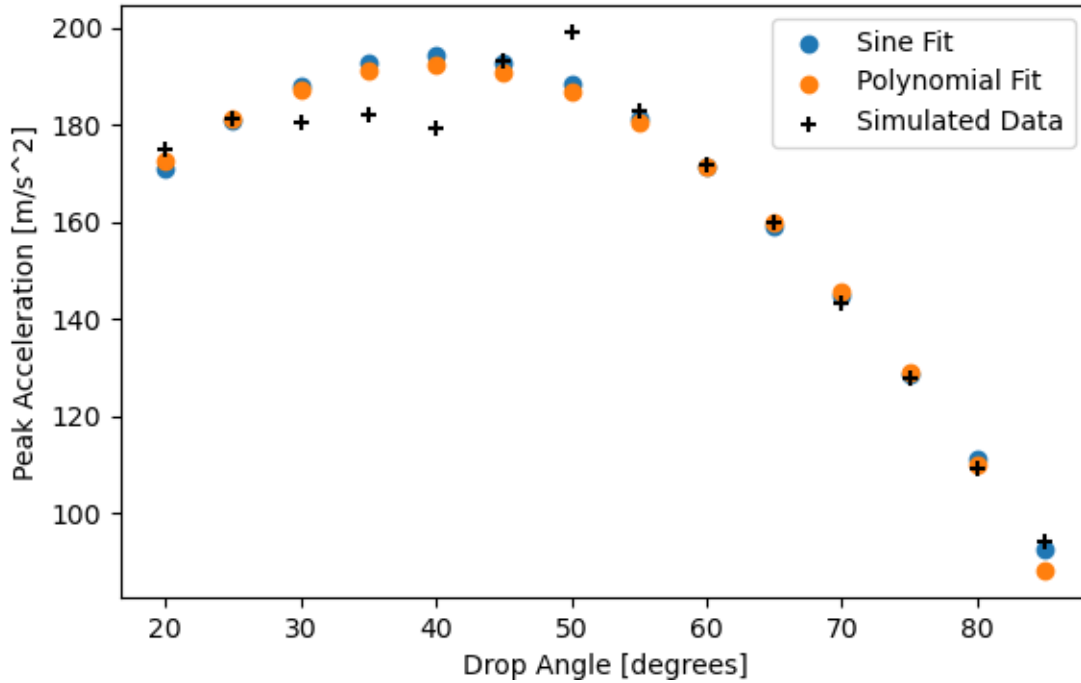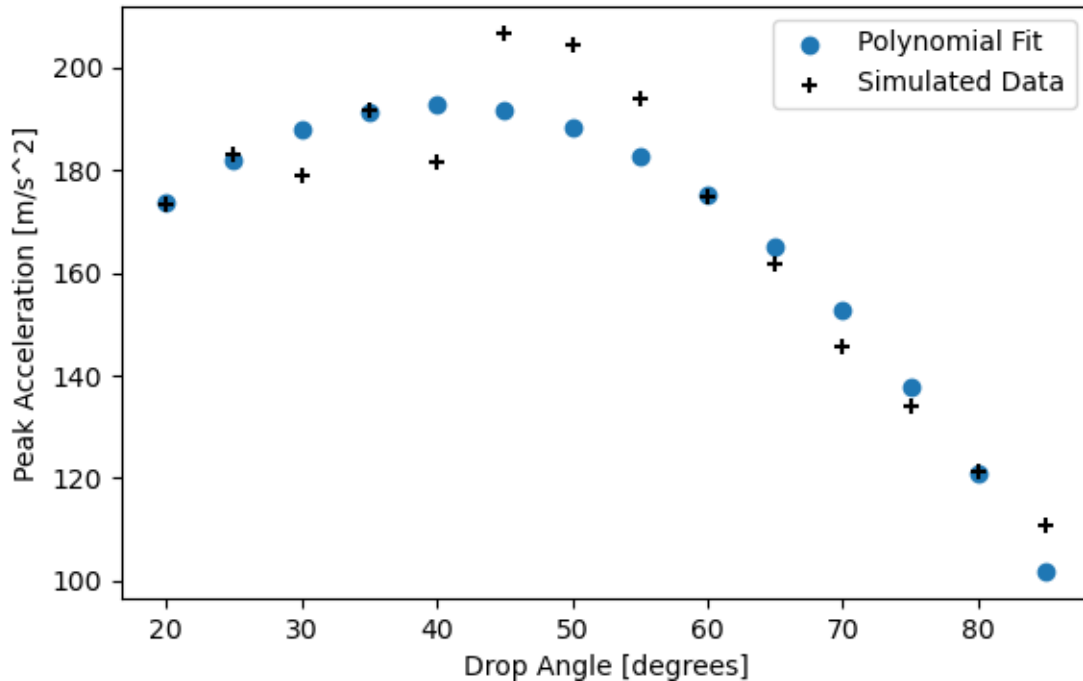
Figure 6-1. Cask Rigid Body Average Peak Acceleration as a Function of Drop Orientation

$$f(x) = -0.0508x^2 + 4.0377x + 111.9300$$

(6.1)

$$f(x) = 87.7607 \sin(-17.5542x) + 107.2529$$

(6.2)

6.4   Basket Fit

Again using R^2 to determine goodness of fit, a second-order polynomial fit was found to be the best approximation for the relationship between drop angle and the peak acceleration in the basket (Figure 6-2). For this functional relationship, the goodness of fit was found to be $R^2 = 0.918$. The parameterized equation is provided in Equation (6.3).

Figure 6-2. Basket Rigid Body Average Peak Acceleration as a Function of Drop Orientation

$$f(x) = -0.0455x^2 + 3.6710x + 118.7151 \qquad\qquad (6.3)$$

6.5 Conclusions and Future Work

While it is possible to create a generic loading and damage prediction model, it is important to note that this model improves depending on the quality and amount of input data used to generate it. As such, future development of this model will require further experimentation and/or simulation of other systems and other drop conditions. This additional work can be concentrated by limiting the simulations to varying the most important parameters and incrementally expanding the source data as more tests and simulations are completed. Other areas for improvement include better quantification of error in the system, especially if any extrapolation will ever be performed.

It is also important for the damage model to present the mean values in addition to the maximum values of the metrics used to evaluate the fuel rod and fuel assembly components.   SNL's WE 17x17 PWR assembly has 264 fuel rods, and from test experience it is known that the peak cladding strain will vary by rod. The FEA model calculates strains at all fuel rod locations, so extracting mean values and statistical information on strains is just an extra step in the post processing procedures. The damage model can easily incorporate that information and provide a valuable perspective on the 30 cm drop loading regime that is needed to close the knowledge gap.

7 CONCLUSIONS

This study performed modeling and analysis of a 30 cm drop of a SNF cask using test data to inform and validate the models. DOE has completed 30 cm drop testing of a 1/3rd-scale cask and a full-scale fuel assembly to observe the structural dynamic loading environment and fuel assembly impact response of the 30 cm cask drop. The data form the basis for constructing explicit dynamic finite element models, which were validated by the test data. PNNL models have demonstrated good agreement with the test data for a specific drop configuration, and the analysts have taken the first step in applying the validated models to solve the problem of a general cask drop of any practical impact configuration (different cask designs, SNF contents, impact orientation, etc.).

The 30 cm horizontal drop test case demonstrates a realistic loading environment for SNF under the regulatory basis NCT cask drop defined in 10 CFR 71.71. The regulations define the cask drop scenario to test the cask design (not the SNF integrity) so it is not a regulatory requirement for SNF to survive the 30 cm drop test. However, evaluating the SNF response to this cask drop loading environment completes DOE's evaluation of the spectrum of loads associated with NCT. The MMTT recorded the SNF loading environment for cask handling and NCT mechanical shock and vibration. The 30 cm cask and SNF assembly drop tests add the data for 1 potential cask drop configuration, but PNNL's analysis indicates that the horizontal drop is not the most limiting 30 cm impact orientation. More analysis is needed to fill the NCT stress profiles knowledge gap to consider the loading environment for the general 30 cm cask drop. These conclusions first discuss the specific horizontal impact case in Section 7.1 and then discuss the general cask drop scenario in Section 7.2. Finally, Section 7.3 recommends an analysis and testing plan to close the NCT stress profiles knowledge gap.

7.1 Horizontal Case

DOE's test data for the horizontal cask drop scenario recorded a global peak cladding strain of 1,723 uE (Kalinina et al. 2020) and a first-impulse peak of 1430 uE (which is the appropriate peak value to validate the model because of the impact timing). These strain values are below the SNF cladding yield strain of 10,000 uE (an estimate for low burnup, room temperature Zircaloy-4 based on Geelhood et al. [2008]). Many spacer grids experienced some measurable permanent deformation as a result of the impact load. The test data indicates a very significant margin against cladding failure and gross structural failure of the assembly.

PNNL developed a new fuel assembly model with crushable grid capability. This model agreed with the test data reasonably well, with some variation. The peak cladding strain calculated at strain gage locations was 1810 uE (compared to 1430 uE) and the peak cladding strain away from strain gage locations was 2650 uE. The PNNL model is conservative (an average of 500 uE higher at each strain gage location), but beam theory can be used to estimate the correct strain with a much tighter error band. Like the test data, the model results indicate a very significant margin against cladding failure and gross structural failure of the assembly. The model has the advantage of calculating the structural dynamic response at all locations of the fuel assembly, and while strains calculated away from strain gage locations were higher, there is no indication that the test's transducers missed any important behavior.

Rod-to-rod contact was observed in the test through the use of contact paper. The paper provides some insight into contact pressure, but finite element modeling is needed to provide an estimate of the local cladding stress and strain. The PNNL model predicts peak rod-to-rod contact pressure of 1035 MPa, and expects that about twice that contact pressure is needed to cause local cladding yielding in low burnup fuel. The test data pressure paper and the calculated rod-to-rod contact pressure from the model both agree that rod-to-rod contact happens in the 30 cm drop but significant margin on cladding failure is maintained.

One thing that PNNL has not done yet is to apply high burnup fuel rod properties to the analysis. The model discussed in this study used the as-tested configuration, which is approximately the same as low

burnup SNF. The primary goal was to validate the model in this year's work, and subsequent work is needed to calculate the response of high burnup fuel.

In addition, the fact that calculated stresses are within an order of magnitude of yield and failure suggests that more investigation is needed to evaluate cladding integrity and include such local effects as pellet-to-clad and pellet-to-pellet interaction. Stress concentrations from the pellets are expected, and other material degradation phenomena such as swelling and fragmentation could locally increase stresses or locally reduce the cladding section's ability to carry load. This additional evaluation is necessary because the test recorded strains on non-irradiated cladding tubes with surrogate fuel mass and the models calculate stress and strain in equivalent homogeneous beams. Both methods neglect potential local phenomena that can affect a real SNF cladding's ability to carry structural loads. The Sibling Pin test program is exploring the material science phenomena that need to be accounted for to relate the test information and calculated model results to failure criteria. This could take the form of stress concentration factors or a reduction in material strength. A phenomenon like the ductile-to-brittle transition (from hydride reorientation) could significantly reduce the effective strength of a fuel rod section.

PNNL has also not yet studied the cumulative fatigue effects of a 30 cm drop. The loading is much higher than the loads experienced during the MMTT, so the potential impact on fatigue life could be very significant. While the NCT shock and vibration environment was found to cause negligible fatigue damage in the cladding during a 2000 mile trip, a single cask drop event could potentially consume a significant fraction of the cladding fatigue life. The cladding strains measured in the 30 cm drop tests represent roughly 1% to 10% of the cladding fatigue life. Therefore, a proper understanding of the fatigue damage from 1 drop must still be made.

Another area where PNNL has not completed analysis is that of the fuel assembly components, such as the guide tubes. Spacer grids were a primary concern this year because the drop tests demonstrated permanent deformation. A structural evaluation of guide tube response was not completed and needs to be included in future work to fill the stress profiles knowledge gap.

In summary, the horizontal case represents a loading scenario that causes peak strains in the cladding that maintain significant margin on yield and failure, compared to anticipated low-burnup material properties. There is no reason to expect any significant structural failures of the cladding or the fuel assembly structure in the 30 cm horizontal cask drop scenario. More work is needed to consider the high burnup condition and the local cladding failure criteria. Fatigue and assembly hardware also need to be considered. A plan for performing this work is presented in Section 7.3.

7.2 General Cask Drop Scenario

PNNL began exploring the general 30 cm drop scenario using the ENSA ENUN-32P cask and SNL's specific Westinghouse 17x17 PWR fuel assembly design. The analysis indicates that the horizontal drop case is not the most limiting, in terms of fuel rod cladding strains. The 60° impact angle case was most limiting, with cladding strains that were 4673 uE, or 76% higher than the peak cladding strain value calculated in the horizontal model (2650 uE) and 171% higher than the maximum recorded strain in the horizontal test (1,723 uE). While these are significant increases in strain, there still remains significant margin compared to low burnup yield and failure limits. As noted above, PNNL still needs to perform analyses of the high burnup condition and relate the calculated peak strain to cladding failure criteria.

The general case of the 30 cm cask drop involves many parameters that can affect the loading. A structural dynamic analysis of one drop event requires choosing a configuration from the following list. For example, the impact angle orientation can be any angle from 0° to 90°. The entire field of potential cask drops is enormous, so the results of this current study are valuable in defining the matrix of configurations to be simulated in the future. The goal should be to explore the following list as much as necessary to understand the range of fuel assembly loads.

<div align="center">

Configuration Parameters List
</div>

- Impact angle orientation
- Cask rotational orientation
- Fuel-to-basket gaps
- Cask design
- Fuel design
- SNF burnup
- SNF temperature

PNNL envisions using a damage model concept to assess these variables and to establish important trends. For example, the 60° impact angle was found to be most limiting, as detailed in Section 5.1.2.1 of this report. The exercise of finding the most limiting impact angle required a parametric study of the model that calculated an impact response for several cases with an impact angle between 0° and 90°. Section 6 describes the current state of development of the damage model and shows acceleration vs. impact angle, which is based on the modeling results from the impact angle parametric study. The damage model is envisioned to be able to generate a curve of peak cladding strain vs. impact angle, or any of the variables listed above.

Note that cask design and fuel design are the items on the list that would require the most analysis. All of the other items can be explored using the models already created. There are 17 cask designs in the US, and the most important one to model is a canister system. There are numerous fuel designs, and the most important one to model is a boiling water reactor (BWR) fuel assembly. For the BWR, it is important to model a fuel design that has partial-length fuel rods because previous modeling by the authors suggests that such fuel designs could be more vulnerable to damage because of their structure. The best way to populate the damage model is to cover the extreme cases, and then determine how many intermediate cases are needed.

Section 7.3 proposes an analytical study to complete the damage model.

7.3   Plan for Closing the NCT Stress Profiles Knowledge Gap

This section describes a plan for closing the NCT stress profiles knowledge gap over the next one to two years.

The first priority is to relate the as-tested horizontal drop scenario to a high burnup equivalent scenario. PNNL's fuel assembly model is validated against test data, so what remains is to update the material properties to represent a high burnup material condition and select configuration parameters from the configuration parameters list. Ideally, several configurations would be calculated, using the results of each analysis case to populate the damage model. This activity can be completed in one year.

The second priority is to address the general 30 cm drop scenario by exploring the configuration parameters list. This is where PNNL's expertise in developing automated analysis scripts (as was done by Klymyshyn et al. [2019] to perform 1600+ analyses) will allow us to explore large parametric variations to populate the damage model. An adequately populated damage model would enable the estimation of damage, stress, strain, acceleration, or any other important 30 cm cask drop parameter for the entire field of cask and fuel assembly designs. The SFWST program does not need the granularity of knowing the cask drop response of every conceivable cask and fuel combination, but the program needs to know the full range of behavior to inform SNF testing and to determine when the knowledge gaps are closed. This activity is viewed as a two-year effort, with the bulk of the damage model being completed in the first year, and the second year devoted to refining the tool. The first year would include creating models of a canister cask system and a BWR fuel assembly.

The third priority is to develop cladding failure criteria that are related to the stresses and strains calculated by the model, which assumes nominal geometry. This is where fuel cladding and pellet effects need to be considered including phenomena such as fuel fragmentation that has been observed in the Sibling Pin test program (see Saltzstein et al. 2020 for details of the Sibling Pin test campaign). The tests record strains and the fuel assembly level model calculates stress and strain. While these values are very useful, the ultimate goal is to determine if the cladding and other fuel assembly structural components are at the risk of failure. While the Sibling Pin test campaign is ongoing, and the test data are still being collected, we need to connect the fuel assembly level structural dynamic model results to the existing fuel segment level test data. The MMTT data were so low that there was no reason to take this step, but the 30 cm drop loads are high enough that this step is necessary. This activity is important because it provides data to the damage model so that it incorporates fuel cladding failure mechanisms. This activity can be executed concurrently with the ongoing Sibling Pin test campaign and lessons learned in modeling can inform the in-progress testing. This activity may need to continue after the Sibling Pin testing is complete in order to address all the issues raised in testing. The intent with this activity is to inform the damage model and ensure that the material scientists are getting the correct information about mechanical loading conditions.

8   REFERENCES

Adkins H, K Geelhood, B Koeppel, J Coleman, J Bignell, G Flores, J-A Wang, S Sanborn, R Spears, and N Klymyshyn. 2013. *Used Nuclear Fuel Loading and Structural Performance Under Normal Conditions of Transport – Demonstration of Approach and Results on Used Fuel Performance Characterization.* FCRD-UFD-2013-000325, Pacific Northwest National Laboratory, Richland, Washington.

Ammerman, D.J., Lum, C.C. "ENSA Impact Tests." SAND2011-0803P, Sandia National Laboratories, Albuquerque NM, 2011.

ANSYS, Inc. April 2017. ANSYS Mechanical User's Guide, Release 18.1. Canonsburg, Pennsylvania.

Barber, J.J. "Hertzian Contact." Contact Mechanics, Springer, 2018, pp. 37–37.

Geelhood, K.J., Beyer, C.E., Luscher, W.G. "PNNL Stress/Strain Correlation for Zircaloy." PNNL-17700, Pacific Northwest National Laboratory, Richland WA, 2008.

Jiang, H., J-A., J. Wang. 2016. "Spent Nuclear Fuel System Dynamic Stability Under Normal Conditions of Transportation." *Nuclear Engineering and Design.* Vol. 310, pp. 1–14.

Kalinina, E.A., Wright, C., Gordon, N., Saltzstein, S.J., Lujan, L., Norman, K.M. 2018. *Data Analysis of ENSA/DOE Rail Tests.* SFWD-SFWST-2018-000494, Sandia National Laboratories, Albuquerque, New Mexico.

Kalinina, E., D. Ammerman, C. Grey, M. Arviso, C. Wright, L. Lujan, G. Flores, S. Saltzstein. 2019. "30 cm Drop Tests." SAND2019-15256 R. Sandia National Laboratories, Albuquerque NM, 2019.

Kalinina, E., D. Ammerman, C. Grey, G. Flores M, L. Lujan, S. Saltzstein, D. Michel. 2020. "Surrogate Assembly 30 cm Drop Test." Sandia National Laboratories, Albuquerque NM, 2020.

Klymyshyn, N.A., Ivanusa, P., Kadooka, K., Spitz, C., Jensen, P.J., Ross, S.B., Hanson, B.D., Garcia, D., Smith, J., Lewis, S. "Modeling and Analysis of the ENSA/DOE Multimodal Transportation Campaign." PNNL-28088, Pacific Northwest National Laboratory, Richland WA, 2018.

Klymyshyn, N.A., Ivanusa, P. "Modeling and Analysis to Support Spent Nuclear Fuel Drop Tests." PNNL-29164, Pacific Northwest National Laboratory, Richland WA, 2019.

Klymyshyn N.A., P. Ivanusa, K. Kadooka, C.J. Spitz, E.D. Irick, P.J. Jensen, S.B. Ross, and B.D. Hanson. "Structural Dynamic Analysis of Spent Nuclear Fuel." PNNL-29150. Pacific Northwest National Laboratory, Richland WA, 2019.

LSTC (Livermore Software Technology Corporation). 2013. *LS-DYNA® Keyword User's Manual, Volume I, Version R7.0.* Livermore, California.

McConnell PE, R Wauneka, S Saltzstein, and K Sorenson. 2014. *Normal Conditions of Transport Truck Test of a Surrogate Fuel Assembly.* Sandia National Laboratories, Albuquerque, New Mexico.

NRC. NUREG–1864, ''A Pilot Probabilistic Risk Assessment of a Dry Cask Storage System at a Nuclear Power Plant'' U.S. Nuclear Regulatory Commission, Washington, DC. 2007.

Rashid, J., Wong, F., Dunham, R. 2007. Spent-Fuel Transportation Applications—Normal Conditions of Transport. EPRI TR 1015049. Final Report, June.

Sanders et al. "A Method for Determining the Spent Fuel Contribution to Transport Cask Containment Requirements." Sandia National Laboratories. SAND90-2406, 1992.

Saltzstein, S., Hanson, B, Sorensen, K. 2020. "Spent Fuel and Waste Science and Technology Storage and Transportation 5-Year R&D Plan." M2SF-20SN010201062. Sandia National Laboratories, Albuquerque, New Mexico.

Wang J-A, H Wang, H Jiang, Y Yan, BB Bevard, and JM Scaglione. 2016. *FY 2016 Status Report: Documentation of All CIRFT Data including Hydride Reorientation Tests*. ORNL/SR-2016/424, Oak Ridge National Laboratory, Tennessee. 2016.

APPENDIX A

CASK IMPACT STRUCTURAL DYNAMICS MODELING

A-1   Introduction

This appendix provides additional technical details and results from the cask impact model that were omitted from Section 2 for conciseness.

Section A-2 provides additional information about the 1/3-scale cask model used for validation studies. This includes additional detail about the LS-DYNA model (Section A-2.1) and the methodology used for model validation (Section A-2.2). Additional results from the validation studies are also discussed here, including more granular detail about the surrogate assembly response in the model and test (Section A-2.3) and results from validation relative to data from the 9 m drop tests conducted at SNL in 2010 (Section A-2.4).

Section A.3 provides additional information about the full-scale cask model studies. This includes additional detail about the LS-DYNA model (Section A-3.1) and the cask impact orientation study, including time histories for each of the five orientations selected for further analysis (Section A-3.2).

A-2   1/3-Scale Cask Model

A-2.1   *LS-DYNA Model Description*

This section provides additional detail about the 1/3-scale cask model that was briefly described in Section 2.1.1.

A cask model was developed and validated based on cask drop tests performed at SNL in 2010 (Ammerman and Lum 2011), and at BAM in 2018 (Kalinina et al. 2019). Both tests used 1/3-scale ENSA ENUN-32P dual-purpose casks and impact limiters.

An LS-DYNA model of the 1/3-scale cask and impact limiters was developed (Figure A.1) based on design drawings provided by ENSA, similar to the model previously used for pre-test and initial post-test modeling of the 30 cm drop test at BAM (Klymyshyn and Ivanusa 2019). The model simplifies the actual package geometry by representing the cask and two distinct impact limiter materials (polyurethane foam and aluminum honeycomb) as three homogenized regions represented by solid elements. By homogenizing otherwise complex geometry, a much larger time step can be used for explicit dynamics analyses, allowing the calculation to be done much more efficiently. Homogenization of the impact limiter material, skin, and gussets is validated by comparison against test data. The cask is a rigid structure that undergoes very little deformation, so homogenization of the cask body, neutron absorber material, lid, and fasteners has a negligible effect on its response. The basket structure is approximated using shell elements rather than the solid elements in the previous model. The surrogate assemblies are slightly simplified in the model; the hollow, slotted assemblies used in the test are represented in the model by solid rectangular prisms that have identical overall dimensions, mass, and flexural rigidity.
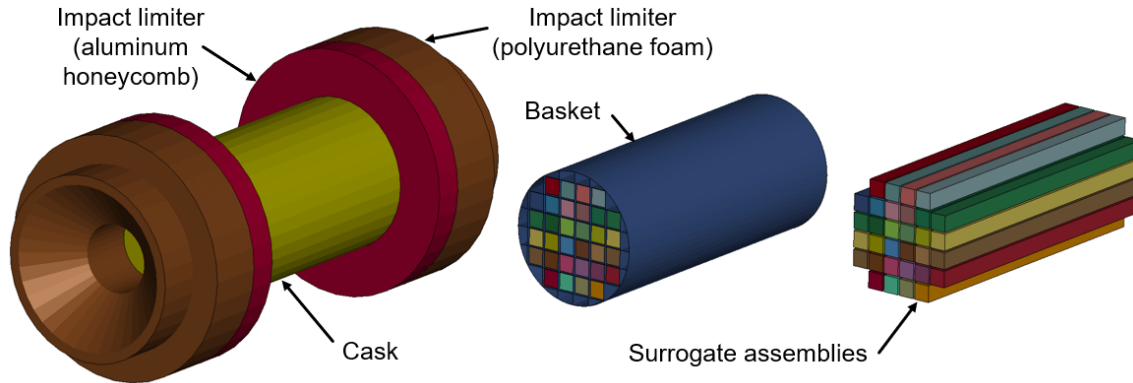
Figure A.1. LS-DYNA Model of the 1/3-Scale ENSA ENUN-32P Cask and Impact Limiters

The material density of each of the components was set to match total component masses on the ENSA design drawings to within 1% (Table A.1). The cask, basket, and surrogate assemblies were given the elastic properties of steel, the major structural material of each. The cask material incorporates piecewise linear plasticity (*MAT_PIECEWISE_LINEAR_PLASTICITY), while the basket and surrogate assemblies use a linear elastic material model (*MAT_ELASTIC). The impact limiters incorporate the *MAT_MODIFIED_HONEYCOMB material model and assume isotropic stiffness and crush strength. The crush strength and volume fraction at full compaction for the polyurethane foam and aluminum honeycomb are best estimates based on a range of test and manufacturer data for the actual materials, Last-A-Foam (McMurty and Honestreiter 1995; Alcore, Inc. 2003). The ground is modeled as an unyielding, rigid body with the contact stiffness of steel.

Table A.1. Approximate Mass of 1/3-Scale Cask Components

Component	Mass (kg)
Impact Limiters (total)	614
Cask	3248
Basket	346
Surrogate assemblies (each)	27

Initial velocity was applied to all nodes of the package and its contents to simulate the velocity of the cask just before impact (2.43 m/s in the 30 cm drop, and 13.3 m/s in the 9 m drops). A constant acceleration field was also applied to simulate gravity.

A contact algorithm (*CONTACT_AUTOMATIC_SINGLE_SURFACE) was used to account for contact within the model, including between the cask and ground, and cask cavity and internals. Tied contact (*CONTACT_TIED_NODES_TO_SURFACE) was used to simulate the connection between the cask and the impact limiters. Approximately 1% stiffness damping was applied to the model for numerical stability.

A-2.2 *Validation Data and Impact Limiter Material Property Selection*

This section provides additional details about the validation methodology and impact limiter property selection that was briefly summarized in Section 2.1.2.

In the SNL and BAM drop tests, the following five different drop conditions relevant to this work were evaluated. The drop orientations are represented in Figure A.2.

1. **30 cm side drop:** Performed at SNL and BAM. At BAM, two tests were performed where the basket was unrotated (basket cell floors parallel to the ground), and rotated 45° around its longitudinal axis.

The BAM test was performed with the cask at room temperature. The SNL test was performed with the cask chilled to approximately -29°C. Because the test results were very similar, and because the BAM test also instrumented the cask internals, the BAM 30 cm drop was used for validation.

2. **9 m side drop:** Performed at SNL, with the cask chilled to approximately -29°C.

3. **9 m end drop:** Performed at SNL, with the cask chilled to approximately -29°C.

4. **9 m slapdown (10° from horizontal):** Performed at SNL, both chilled (to approximately -29°C) and heated (to approximately 100°C).

5. **9 m CG over-corner drop (69° from horizontal):** Performed at SNL, with the cask heated to approximately 100°C.
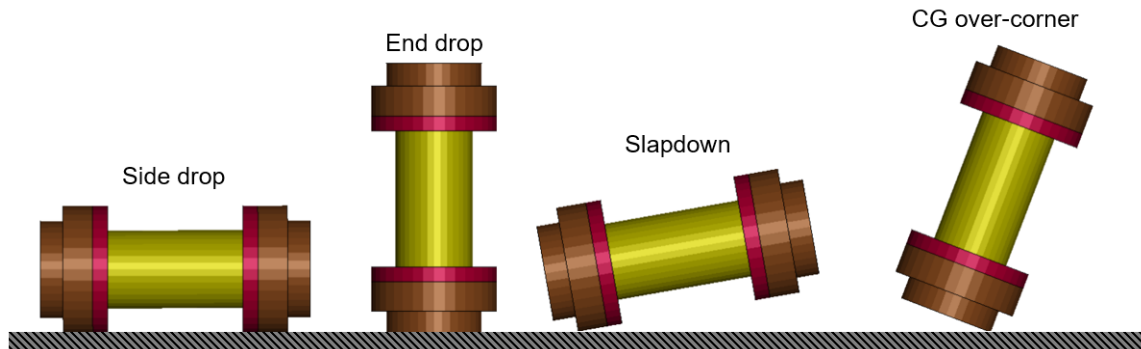
Figure A.2. Drop Orientations Represented in the Validation Data

This list does not include the 1 m side and end puncture tests conducted at SNL, because they were conducted to test the integrity of the cask, rather than the shock imparted to it. Moreover, these puncture tests produced package accelerations that were similar to or more benign than their non-puncture test counterparts.

The impact limiter parameters in the cask model were chosen to match the cask deceleration magnitudes measured in the drop tests. The cask deceleration was chosen as the dependent variable in this study, because it determines the load imparted on the SNF. The impact limiter material response is most important in determining the cask deceleration, because it is the main means of energy absorption during an impact.

Two material properties of the impact limiters were identified as key parameters that affect the dynamics of the model—volume fraction at full compaction (abbreviated as "VF") and crush strength. With the two impact limiter materials of polyurethane foam and aluminum honeycomb, this gives a total of four variables that must be determined from the test data. Ranges for each of these properties are available in the literature (Table A.2). Because the impact limiters in the cask model are homogenized and do not resolve details such as the thin impact limiter skin and internal gussets, it is acknowledged that some deviation from the literature values may occur.

Table A.2. Range of Material Properties for Impact Limiter Materials

	Volume Fraction at Full Compaction	**Crush Strength (MPa)**
Polyurethane foam (Last-A-Foam)	0.47-0.48 (McMurtry 1995)	5.2-15.6 (McMurtry 1995)
Aluminum honeycomb (Trussgrid)	0.22-0.25 (McMurtry 1995)	0.69-6.00 (Alcore 2003)

A strategy was developed for selecting the parameters listed in Table A.2 from the known range, based on the known loading direction and intensity of each of the test cases. For instance, the 30 cm side drop tests yielded little permanent deformation, meaning that VF had little, if any, effect on the impact behavior, and the response is set by the crush strength. In the 9 m end drop, the response is set by the polyurethane foam properties exclusively. On the other hand, the side drop and slapdown response is set by both the polyurethane foam and the aluminum honeycomb properties, because both are compressed in a horizontal drop. The following stepwise strategy was used to achieve the best fit between the test and model behavior:

1. Adjust the VF and crush strength of the polyurethane foam to approximately match the 9 m end drop test data.

2. Adjust the crush strength of the aluminum honeycomb to approximately match the 30 cm side drop test data.

3. Adjust the VF of both impact limiter materials to approximately match the 9 m side drop and slapdown test data.

Emphasis was put on matching the deceleration of the cask CG or average accelerometer response, rather than the deceleration of individual accelerometers on various points on the cask. While the individual accelerometers were used to inform the material property selection process, the cask CG was used as the main metric because it smooths any spurious response of individual accelerometers.

A-2.3   *Additional Validation Results – BAM 30 cm Drops*

This section provides additional details about the validation study for the BAM 30 cm drop. In particular, it provides more granular detail about the surrogate assembly accelerations in the model and test.

Accelerations of the surrogate assemblies were used to validate the elastic properties of the basket and surrogate assemblies. In the BAM test, 11 of the 32 surrogate assemblies were instrumented with accelerometers, mounted at the lid end or bottom end of the assembly, and in some cases, at both ends. For comparison, accelerations at each end of the surrogate assemblies were calculated in the model. These data are aggregated in Table 2.2 of Section 2.1.3. Table A.3 and Table A.4 provide cell-by-cell detail of the surrogate assembly accelerations in the non-rotated and rotated configurations, respectively.

Table A.3. **Comparison of Model and Test Surrogate Assembly Acceleration, Non-rotated Configuration. Impact occurs on the bottom edge of the basket cell plots.**

Lid End (BAM Test Data):

	117	148	N/A	N/A	
N/A	N/A	162	130	N/A	N/A
N/A	N/A	103	N/A	N/A	N/A
N/A	N/A	124	N/A	N/A	N/A
102	N/A	N/A	N/A	N/A	N/A
	85	N/A	N/A	85	

Bottom End (BAM Test Data):

188	245	N/A	173		
N/A	N/A	N/A	N/A	N/A	N/A
N/A	N/A	N/A	N/A	N/A	N/A
N/A	N/A	N/A	N/A	N/A	N/A
177	N/A	N/A	N/A	N/A	106
161	N/A	N/A	127		

	Test	Model
Lid ave	117.3	95.1
Bottom ave	168.0	136.8
Overall ave	139.5	115.9
Lid peak	161.9	154.4
Bottom peak	244.6	232.0

Lid End (Model):

118	103	110	130		
120	109	152	121	40	154
68	91	94	100	62	150
59	54	55	73	77	101
61	112	56	69	107	80
69	152	122	76		

Bottom End (Model):

111	152	175	148		
149	113	145	144	129	127
169	151	162	232	148	147
128	114	181	201	82	96
104	101	81	75	130	105
106	179	173	121		

Table A.4. **Comparison of Model and Test Surrogate Assembly Acceleration, Rotated Configuration. Impact occurs on the bottom left corner of the basket cell plots.**

Lid End (BAM Test Data):

167	119	N/A	61		
N/A	N/A	136	136	N/A	N/A
N/A	N/A	135	N/A	N/A	N/A
N/A	N/A	119	N/A	N/A	N/A
85	N/A	N/A	N/A	N/A	N/A
76	N/A	N/A	82		

Bottom End (BAM Test Data):

198	224	N/A	127		
N/A	N/A	N/A	N/A	N/A	N/A
N/A	N/A	N/A	N/A	N/A	N/A
N/A	N/A	N/A	N/A	N/A	N/A
118	N/A	N/A	N/A	N/A	87
164	N/A	N/A	172		

	Test	Model
Lid ave	111.8	107.3
Bottom ave	155.9	147.2
Overall ave	129.9	127.2
Lid peak	167.2	162.8
Bottom peak	223.8	229.3

Lid End (Model):

106	91	123	108		
78	98	100	108	109	112
64	107	97	105	135	131
106	115	90	82	105	100
141	100	106	141	114	163
86	116	110	87		

Bottom End (Model):

210	45	103	184		
150	192	111	153	224	189
110	220	182	146	126	89
115	118	90	191	151	85
90	105	212	163	219	229
70	93	208	136		

A-2.4 *Additional Validation Results – SNL 9 m Drops*

This section provides additional detail about the validation of the model to the 9 m drop tests conducted at SNL in 2010, that were introduced in Section 2.1.4 and briefly summarized in Table 2.3 of that section. These tests are not discussed at length in the main body of this report, because the main focus

of this work is the 30 cm drop. However, validation relative to the 9 m drop data is useful because it would allow the model to be used for hypothetical accident conditions in future work. The four 9 m drop conditions (side, end, slapdown, and CG-over-corner) are discussed in the following sections.

A-2.4.1 *9 m Side Drop*

In the 9 m side drop, the cask was dropped from that height (13.3 m/s impact velocity), oriented horizontally. Unlike the 30 cm drop at BAM, the basket was not instrumented with accelerometers, so data to estimate the initial gap between the cask and internals were not available. The small initial gap from the 30 cm drop was retained for this model. A comparison of the model and test acceleration time histories is shown in Figure A.3.
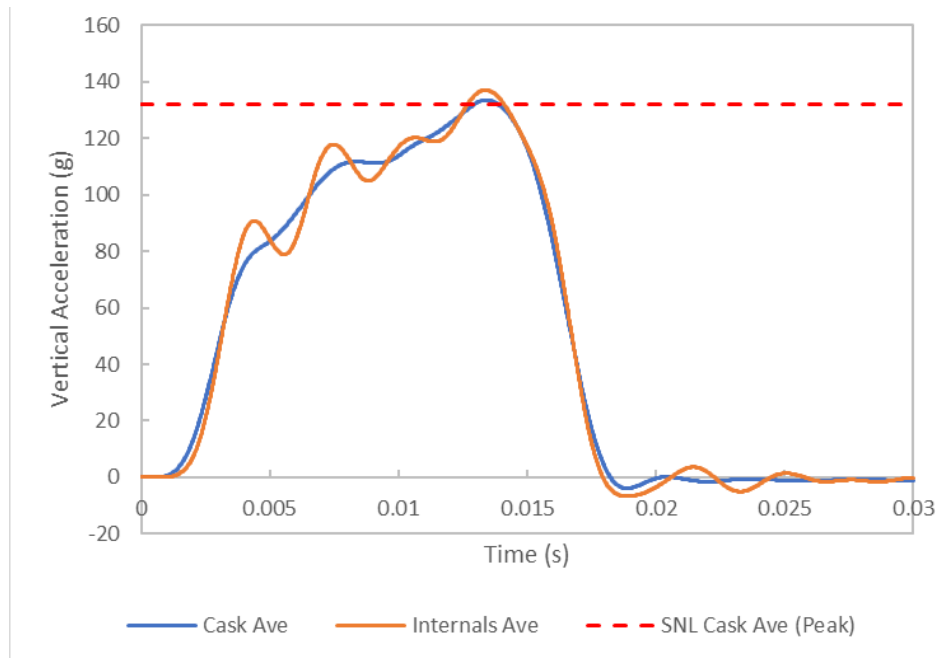
Figure A.3. Comparison of Model and Test Data in the 9 m Side Drop

Very good agreement was obtained between model and test, with a difference of just 1% (134 g peak cask CG acceleration in the model, versus 132 g in the test).

A-2.4.2 *9 m End Drop*

In the end drop test, the cask was dropped from a height of 9 m (13.3 m/s impact velocity), oriented vertically. The initial gap between the internals and cask cavity was fully closed for this and the subsequent analyses. This assumption produces conservative results with respect to the selected impact limiter properties, because smaller initial gaps tend to reduce the acceleration of the system.

Good agreement was observed between the model and test (Figure A.4), with a difference of 9% (113 g peak cask CG acceleration in the model, versus 104 g in the test).
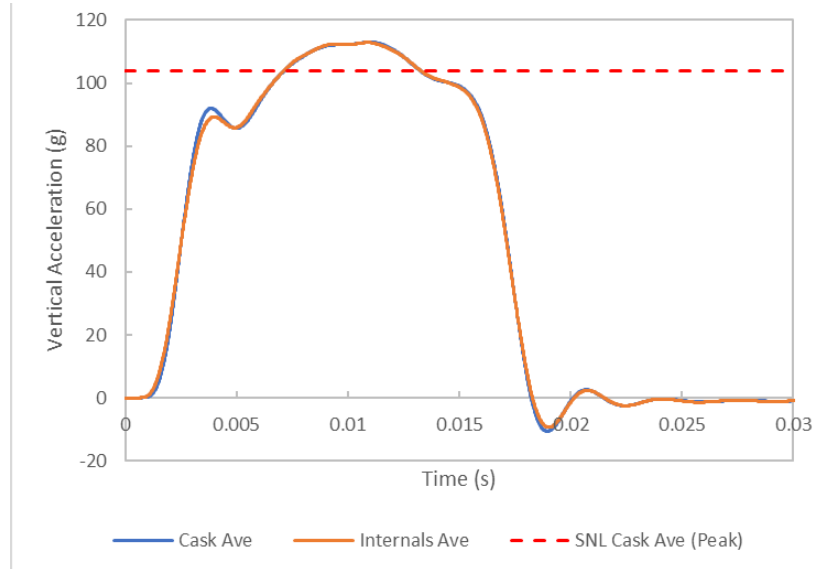
Figure A.4.   Comparison of Model and Test Data in the 9 m End Drop

A-2.4.3   *9 m Slapdown*

In the slapdown test, the cask was dropped from a height of 9 m (13.3 m/s impact velocity) with an initial rotation of 10° from horizontal.

Very good agreement was observed between model and test (Figure A.5), with a difference of 5% in the magnitude of the secondary impact (86 g peak cask CG acceleration in the model, versus 82 g in the test). There was also good agreement in the primary impact (57 g in the model, versus 60 g in the test).
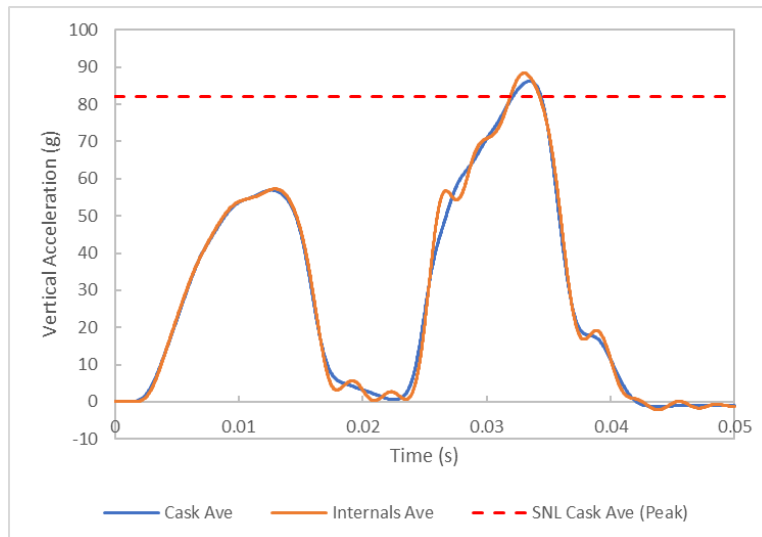
Figure A.5.   Comparison of Model and Test Data in the 9 m Slapdown

A-2.4.4   *9 m Corner Drop*

In the corner drop test, the cask was dropped such that the cask CG was positioned over the initial point of impact to cause tipping and secondary impact to occur. The cask was dropped from a height of 9 m (13.3 m/s impact velocity) with an initial rotation of 69° from impact (the actual value measured in the SNL test, rather than the 71° nominally specified in the test plan).

Very good agreement was observed between the model and test (Figure A.6), with a difference of 1% (89 g peak cask CG acceleration in the model, versus 90 g in the test). A smaller, secondary impact associated with tipping of the cask was also modeled, but no test data were available for comparison.
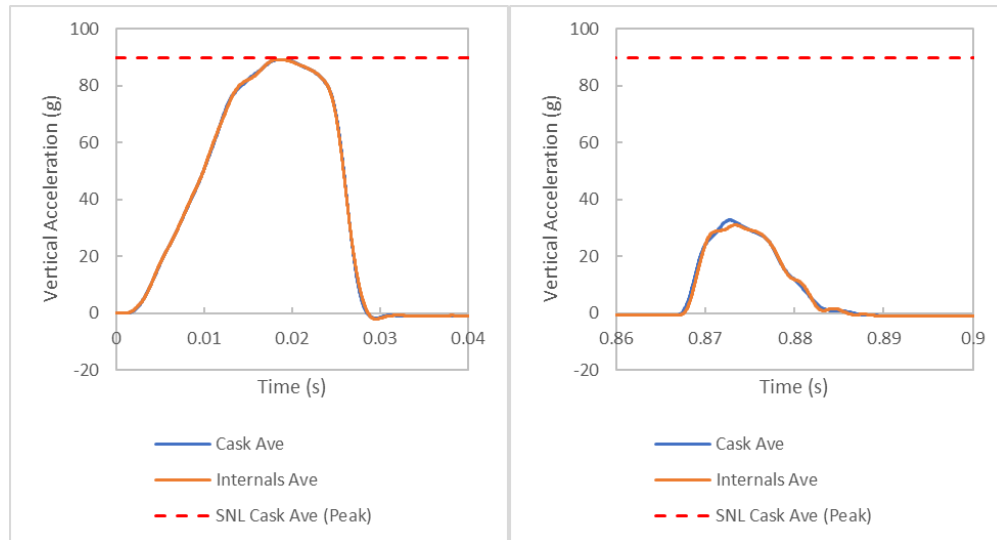
Figure A.6.   Comparison of Model and Test Data in the 9 m Corner Drop

A-3   Full-scale Model Studies

A-3.1   *LS-DYNA Model Description*

This section provides additional detail about the full-scale cask model that was briefly described in Section 2.2.

The 1/3-scale ENSA ENUN-32P cask model developed and validated in this work was converted to a full-scale package by adjusting the model dimensions to match full-scale design drawings provided by ENSA. The full-scale model is virtually identical in appearance to the 1/3-scale model shown in Figure 6-1. Material densities were calculated to match the known mass of components to within 1% (Table A.5). Material properties of the impact limiter materials are identical to the 1/3-scale model because material grain size and their associated properties are not adjusted for scale in actual testing. The surrogate assemblies were given the mass, inertia, and flexural rigidity identical to the 17x17 PWR fuel model described in Appendix B, in order to simulate their dynamics. All other aspects of the model, such as stiffness damping, gravity, and contact algorithm, remain unchanged.

Table A.5.   Approximate Mass of Full-scale Cask Components

Component	Mass (kg)
Impact Limiters (total)	16488
Cask	93516
Basket	9394
Surrogate assemblies (each)	741

A-3.2   *Additional Model Output – Cask Impact Orientation Study*

This section provides further detail about the cask impact orientation study described in Section 2.2.1. The peak cask accelerations for each of the 19 different cask orientations are summarized in Figure 2-5 of that section, but the individual time histories were not shown, for conciseness. Figure A.7 through Figure

A.12 show the acceleration time history for each of the five cask orientations selected in that section for further downstream analyses.

The results are reported in the same local coordinates used in the main body of this text. These are X' (axial to the fuel) and Z' (lateral to the fuel).
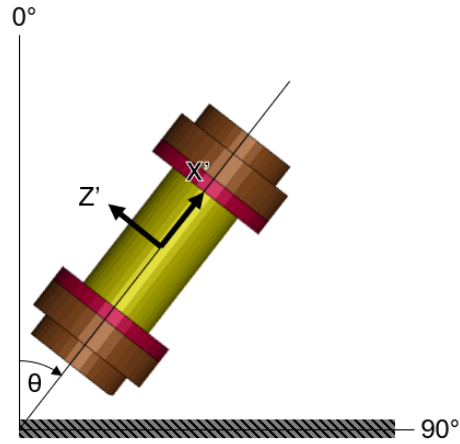
Figure A.7. Coordinate System for Cask Drop Orientation Study
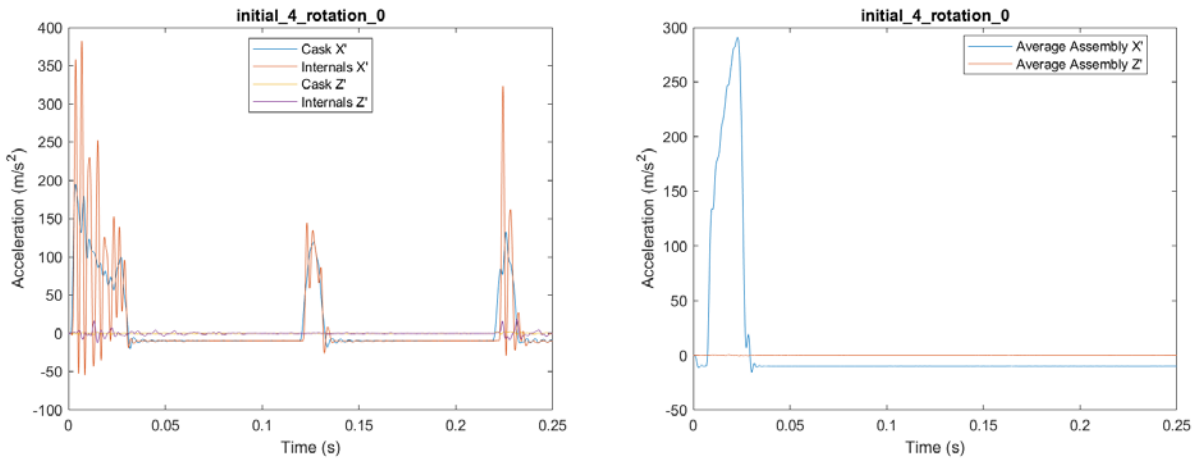
Figure A.8.   Acceleration Time History for the Cask and Basket (labeled as "internals") (left), and Surrogate Assemblies (right) in 0° Drop Orientation
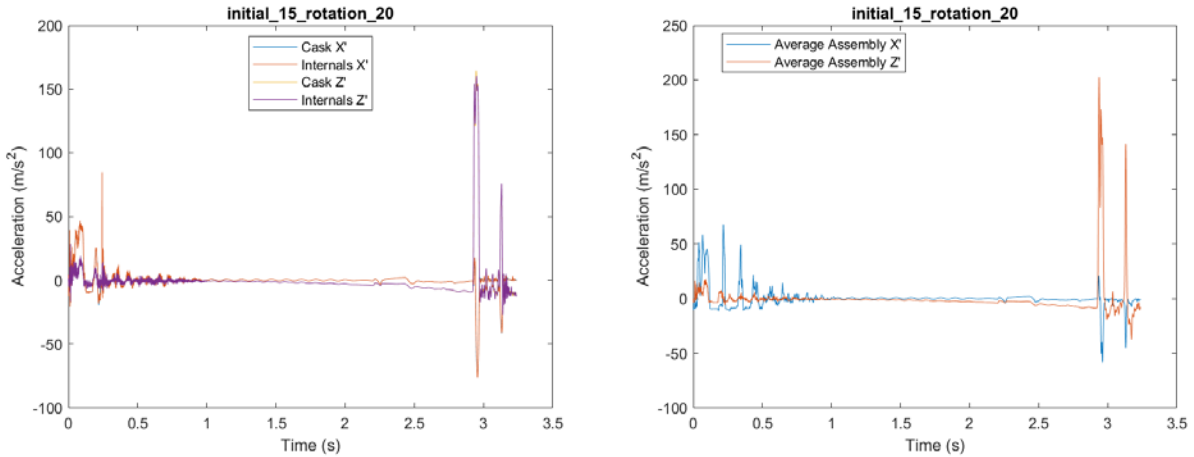
Figure A.9. Acceleration Time History for the Cask and Basket (labeled as "internals") (left), and Surrogate Assemblies (right) in 20° Drop Orientation
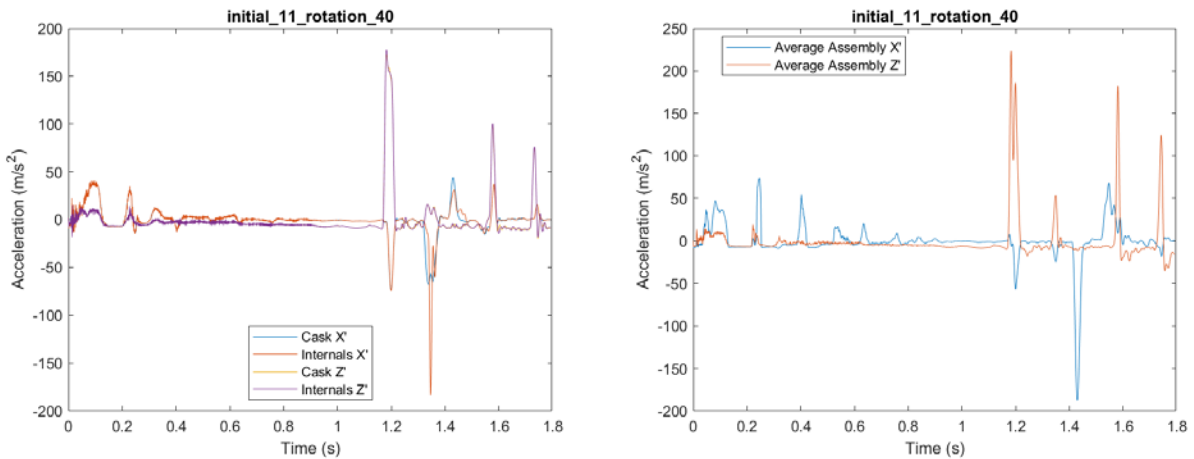
Figure A.10. Acceleration Time History for the Cask and basket (labeled as "internals") (left), and Surrogate Assemblies (right) in 40° Drop Orientation
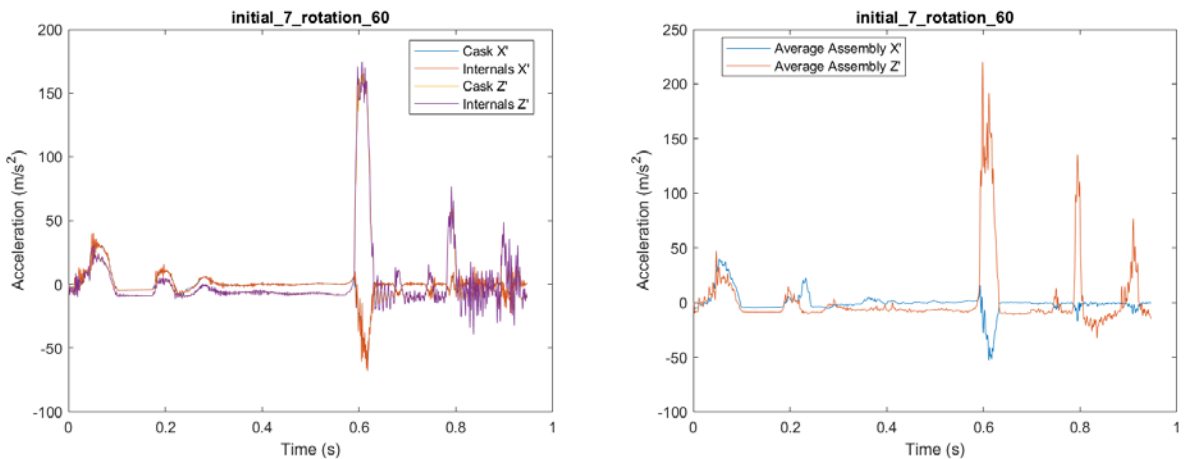
Figure A.11. Acceleration Time History for the Cask and Basket (labeled as "internals") (left), and Surrogate Assemblies (right) in 60° Drop Orientation
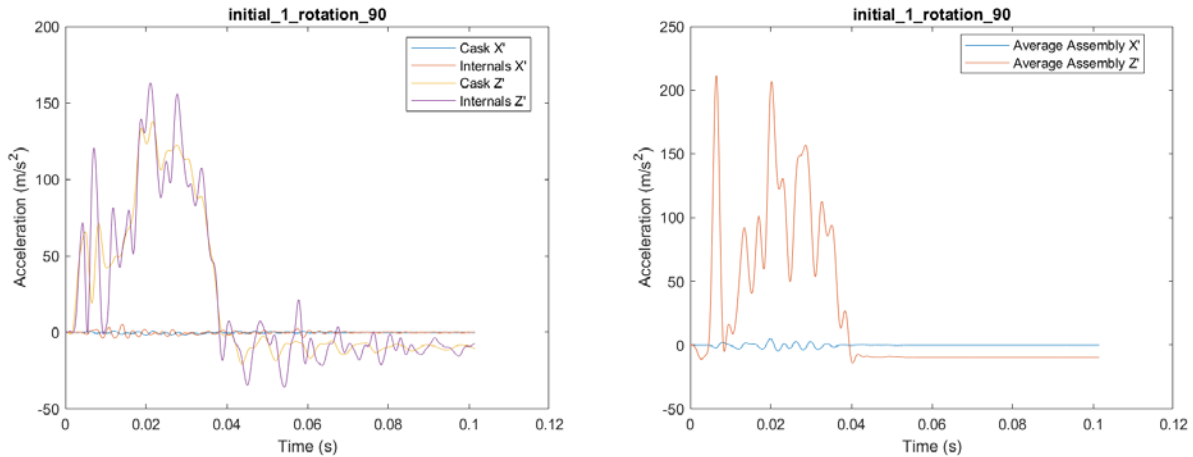
Figure A.12.   Acceleration Time History for the Cask and Basket (labeled as "internals") (left), and Surrogate Assemblies (right) in 90° Drop Orientation

A-4   References

Alcore, Inc. "Product Data Sheet, Trussgrid Three-Dimensional Honeycomb." January 2003. https://www.thegillcorp.com/alcore/datasheets/truss_0600.pdf. Accessed March 25, 2020.

Ammerman, D.J., Lum, C.C. "ENSA Impact Tests." SAND2011-0803P, Sandia National Laboratories, Albuquerque NM, 2011.

Kalinina, E., D. Ammerman, C. Grey, M. Arviso, C. Wright, L. Lujan, G. Flores, S. Saltzstein. 2019. "30 cm Drop Tests." SAND2019-15256 R. Sandia National Laboratories, Albuquerque NM, 2019.

Klymyshyn, N.A., Ivanusa, P. "Modeling and Analysis to Support Spent Nuclear Fuel Drop Tests." PNNL-29164, Pacific Northwest National Laboratory, Richland WA, 2019.

McMurtry, W.M., Hohnstreiter, G.F. "Impact Limiter Test of Four Commonly Used Materials and Establishment of an Impact Limiter Data Base." SAND95-0375C, Sandia National Laboratories, Albuquerque, NM, 1995.

This page is intentionally left blank.

APPENDIX B

CRUSHABLE GRID FUEL ASSEMBLY MODEL

B-1   Introduction

This appendix provides additional technical details and results from the crushable grid fuel assembly model omitted from Sections 4.2 and 5.1 for conciseness.

Section B.2 provides additional information about the LS-DYNA crushable grid fuel assembly model. Section B.3 provides additional information about the fuel assembly response in the numerous generic 30 cm drop analyses conducted in this work.

B-2   LS-DYNA Model Description

This section provides additional detail about the crushable grid fuel assembly model that was introduced in Section 4.2.1.

An LS-DYNA model of the 17x17 PWR fuel assembly used in the SNL assembly drop test was developed based on the "full fuel assembly model" that had been previously used in pre- and post-test modeling of the MMTT (see Klymyshyn et al. 2018, Section 3 and Appendix C). That model had been adapted from similar models used in previous works such as shaker table and truck test simulations (Klymyshyn et al. 2014) and has a long pedigree for modeling cladding strains in NCT conditions.

The model developed for the current work follows the same overall geometry (Figure B.1) and material models as the previous work, with a few exceptions. Most notably, the spacer grids are designed in the model to realistically buckle and deform. This is in contrast to previous fuel assembly models, which used a coarse representation of the spacer grids that did not attempt to resolve such behavior during lateral loading. That was not necessary for modeling most NCT scenarios, because the lateral loads were too small to cause significant or permanent deformation of the fuel assembly. On the other hand, the SNL assembly drop clearly demonstrated that grid crushing can occur during a drop event. This is important to model because the grid forms a part of the load path to the fuel in a lateral impact. A grid that buckles and crushes will convert more of the kinetic energy of a lateral impact into elastic and plastic strain energy than an elastic grid. In addition, as a grid crushes, the fuel rod pitch decreases, changing the boundary condition of the rod and increasing its proximity to other rods for rod-to-rod impact.
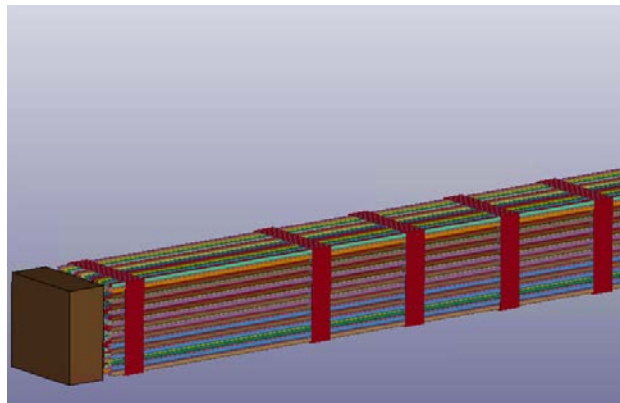
Figure B.1. Fuel Assembly Model with Crushable Grids

Several different ways of representing the grid in the finite element model were investigated, as illustrated in Figure B.2. Previous models used coarse shell elements to represent the grid (Figure B.2, top

left), which precludes realistic buckling behavior due to the overly stiff representation. A much finer shell mesh was briefly investigated (Figure B.2, top right) that represented the various springs, dimples, slots, and spot welds that make up a typical grid. Some success was achieved in modeling small sections of a fuel assembly, such as a 5x5 section as shown in Figure B.2, but this model proved to be much too computationally expensive to run, especially for a full 17x17 fuel assembly.
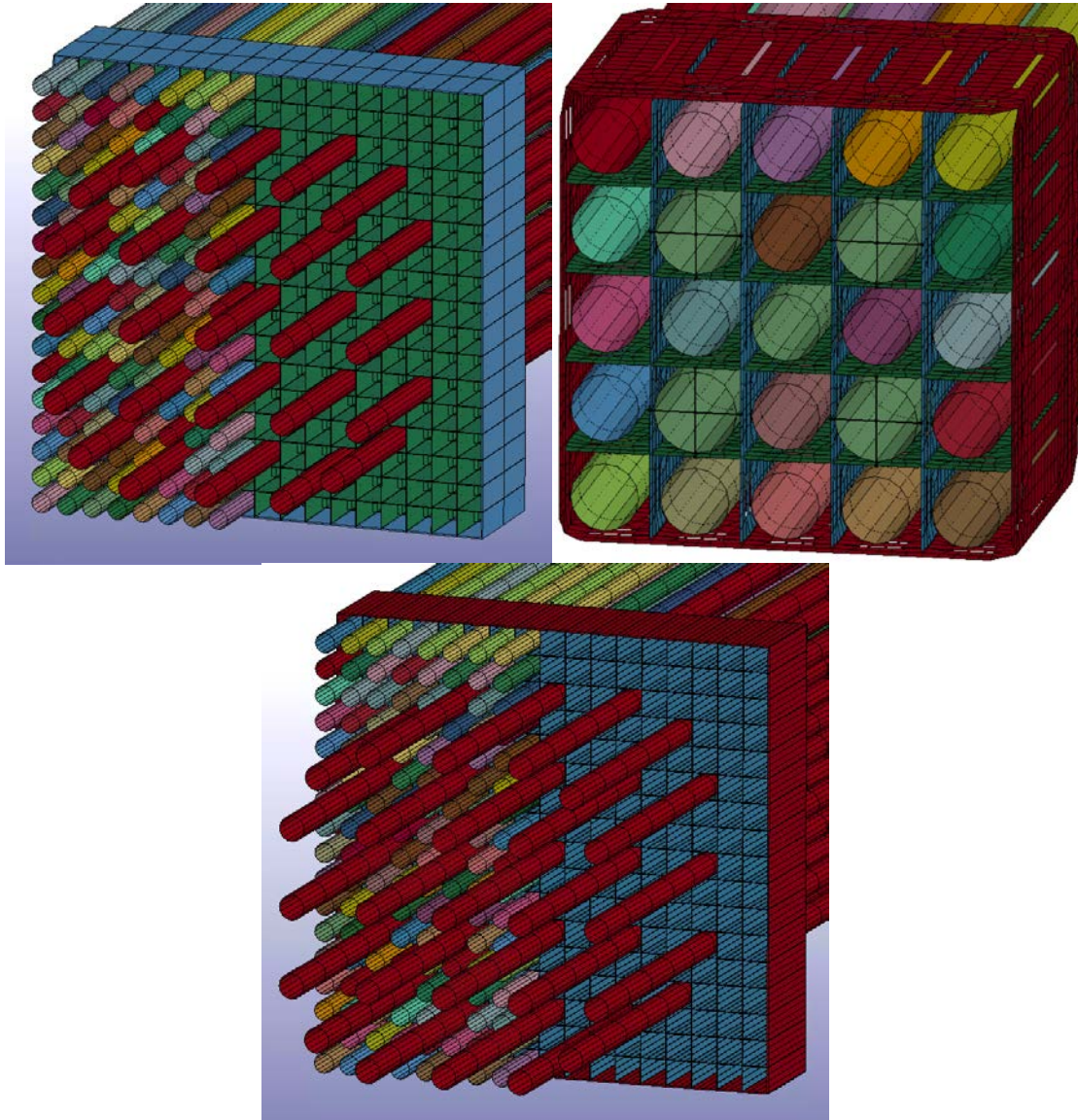
Figure B.2. Comparison of Various Grid Representations, Coarse Shell Mesh (top left), Fine Shell Mesh (top right), and Beams (bottom)

Finally, it was found that modeling the grid using beam elements (*ELEMENT_BEAM), four elements to each side of a grid cell, provided reasonably realistic grid buckling behavior without detailed modeling of the actual grid geometry (Figure B.3). Instead of directly modeling fine geometric details, the elastic modulus, yield strength, and tangent modulus of the grid material were chosen to produce the correct amount of buckling and residual deformation. The elastic modulus sets the initial elastic response, while the yield strength and tangent modulus set the onset and extent of plastic buckling. The SNL assembly drop was used as a benchmark for the crushable grid material properties, and the parameters were selected to match the test observations, using the known material properties of Zircaloy-4 as a

starting point. The grid buckling in the model and test are compared in Section 4.2.2. As shown in Figure B.3, the fuel rods are connected to the grids by discrete beams that represent the nonlinear stiffness characteristics of the springs and dimples, as detailed by Klymyshyn et al. (2014). The guide tubes are connected to the grids using spot weld constraints (*CONSTRAINED_GENERALIZED_WELD_SPOT).
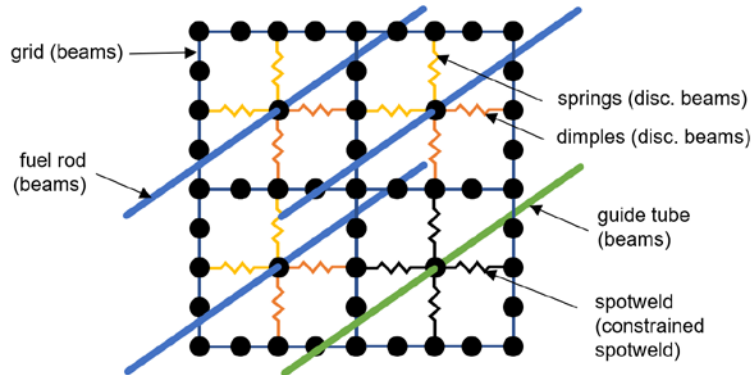
Figure B.3.   Finite Element Representation of the Grids and Grid-rod Connections

For the studies in this work, the fuel assembly was confined by a rigid basket cell (Figure B.4), based on dimensions derived from ENSA design drawings. This provides equivalent boundary conditions for the SNL assembly drop test and the shipping configuration in the ENSA ENUN-32P cask (the same configuration used in the cask impact model in this work). The model was loaded by applying translational and rotational time histories to the rigid basket (*BOUNDARY_PRESCRIBED_MOTION_RIGID). The time histories were either calculated from test data (in the SNL assembly drop model) or from the cask impact model (in the generic 30 cm drop analysis). Constant acceleration due to gravity was applied to the model as well (*LOAD_BODY).
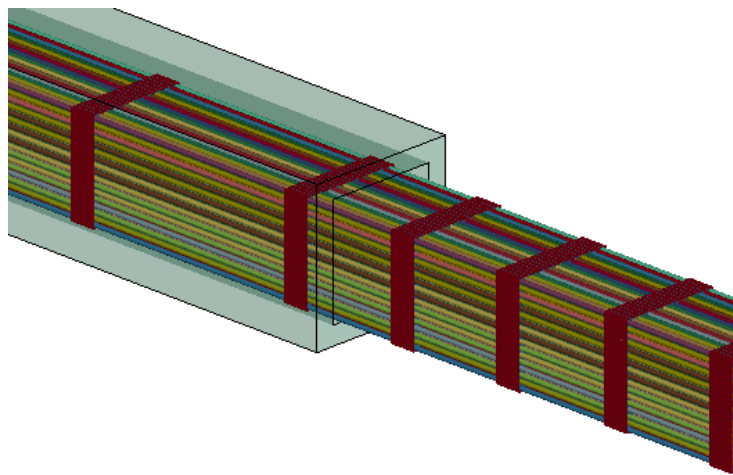
Figure B.4.   Fuel Assembly Model in Basket Cell (sectioned for illustrative purposes)

A variety of contact algorithms were used to simulate contact between various parts of the model. *CONTACT_AUTOMATIC_GENERAL was used to capture contact throughout the model, including beam-to-beam and beam-to-surface contact. The other type of contact in the model was *CONTACT_TIED_NODES_TO_SURFACE, which was used to connect the guide tubes to the top and bottom nozzles.

Approximately 1% mass damping was applied to the model (*DAMPING_GLOBAL) for numerical stability. Approximately 5% stiffness damping (*DAMPING_PART_STIFFNESS) was applied to the

grids, fuel rods, and guide tubes. This was done in an attempt to suppress the effect of the higher order bending mode seen in the model, but not in the test data (discussed in Section 4.2.3). The total amount of damping in the model is about 5–6% of critical damping, which is toward the upper end of damping typical for fuel assembly models (as discussed in Appendix C of Klymyshyn et al. (2014)). Comparisons of damping in the model and damping observed during the test were not a part of this work and so should be investigated in the future.

B-3   Additional General 30 cm Drop Simulation Results

This section provides additional detail about the generic 30 cm drop simulations and sensitivity studies that were discussed in Section 5.1. Contour plots of the cladding strain time corresponding to the time of peak strain, as well as the time histories of the element exhibiting the peak strain, are presented in the following sections. Table B.1 summarizes the fuel assembly drop simulations performed in this work, as well as the relevant sections in which the results are discussed.

Table B.1. Summary of SNF 30 cm Drop Analysis Conducted in this Work

Set	Time History	Basket-fuel Gap	Cladding Properties	Peak Cladding Strain (uE)	Peak Grid Crush (mm)	Section in this Work
SNL drop	Basket time history from test	4 mm (18% lateral gap)	Room temperature, unirradiated	2653	5.5	4.2.2
Potentially adverse drop conditions and reference cases	0° cask (end drop)	260 mm (99% longitudinal gap)		1133	0.0	5.1.2.1
	20° cask (CG-over-corner)	22 mm (99% lateral gap)		4651	16.6	5.1.2.1
	40° cask	22 mm (99% lateral gap)		4515	14.9	5.1.2.1
	60° cask	22 mm (99% lateral gap)		4673	12.0	5.1.2.1
	90° cask (side drop)	22 mm (99% lateral gap)	Room temperature, 10 GWd (low burnup)	3122	5.7	5.1.2.1
Windowed analysis check	60° cask, initial impact	0.2 mm (1% lateral gap)		368	0.0	5.1.2.2
		22 mm (99% lateral gap)		1562	0.0	5.1.2.2
Basket-fuel gap sensitivity study	0° cask (end drop)	2.6 mm (1% longitudinal gap)		1103	0.0	5.1.2.3
		130 mm (50% longitudinal gap)		848	0.0	5.1.2.3
	90° cask (side drop)	0.2 mm (1% lateral gap)		924	0.0	5.1.2.3
		11 mm (50% lateral gap)		2771	5.0	5.1.2.3

Set	Time History	Basket-fuel Gap	Cladding Properties	Peak Cladding Strain (uE)	Peak Grid Crush (mm)	Section in this Work
Fuel assembly orientation sensitivity study	90° cask (side drop)	0.2 mm (1% lateral gap)		944	0.0	5.1.2.4
		11 mm (50% lateral gap)		2618	6.7	5.1.2.4
		22 mm (99% lateral gap)		2603	9.2	5.1.2.4
Effects of cladding temperature	90° cask (side drop)	22 mm (99% lateral gap)	200°C, 10 GWd (low burnup)	3319	6.0	5.1.2.5

B-3.1   *Potentially Adverse Drop Conditions and Reference Cases*

Figures B.5 through B.16 present additional model results from the potentially adverse drop conditions and reference cases discussed in Section 5.1.2.1, including strain contour plots, the time history of the element with maximum strain, and shape of the deformed grids for each of the analyzed drop orientations.
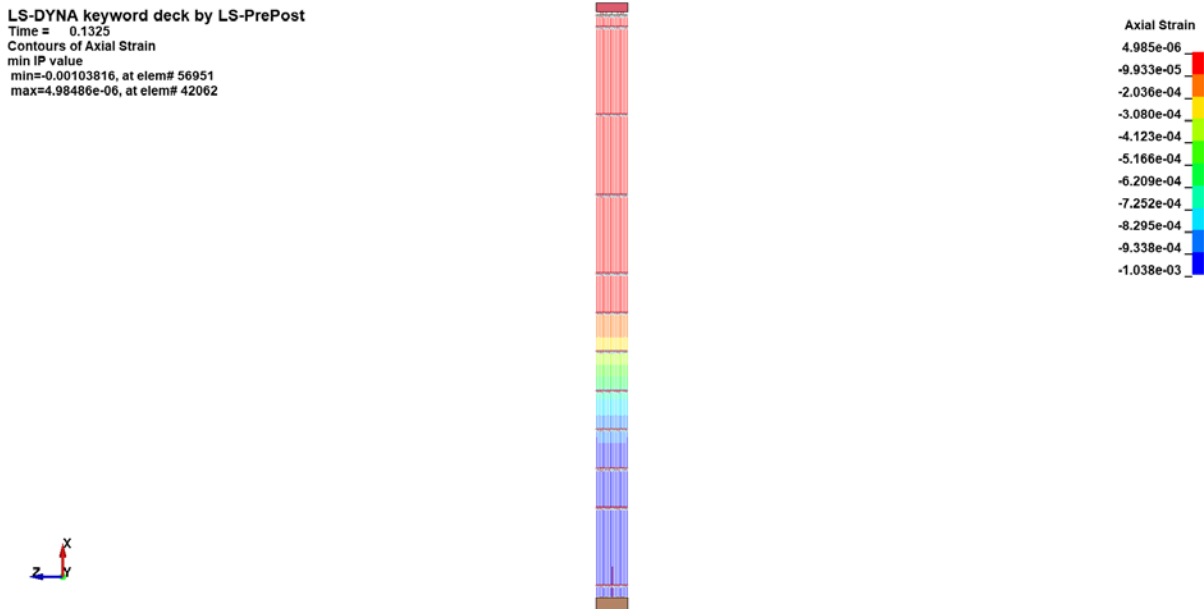
Figure B.5.   Contours of Cladding Strain, at Time of Peak Strain in the 0° (End Drop) Orientation
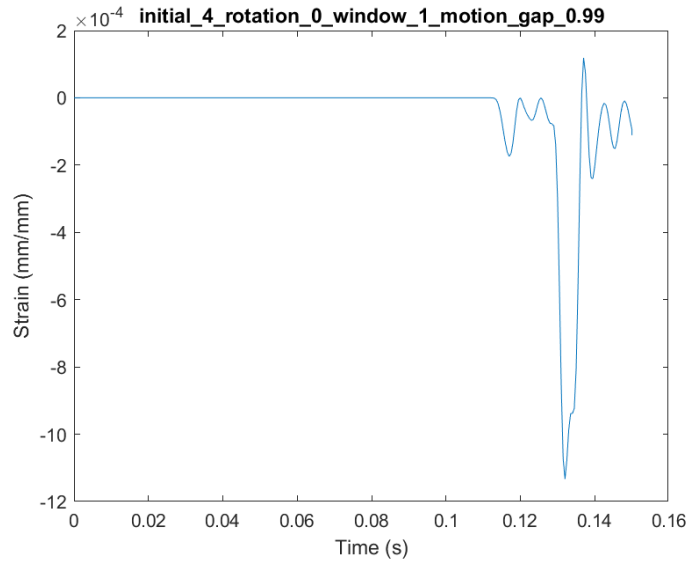
Figure B.6.   Strain Time History in Element with Peak Strain in the 0° (End Drop) Orientation
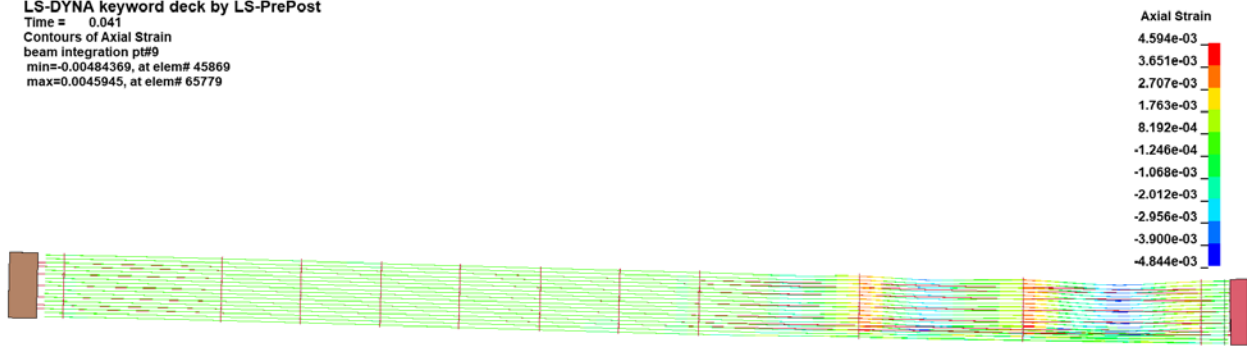
Figure B.7.   Contours of Cladding Strain, at Time of Peak Strain in the 20° (End Drop) Orientation
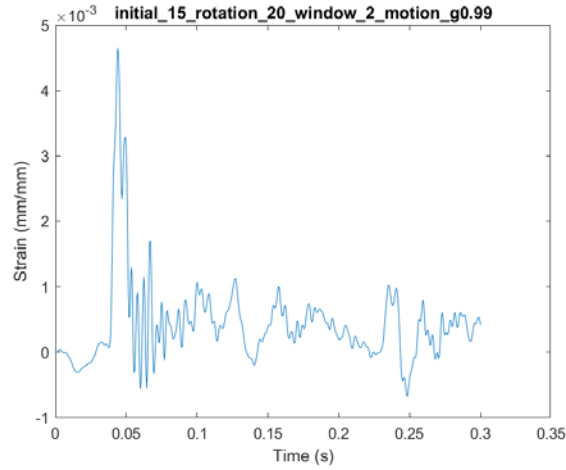
Figure B.8.   Strain Time History in Element with Peak Strain in the 20° (End Drop) Orientation
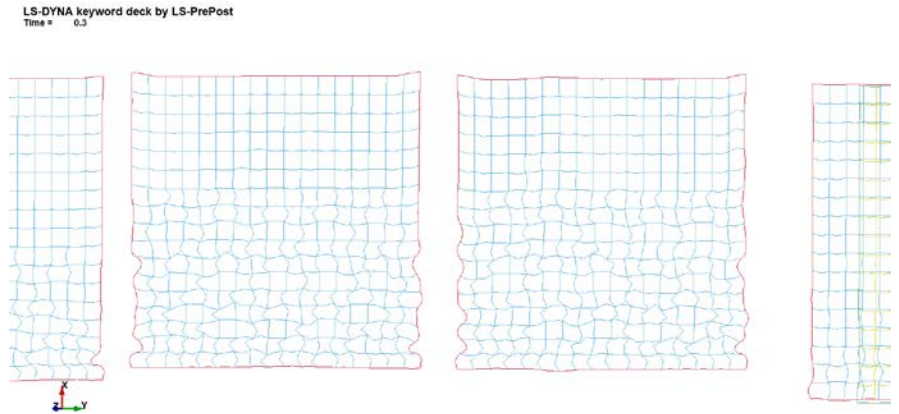
Figure B.9. Deformed Shape of Spacer Grids Post-impact in the 20° (End Drop) Orientation

LS-DYNA keyword deck by LS-PrePost
Time =   0.081
Contours of Axial Strain
beam integration pt#9
 min=-0.00442998, at elem# 49299
 max=0.00538324, at elem# 65779

Axial Strain
5.383e-03
4.402e-03
3.421e-03
2.439e-03
1.458e-03
4.766e-04
-5.047e-04
-1.486e-03
-2.467e-03
-3.449e-03
-4.430e-03
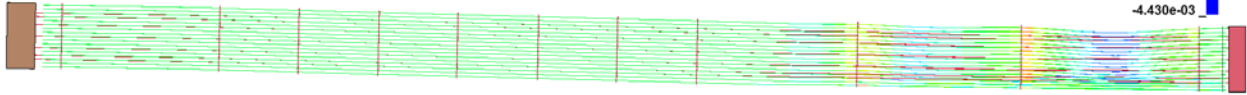
Figure B.10.   Contours of Cladding Strain, at Time of Peak Strain in the 40° (End Drop) Orientation
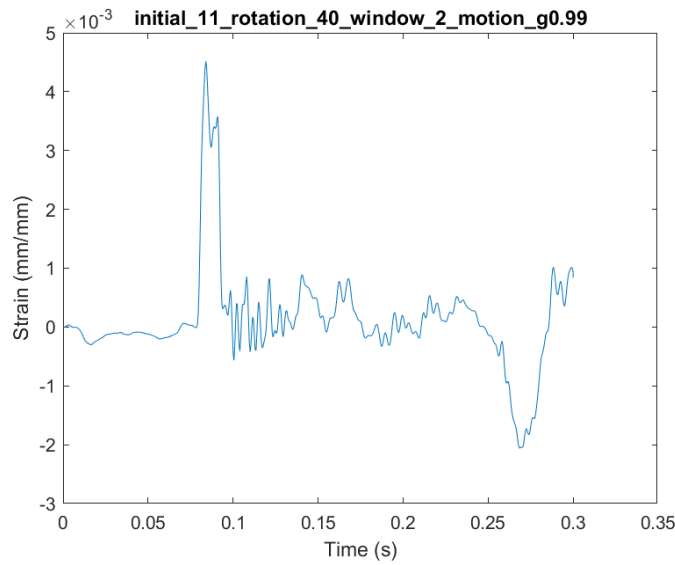
Figure B.11.   Strain Time History in Element with Peak Strain in the 40° (End Drop) Orientation
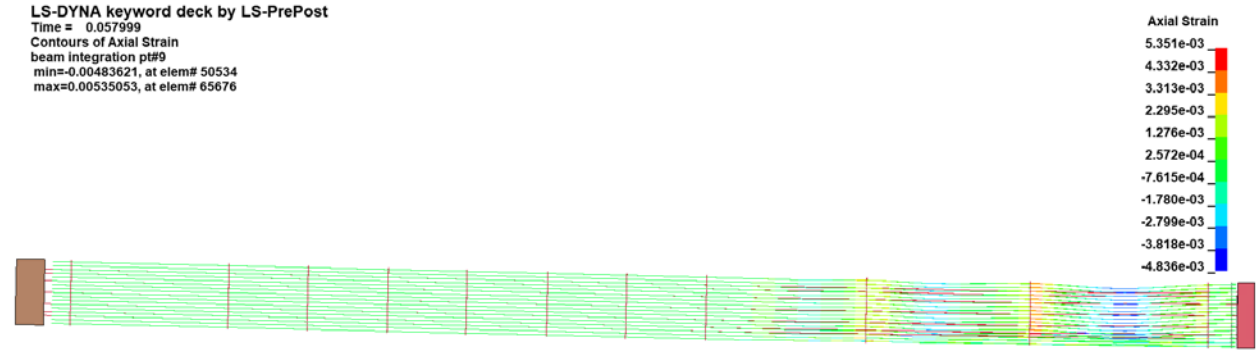
Figure B.12.   Contours of Cladding Strain, at Time of Peak Strain in the 60° (End Drop) Orientation
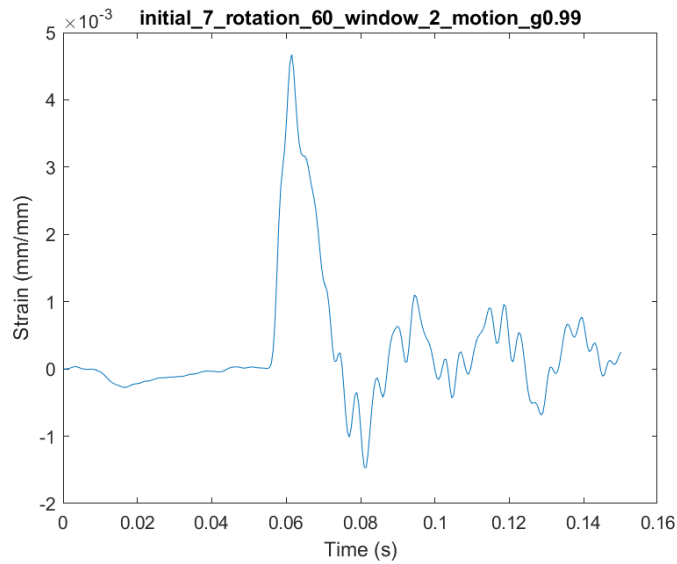
Figure B.13.   Strain Time History in Element with Peak Strain in the 60° (End Drop) Orientation

LS-DYNA keyword deck by LS-PrePost
Time = 0.0315
Contours of Axial Strain
beam integration pt#9
 min=-0.00336454, at elem# 68836
 max=0.00404958, at elem# 65499

Axial Strain
4.050e-03
3.308e-03
2.567e-03
1.825e-03
1.084e-03
3.425e-04
-3.989e-04
-1.140e-03
-1.882e-03
-2.623e-03
-3.365e-03
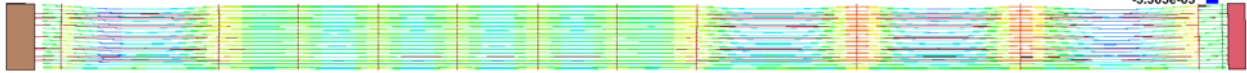
Figure B.14.   Contours of Cladding Strain, at Time of Peak Strain in the 90° (End Drop) Orientation
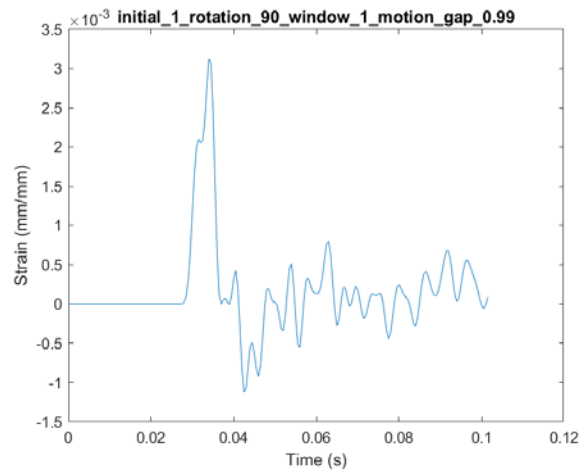
Figure B.15.   Strain Time History in Element with Peak Strain in the 90° (End Drop) Orientation

LS-DYNA keyword deck by LS-PrePost
Time = 0.10149
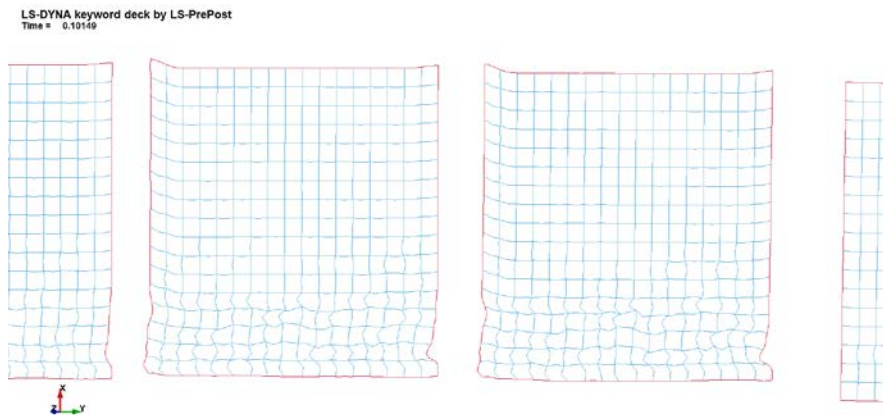
Figure B.16.   Deformed Shape of Spacer Grids Post-impact in the 90° (End Drop) Orientation

B-3.2   *Windowed Analysis Check*

This section presents additional details on the windowed analysis check discussed in Section 5.1.2.2. Figure B.17 shows the time history in the element with maximum strain during the initial impact in the 60° orientation, with a 1% lateral gap. Figures B.18 and B.19 show strain contour plots and maximum strain time history, with a 99% lateral gap.
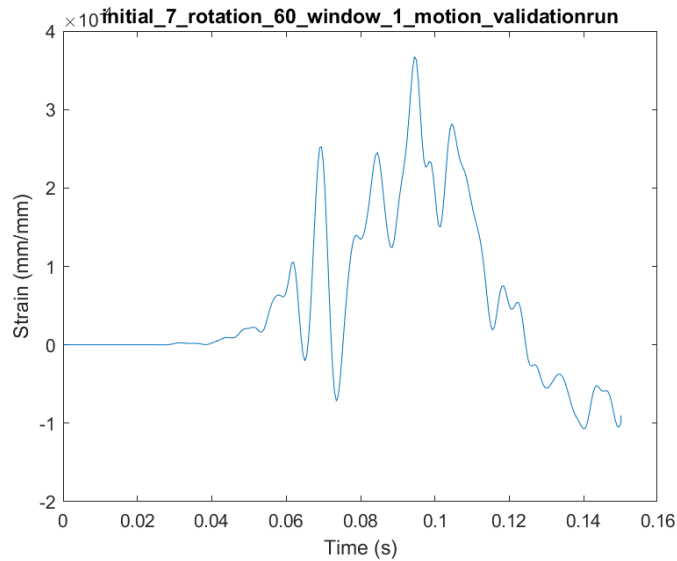
Figure B.17.   Strain Time History in Element with Peak Strain, 60° Orientation, Initial Impact, 1% Lateral Gap
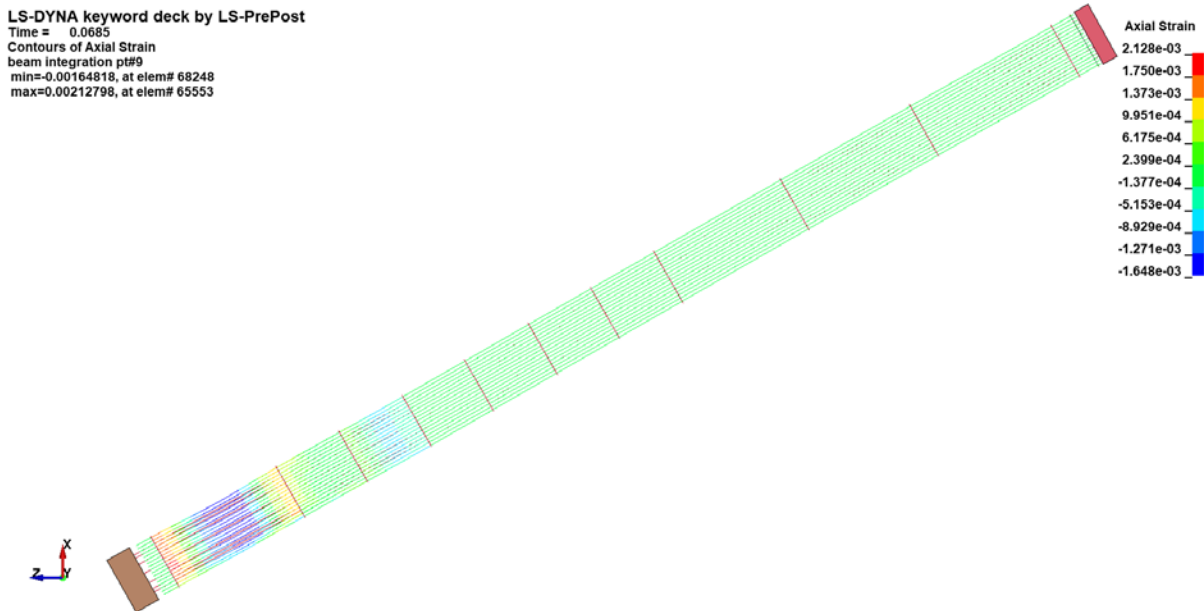
Figure B.18.   Contours of Cladding Strain, at Time of Peak Strain, 60° Orientation, Initial Impact, 99% Lateral Gap
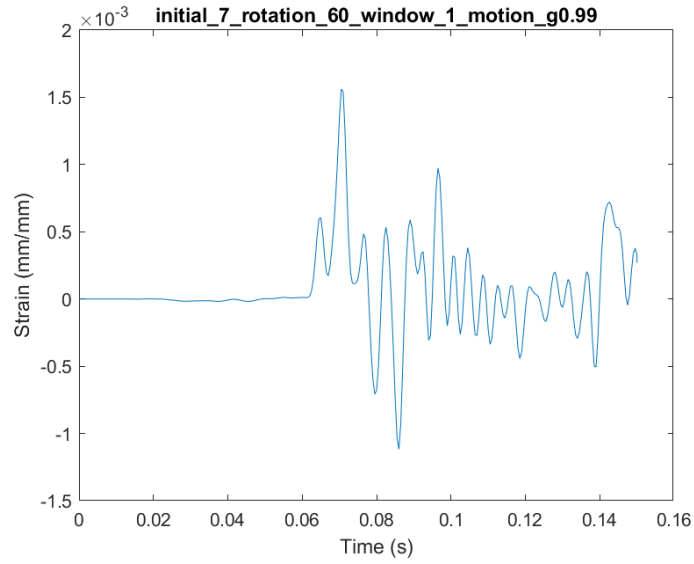
Figure B.19. Strain Time History in Element with Peak Strain, 60° Orientation, Initial Impact, 99% Lateral Gap

B-3.3   *Basket-fuel Gap Sensitivity Study*

This section presents additional details on the basket-fuel gap sensitivity study discussed in Section 5.1.2.3. Figures B.20 through B.27 show strain contours and time history of the element with maximum strain for various levels of basket-fuel gap.
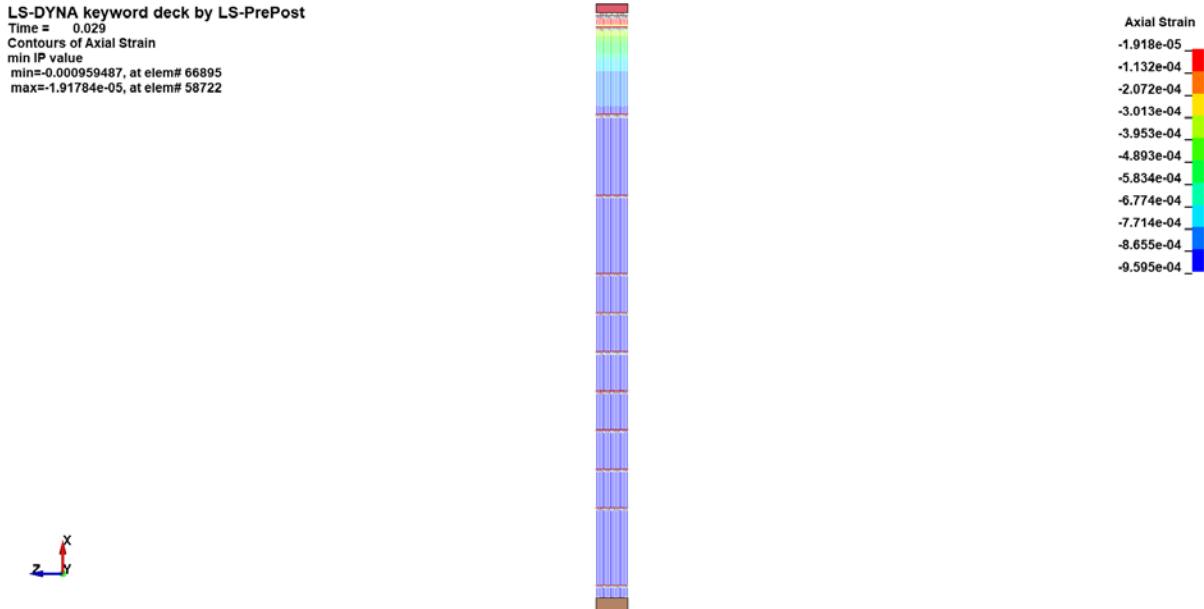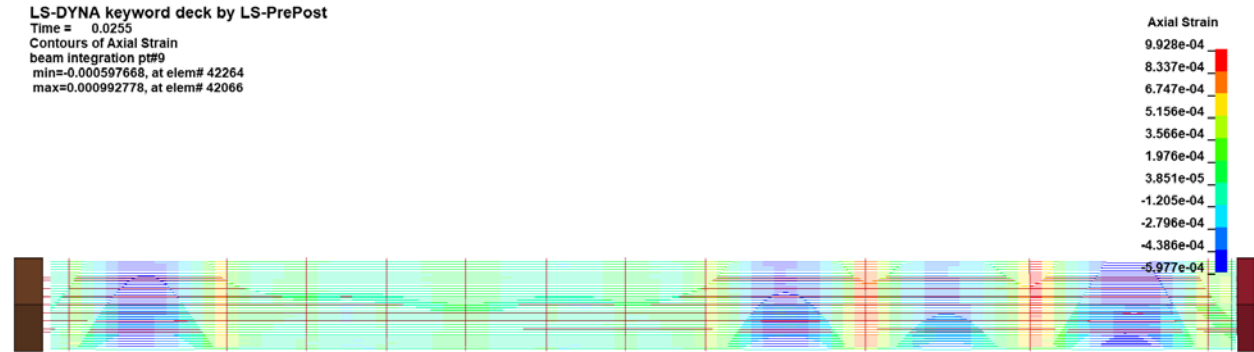

Figure B.20.   Contours of Cladding Strain, at Time of Peak Strain, 0° Orientation, 1% Longitudinal Gap
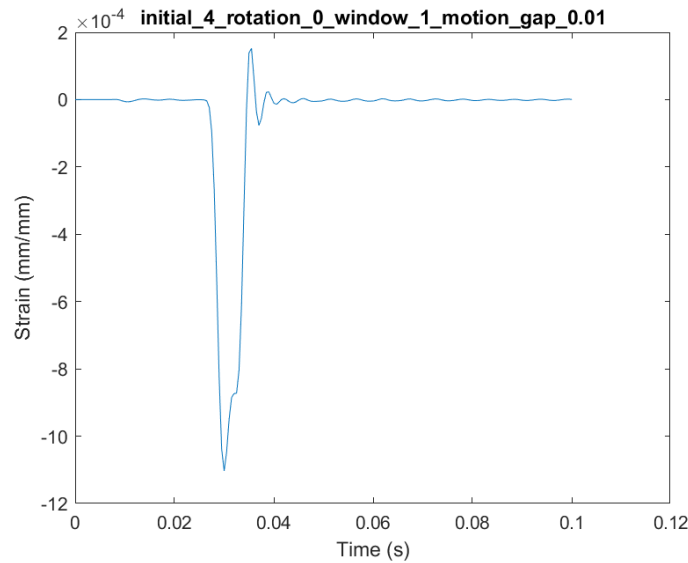
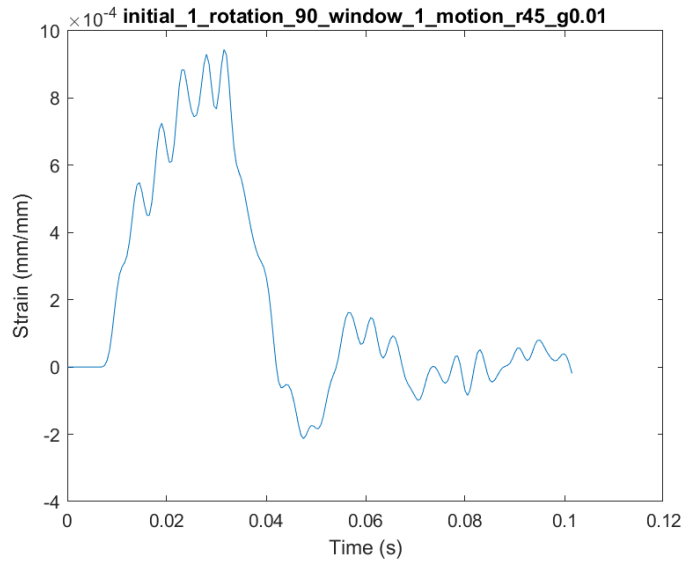**Figure B.21.   Strain Time History in Element with Peak Strain, 0° Orientation, 1% Longitudinal Gap**

LS-DYNA keyword deck by LS-PrePost
Time = 0.073499
Contours of Axial Strain
min IP value
 min=-0.000845185, at elem# 68873
 max=-4.99338e-07, at elem# 58722

Axial Strain
-4.993e-07
-8.497e-05
-1.694e-04
-2.539e-04
-3.384e-04
-4.228e-04
-5.073e-04
-5.918e-04
-6.762e-04
-7.607e-04
-8.452e-04
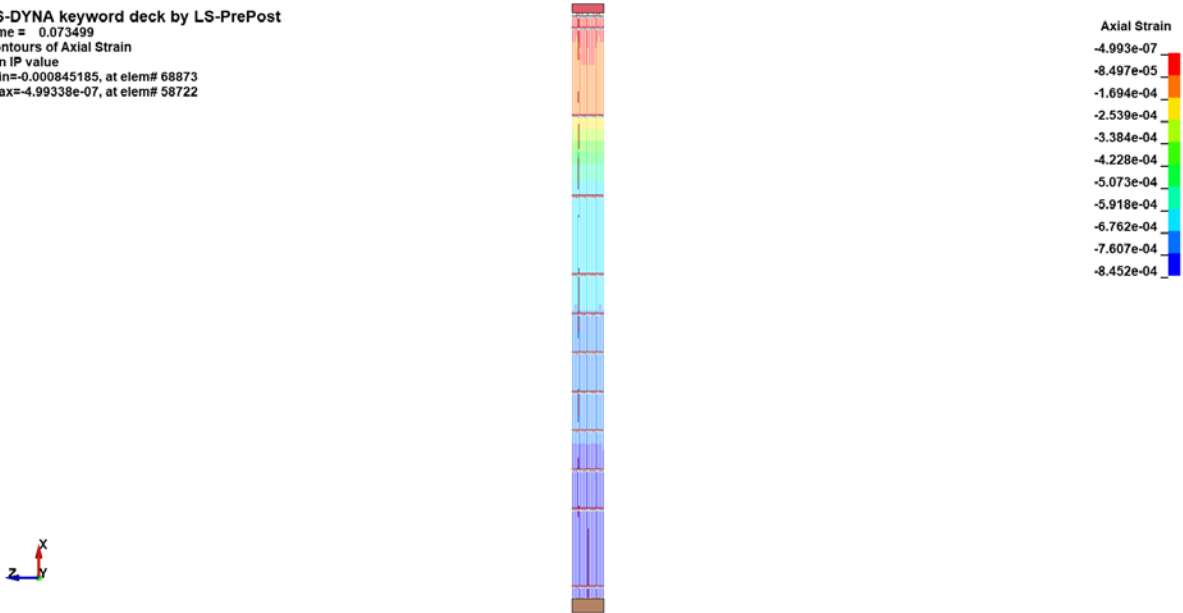
Figure B.22. Contours of Cladding Strain, at Time of Peak Strain, 0° Orientation, 50% Longitudinal Gap
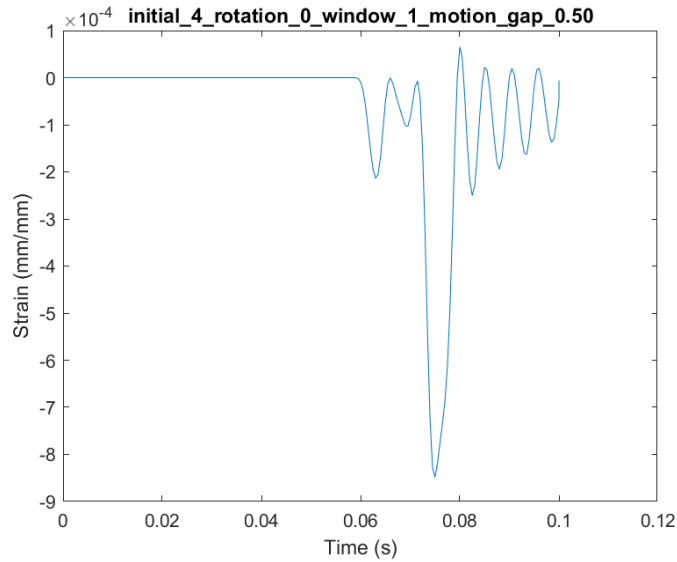
Figure B.23. Strain Time History in Element with Peak Strain, 0° Orientation, 50% Longitudinal Gap
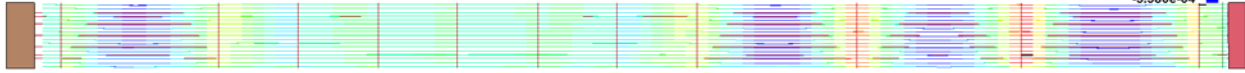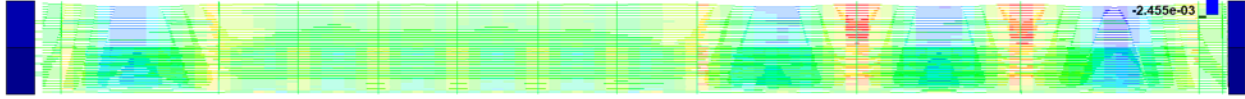
Figure B.24. Contours of Cladding Strain, at Time of Peak Strain, 90° Orientation, 1% Longitudinal Gap
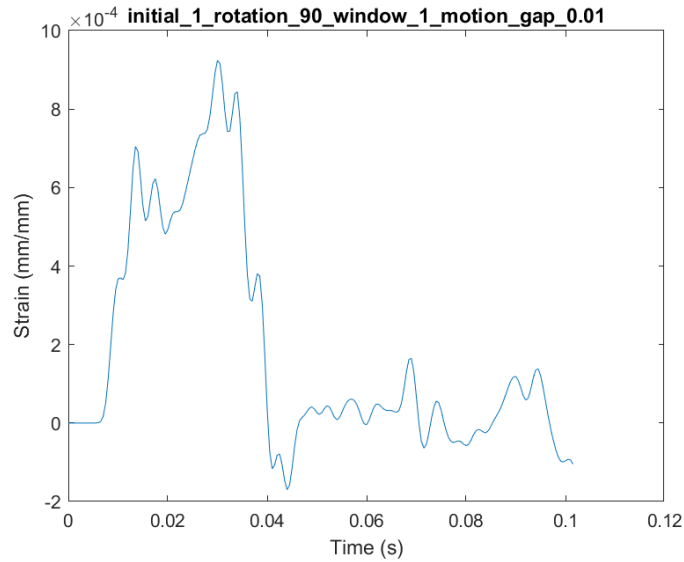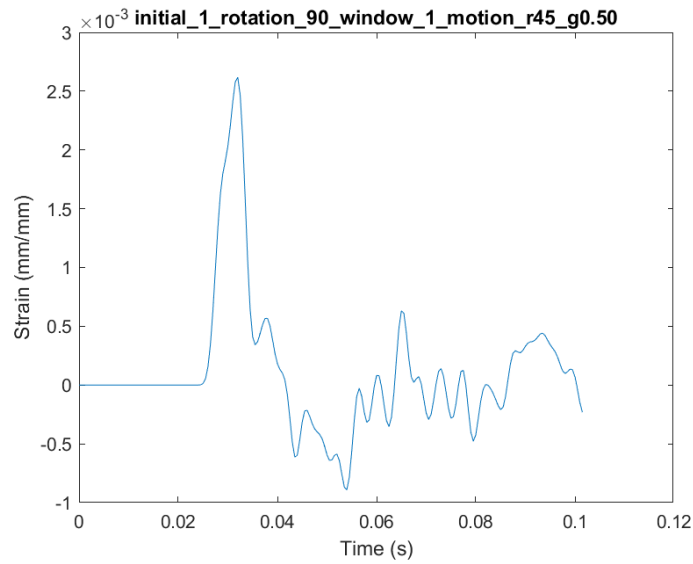

Figure B.25. Strain Time History in Element with Peak Strain, 90° Orientation, 1% Longitudinal Gap
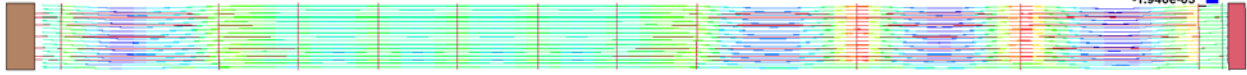
Figure B.26.   Contours of Cladding Strain, at Time of Peak Strain, 90° Orientation, 50% Longitudinal Gap
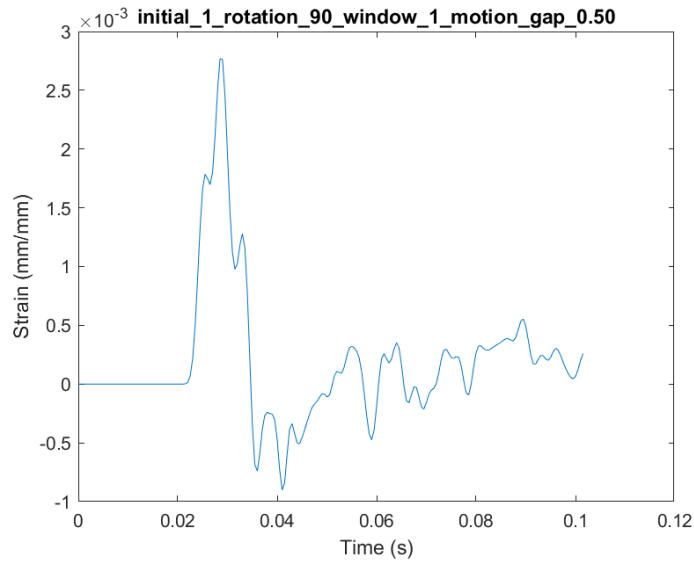
Figure B.27.   Strain Time History in Element with Peak Strain, 90° Orientation, 50% Longitudinal Gap

B-3.4   *Fuel Assembly Orientation Sensitivity Study*

This section presents additional details on the fuel assembly orientation sensitivity study discussed in Section 5.1.2.4. Figures B.28 through B.33 show contours of cladding strain and strain time history in the element with peak strain at various levels of lateral gap. Figure B.34 shows the extent of grid crushing in the case with maximum grid deformation.

Figure B.28.   Contours of Cladding Strain, at Time of Peak Strain, 90° Orientation, 1% Lateral Gap

Figure B.29.   Strain Time History in Element with Peak Strain, 90° Orientation, 1% Lateral Gap

Figure B.30. Contours of cladding strain, at time of peak strain, 90° Orientation, 50% Lateral Gap

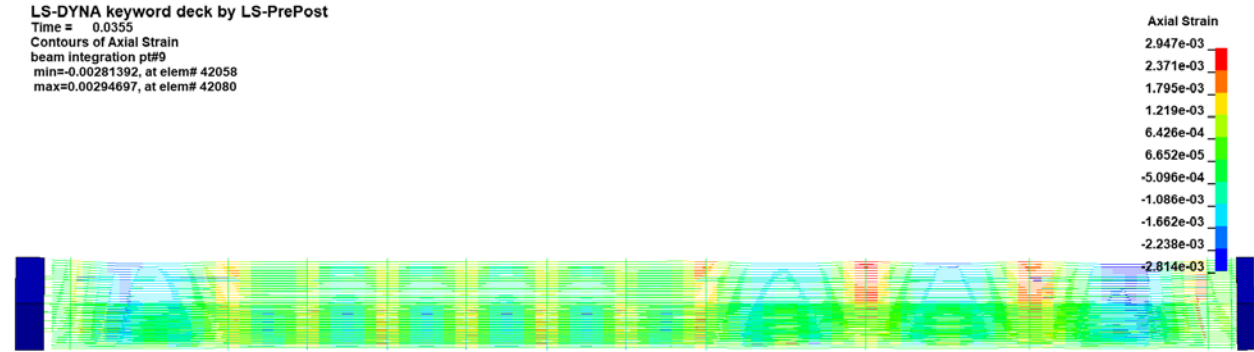**Figure B.31. Strain Time History in Element with Peak Strain, 90° Orientation, 50% Lateral Gap**

Figure B.32. Contours of Cladding Strain, at Time of Peak Strain, 90° Orientation, 99% Lateral Gap
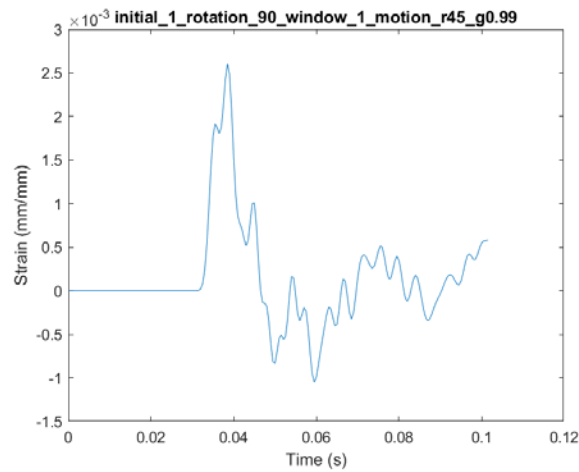

Figure B.33. Strain Time History in Element with Peak Strain, 90° Orientation, 99% Lateral Gap
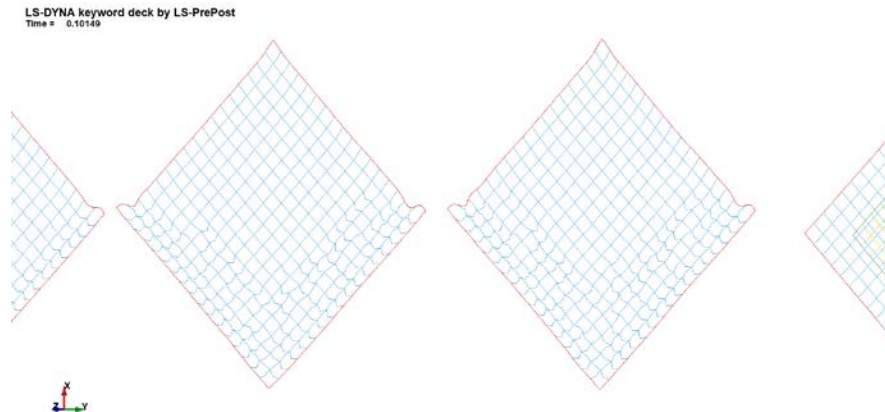

Figure B.34. Deformed Shape of Spacer Grids Post-impact, 90° Orientation, 99% Lateral Gap

B-3.5 *Effects of Cladding Temperature*

This section presents additional details on the cladding temperature sensitivity study discussed in Section 5.1.2.5. Figures B.34 and B.35 show contours of cladding strain and strain time history in the element with peak strain at various levels of lateral gap.
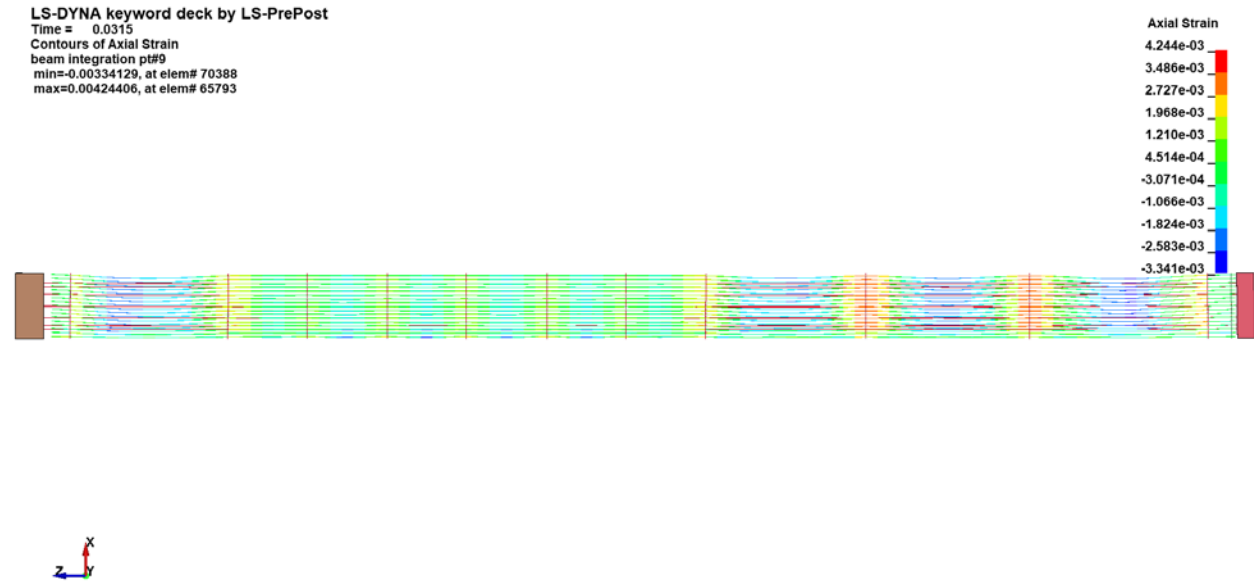

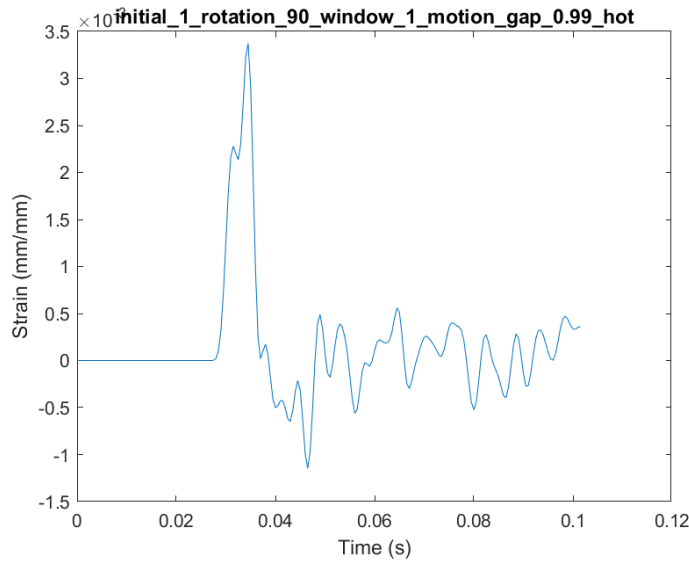**Figure B.35. Contours of Cladding Strain, at Time of Peak Strain, 90° Orientation, 200°C**

Figure B.36. Strain Time History in Element with Peak Strain, 90° Orientation, 200°C

B-4   References

Klymyshyn, N.A., Ivanusa, P., Kadooka, K., Spitz, C., Jensen, P.J., Ross, S.B., Hanson, B.D., Garcia, D., Smith, J., Lewis, S. "Modeling and Analysis of the ENSA/DOE Multimodal Transportation Campaign." PNNL-28088, Pacific Northwest National Laboratory, Richland WA, 2018.

Klymyshyn, N.A., Jensen, P.J., Sanborn, S., Hanson, B. "Fuel Assembly Shaker and Truck Test Simulation," PNNL-23688, Pacific Northwest National Laboratory, Richland WA, 2014.

This page is intentionally left blank.

APPENDIX C

CLADDING CONTACT STRESS ANALYSIS IN 30 CM DROP EVENTS

The contact stresses due to the impact of fuel cladding during 30 cm drop events is evaluated in this appendix. Under certain drop conditions, it was found that contact occurs between adjacent fuel rods and between the fuel rods and the basket. Reaction forces due to rod contact were approximated and extracted from a selection of drop conditions simulated using LS-DYNA in Sections 4 and 5 of this work. This appendix discusses the calculation of the contact stresses within the cladding due to these contact forces. The contact pressure and cladding stresses were approximated using analytical methods of Hertzian contact theory (Barber 2018) and a representative finite element analysis (FEA) model..

C-1   Model Development

Contact pressure exerted on the fuel cladding due to rod-to-rod impact and rod-to-basket impact can be approximated using analytical solutions from Hertzian contact theory. However, Hertzian contact assumes that the elastic materials in each body of contact are homogeneous. The cladding rods make up a heterogeneous system that includes the cladding tube material and the nuclear fuel material. To determine whether the heterogeneous nature of the fuel rods had an impact on contact pressure, a representative finite element model was generated for comparison to the analytical solution. The FEA model assumes that both materials (fuel cladding and fuel pellets) were perfectly bonded, and only the contact pressure at the cladding interface was noted.

C-1.1   *Analytical Solution*

At the time of impact, the contact geometry between rod-to-rod impact and rod-to-basket impact is elliptical. The geometry in both scenarios can be represented by the maximum and minimum radii of the curvature of each body. Thus, the analytical solution of elliptical Hertzian contact between elastic bodies can be used to approximate the contact pressure. The form of this solution was provided via Roark's Handbook (Young and Budynas 2001) and is as follows.

For the case of elliptical contact, both bodies are represented by minimum and maximum radii of curvature R_1 and R_1' for body one, and R_2 and R_2' for body two, in which the principal curvatures respective to each body are perpendicular. For convex shapes the radii are positive, and for concave the radii are negative. The contact modulus C_E is defined as:

$$C_E = \frac{1 - v_1{}^2}{E_1} + \frac{1 - v_2{}^2}{E_2} \tag{C.1}$$

where v and E are the material specific Poisson's ratio and modulus of elasticity, respectively. Then,

$$\cos(\theta) = \frac{K_D}{1.5} \sqrt{\left(\frac{1}{R_1} - \frac{1}{R'_1}\right)^2 + \left(\frac{1}{R_2} - \frac{1}{R'_2}\right)^2 + 2\left(\frac{1}{R_1} - \frac{1}{R'_1}\right)\left(\frac{1}{R_2} - \frac{1}{R'_2}\right)\cos(2\emptyset)} \tag{C.2}$$

and,

$$K_D = \frac{1.5}{\frac{1}{R_1} + \frac{1}{R_2} + \frac{1}{R'_1} + \frac{1}{R'_2}}$$

(C.3)

where $\emptyset$ is the angle between the plane containing curvature $\frac{1}{R_1}$ and the plane containing curvature $\frac{1}{R_2}$. In the case presented in this report, the angle $\emptyset$ is assumed to be zero, and there is minimum skew angle between fuel rods. The value of $\cos(\theta)$ is then used to interpolate values of α and β (which are tabulated values in Roark's solution) for the following equations. For a total contact load P, the major semi-axis c, and minor semi-axis d are defined as:

$$c = \alpha \sqrt[3]{PK_D C_E}$$

(C.4)

$$d = \beta \sqrt[3]{PK_D C_E}$$

(C.5)

From above, the maximum contact pressure can be calculated as:

$$(\sigma_c)_{max} = \frac{1.5P}{\pi c d}$$

(C.6)

C-1.2 *FEA Model*

To determine the effect of the fuel pellet substrate in comparison to the analytical solution, a finite element model was generated using the ANSYS Parametric Design Language. The model geometry assumes that both rods are equally convex during contact, and the maximum radius of the curvature (20.2929 m) was calculated from a representative 500 mm span length and 12.6 mm fuel pin pitch.

The model uses quarter symmetry in which the nodes along the XY-plane were constrained in the Z direction, the nodes along the YZ-plane were constrained in the X direction, and the nodes at the bottom of the lower body were constrained in the Y direction. The length of the model in the positive X direction for each load case was chosen as the corresponding major semi-axis length from the analytical solution. In accordance with Hertzian contact theory, the contact algorithm was standard frictionless contact, and the entire load was applied to the top of the upper body. As can be seen in Figure C.1, an exceptionally fine mesh was implemented to capture the contact pressure of the highly elliptical contact. Two scenarios were evaluated: one with the rods being homogeneous through the thickness with cladding material as in the analytical solution, and the other where the fuel material was modeled within the cladding. It is important to note that this analysis does not account for contact between the fuel and the cladding, only the contact at the outer surface of the cladding. Thus, the FEA model assumes that the fuel and cladding are fully bonded together. To compare the FEA results with the analytical solution, both methods were evaluated at applied loads of 20, 40, 60, 80, 100, 1000, and 5000 N.
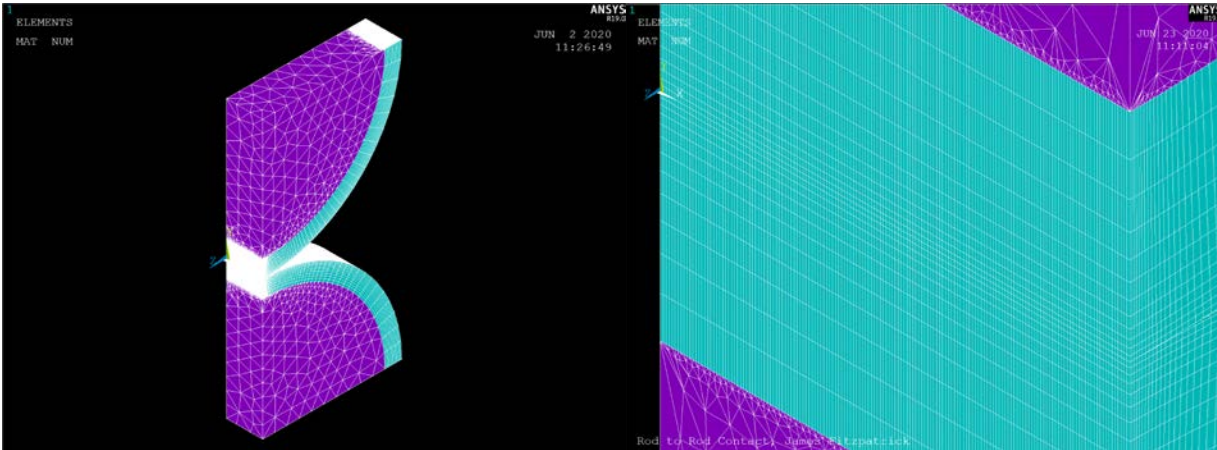
Figure C.1. **Finite Element Model of Rod-to-Rod Contact with Cladding and Fuel Materials (left) and Magnified View of Mesh Density at the Contact Interface (right). In purple: fuel material. In green: cladding material.**

C-1.3 *Validation of Analytical Solution and FEA Model*

It was first necessary to compare the analytical solution to the FEA result, under the assumption of a homogeneous body. Before the fuel substrate and its effects could be modeled, the homogeneous FEA and analytical solution had to match. Initially, it was observed that the FEA results underapproximated the contact pressure in comparison with the analytical solution. To adjust for this, it was possible to apply a constant scale factor of 0.65 to the contact length in all load cases in the FEA model, after which the FEA and analytical solution became nearly identical (see Figure C.2). Of the seven load cases that were observed, a maximum of 1.27% difference was observed between the homogeneous cladding FEA and analytical solution.
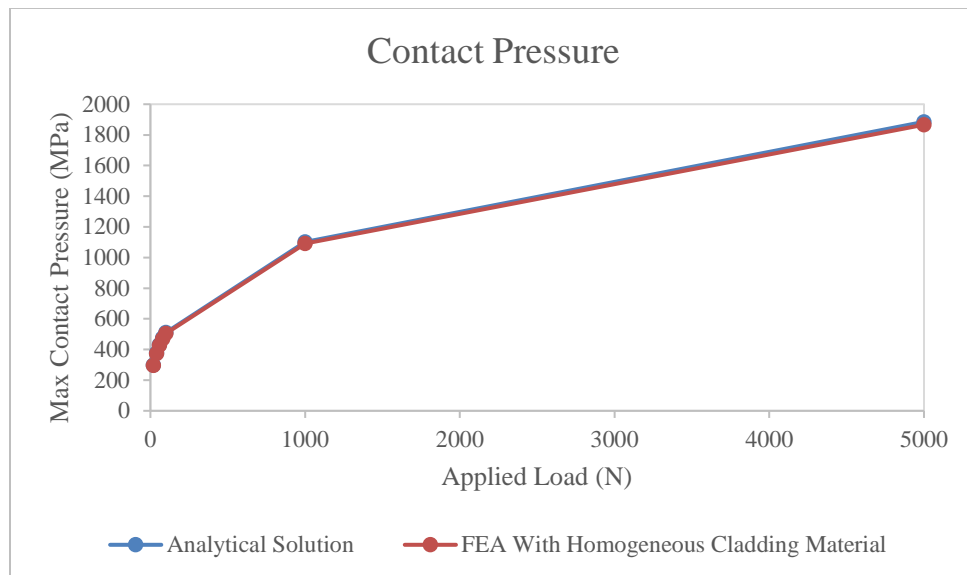

Figure C.2. **Maximum Contact Pressure of Analytical Solution and FEA Model**

When evaluating the contact pressure in relation to the stress components of interest (Figure C.3), it was found that all components exhibited an approximately 1:1 ratio with respect to the maximum contact pressure, with a maximum difference of 5.75% occurring in circumferential compression at the 20 N load

case. As the load increases, the discrepancy decreases. As a conservative approach, the contact pressure can be used for these components. With good agreement between the homogeneous FEA results and the analytical solution, it next was necessary to model the fuel substrate to observe its effects.

Similarly, in comparing these stress components between the homogeneous cladding material model and fuel substrate model, it was observed that the fuel substrate had little effect on the stress components (see Figure C.4). However, the model with the fuel substrate featured lower values in circumferential stress. Thus, the analytical solution could be used as a conservative approach to determine the contact pressure, radial stress, and circumferential stress induced in the cladding, and FEA was not necessary. The individual stress components during rod impact may be considered in future studies of the complete stress state within the cladding during drop events.
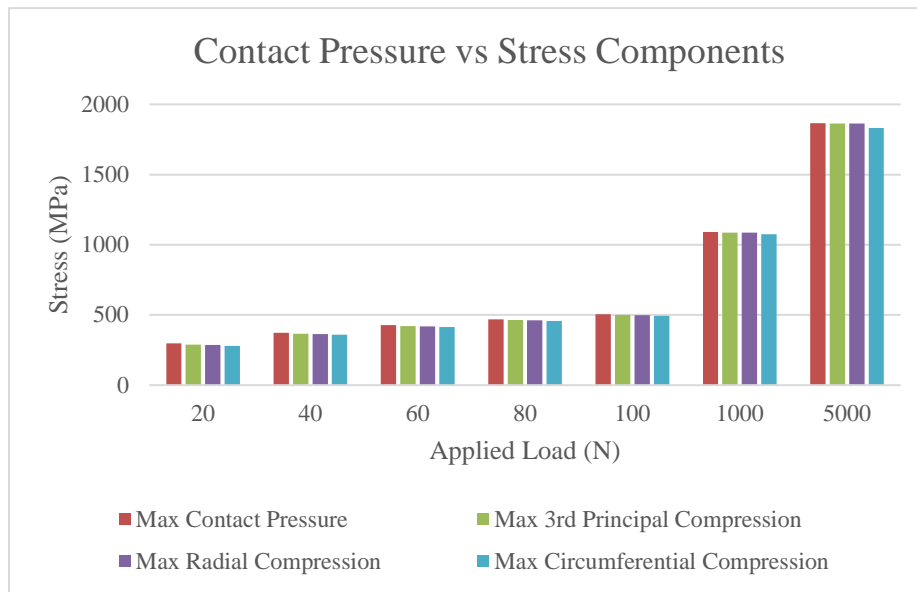
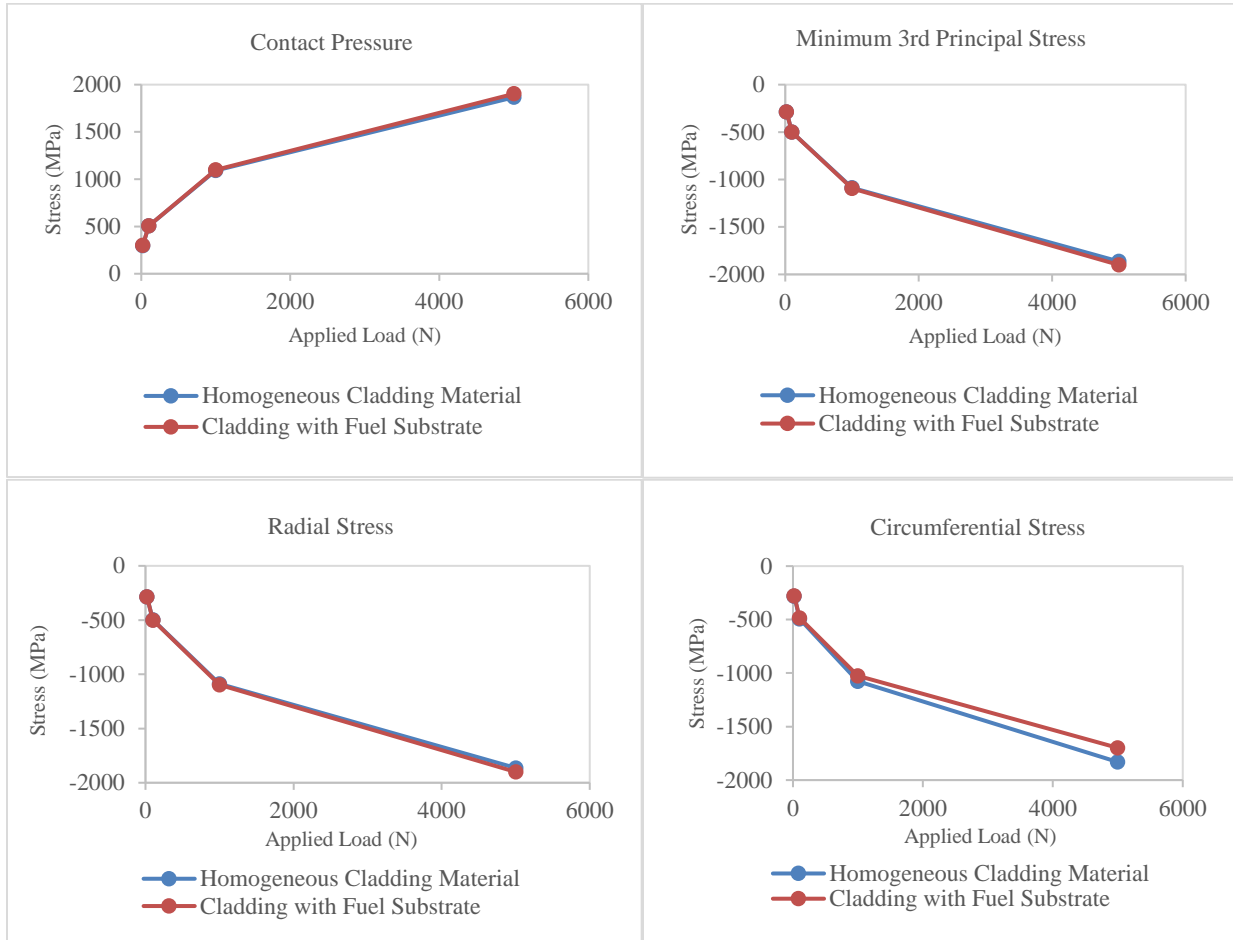**Figure C.3.   Contact Pressure Comparison with Component Stresses of Interest**

Figure C.4. Stress Component Comparison between Homogeneous FEA and Heterogeneous FEA

C-2   Model Applications

Rod contact forces within a fuel assembly during a 30 cm drop were extracted from the crushable grid fuel assembly model developed in LS-DYNA and described in Section 4.2. Approximate contact forces were extracted from two drop scenarios: the 30 cm assembly drop conducted at SNL modeled in Section 4.2 and the generic 60° drop modeled in Section 5.1, which was the limiting case for cladding strain evaluated in this work.

All contact force data were filtered by a low-pass filter with a 300 Hz cutoff frequency, consistent with filtering methods used throughout this work. This work considered only the contact forces lateral to the fuel, in the direction of the drop. Note that the naming scheme for the rods and spans (e.g., Span A, Span C, etc.) in this report was chosen for convenience and differs from the naming scheme used by SNF.

C-2.1   *SNL 30cm Drop*

Figure C.5 illustrates the contact interactions for the fuel rod with maximum contact forces in rod-to-basket contact. Figure C.6 illustrates the maximum contact force due to initial impact (at 0.0177 seconds in the model time history), which occurred in a fuel rod (Rod A) in the bottom row, where contact with the basket first occurs during impact. It is important to note the method that the LS-DYNA model uses to report contact forces in the rod. At each time step, the model sums all contact forces for the entire rod, which can include any rod interactions with other rods, the basket, and the grids. Thus, visual inspection was necessary to confirm the time of maximum contact force. It was determined that at the time of

maximum contact force, Rod A was in contact with the basket in two spans (Span A and Span C). To estimate of the contact force in each span, it was assumed that all the force was due to the rod-to-basket contact (no contribution from rod-to-rod or rod-to-grid contact), and that the force was divided equally among the two interactions.
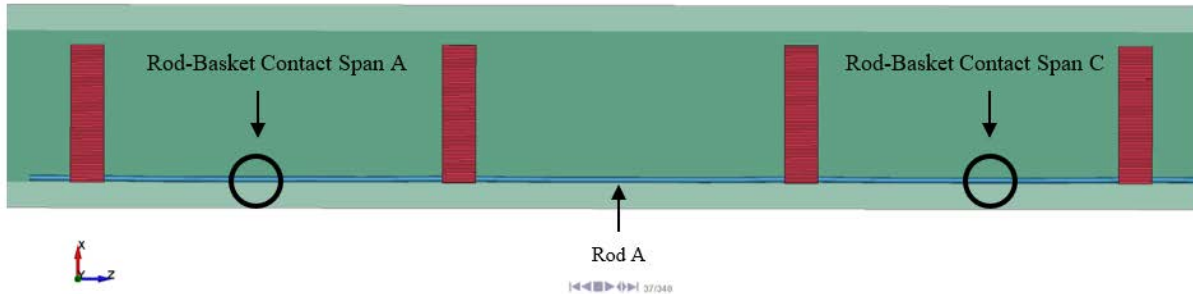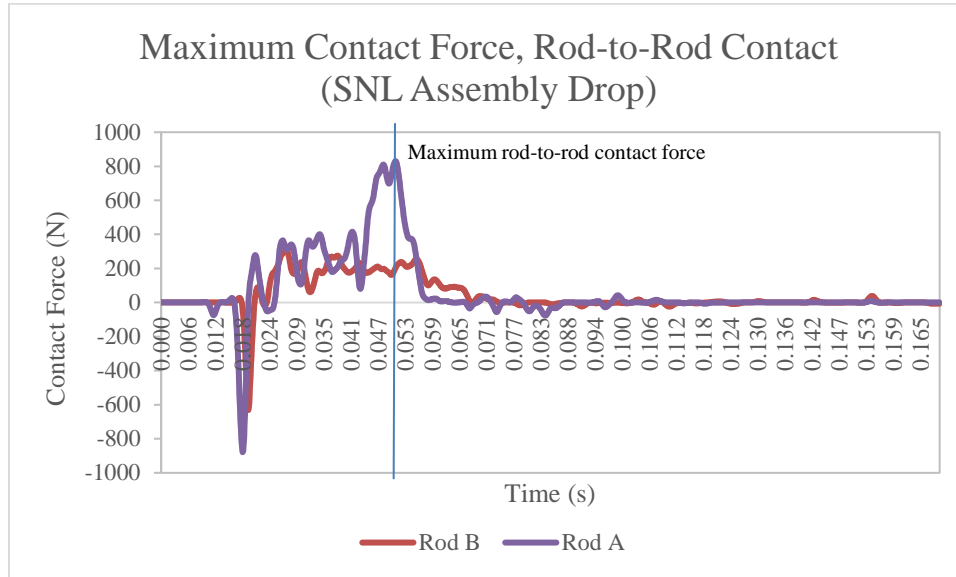

Figure C.5. Snapshot of Model at Time of Peak Rod-to-Basket Contact Force in the SNL Assembly Drop Model
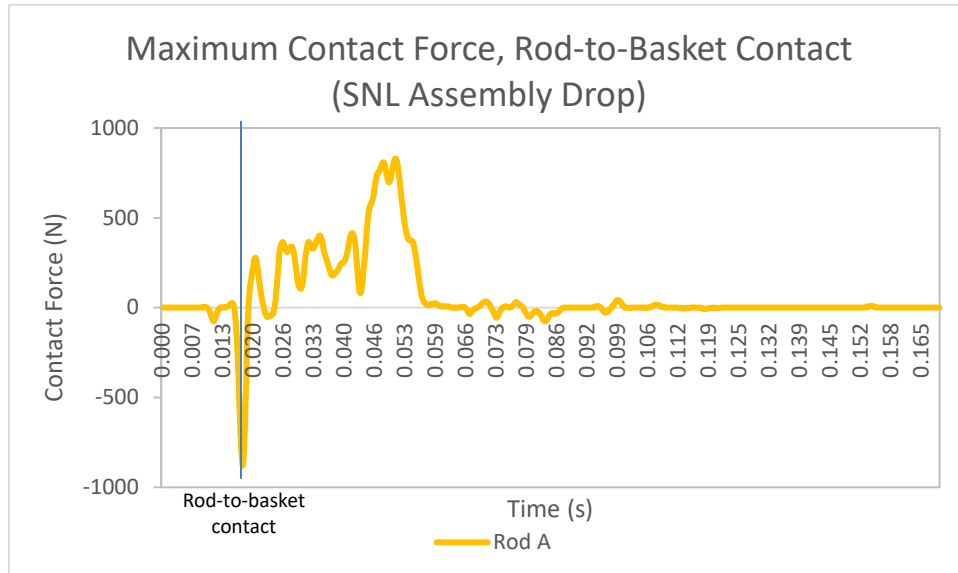

Figure C.6. Contact Force in Rod with Peak Rod-to-Basket Contact in the SNL Assembly Drop Model

At approximately 0.051 seconds, Rod A contacts the rod above it, Rod B, resulting in the maximum rod-to-rod contact force (see Figure C.7). Upon visual inspection, this was a single point of rod-to-rod contact (see Figure C.8). However, Figure C.7 illustrates the discrepancy caused due to the LS-DYNA summation of contacts along the entire rod. Note that the contact force at Rod B is far different than the contact force in Rod A at the time of contact pictured in Figure C.8. This is due to the LS-DYNA model summing the reactions from additional interactions along the rod, which produces a total contact force. Thus, as with the rod-to-basket case, a conservative assumption was made that all the total contact force was concentrated within the single rod-to-rod contact, and the maximum value was used. The actual forces in the contact regions may be different and lower than what is recorded. Therefore, the values used in this study are a conservative approximation, and further investigation with additional discretization of the contact force output is needed in future studies.

Figure C.7. **Contact Force in the Two Rods with the Peak Rod-to-Rod Contact in the SNL Assembly Drop Model**
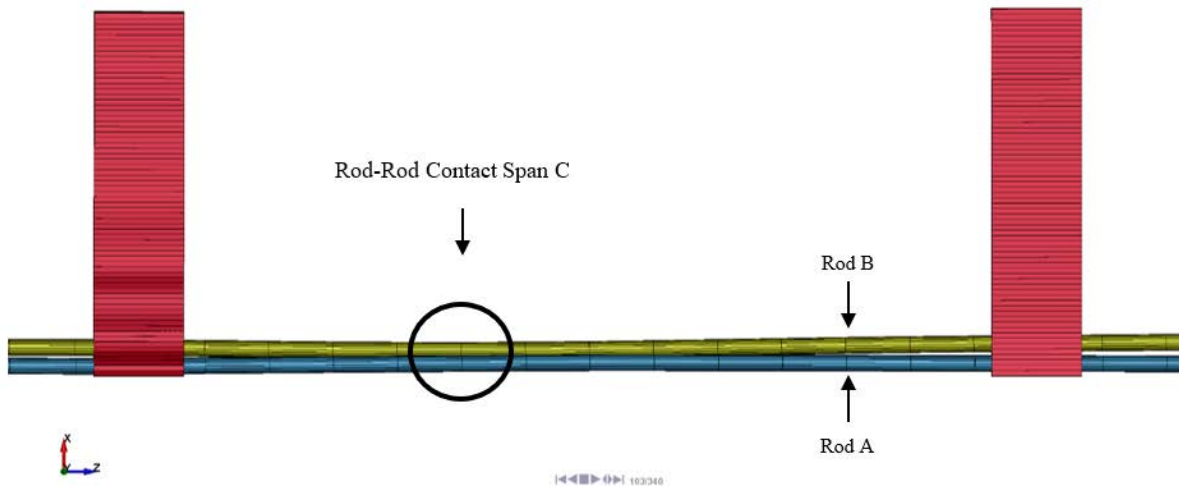
Figure C.8. **Snapshot of Model at Time of Peak Rod-to-Rod Contact in the SNL Assembly Drop Model**

Using the Hertzian contact analytical solution, the maximum contact pressures were calculated. The curvatures of each rod were estimated from nodal vertical displacement with respect to the adjacent grid at the time of contact. Because only the component normal to the cask impact direction were being considered, these curvatures were calculated with respect to this direction also. It is important to note that in the rod-to-rod contact of this case (SNL drop), the conservative values of curvature were calculated due to the rods sliding behind one another during contact, due to the shear-racking deformation behavior of grid buckling during impact. The basket material properties were assumed to be those of A356 aluminum because aluminum is the main constituent material of the aluminum-boron metal matrix composite basket material. As seen in Table C.1, the maximum contact pressure occurs during the rod-to-rod contact interaction. This substantial increase in pressure is believed to be due to material properties, relative curvatures, as well as the relative velocities between the two rods during contact.

Table C.1. Approximate Contact Pressure in the SNL Drop

Contact Interaction	Contact Force (N)	Maximum Contact Pressure (MPa)
Maximum Rod-to-rod (Span C)	831	1035.5
Maximum Rod-to-basket (Span A)	439.5	511.57
Maximum Rod-to-basket (Span C)	439.5	511.42

Of additional interest is the interaction of contact stress and the cladding circumferential (hoop) stress due to internal rod pressure. As a conservative approach, the circumferential compressive stress due to contact was taken as being equal to the contact pressure, as discussed in Section C-1.3. The total maximum circumferential stress was calculated for static circumferential stress values reported at a lower bound burnup (47.5 MPa) and upper bound burnup (110 MPa) (Kim et al. 2017) and are listed in Table C.2 and Table C.3, respectively. Note that the sign of the contact stress is opposite that of the static circumferential stress because of internal pressure. Analysis of the total cladding stress state and the interaction of the primary and secondary stresses is a possible subject of future analysis.

Table C.2. Resultant Circumferential Stress at 30 GWd/tU Burnup in the SNL Drop

Contact Interaction	Rod Circumferential Stress, 30 GWd/tU (MPa)	Contact Circumferential Stress (MPa)	Total Circumferential Stress, 30 GWd/tU (MPa)
Maximum rod-to-rod (Span C)	47.5 (Tensile)	1035.5 (Compression)	988 (Compression)
Maximum rod-to-basket (Span A)	47.5 (Tensile)	511.57 (Compression)	464.07 (Compression)
Maximum rod-to-basket (Span C)	47.5 (Tensile)	511.42 (Compression)	463.92 (Compression)

Table C.3. Resultant Circumferential Stress at 60 GWd/tU Burnup in the SNL Drop

Contact Interaction	Rod Circumferential Stress, 60 GWd/tU (MPa)	Contact Circumferential Stress (MPa)	Total Circumferential Stress, 60 GWd/tU (MPa)
Maximum rod-to-rod (Span C)	110 (Tensile)	1035.5 (Compression)	925.5 (Compression)
Maximum rod-to-basket (Span A)	110 (Tensile)	511.57 (Compression	401.57 (Compression)
Maximum Rod-to-basket (Span C)	110 (Tensile)	511.42 (Compression)	401.42 (Compression)

C-2.2 *Generic 60° Drop*

Further consideration was given to the generic 60° 30 cm drop orientation modeled in Section 5.1, which was the limiting configuration in terms of cladding strain. The contact forces due to rod-to-rod and rod-to-basket contact were obtained using the same assumptions as those use for the analysis of the SNL assembly drop in the previous section.

The drop event can be described as having initial contact at the corner nearest the ground, after which the rest of the cask rotates until it "slaps down" onto the ground (hereafter referred to as "slapdown"). The first maximum rod-to-rod contact force was recorded during the slapdown event (at 0.0553 seconds), and from visual inspection, Rods C and D were found to be in contact (see Figure C.9). In this case, the reactions in rods C and D were very comparable at the time of slapdown (see Figure C.10). As before, the contact reaction was taken to be the maximum between the two and assumed to be solely due to this interaction.
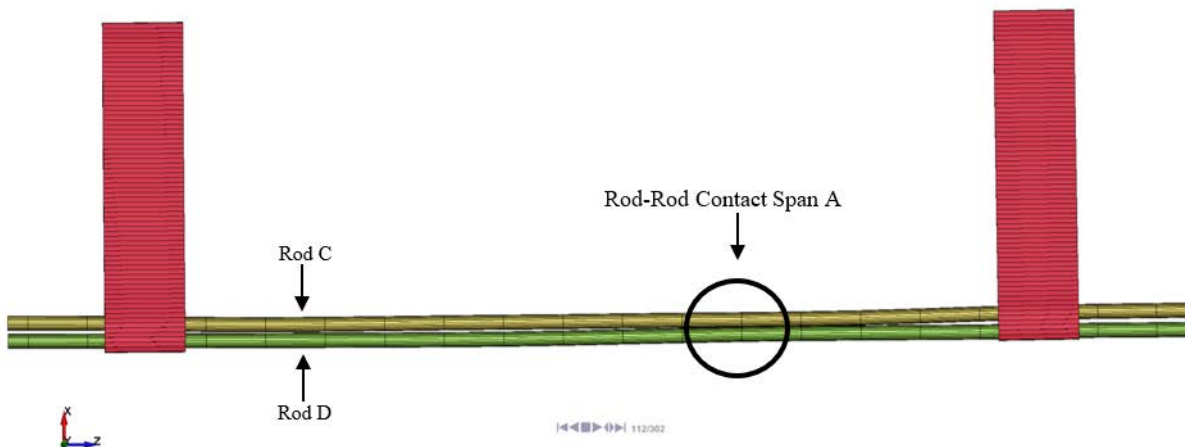

Figure C.9.   Snapshot of model at time of peak rod-to-rod contact in the generic 60° drop.
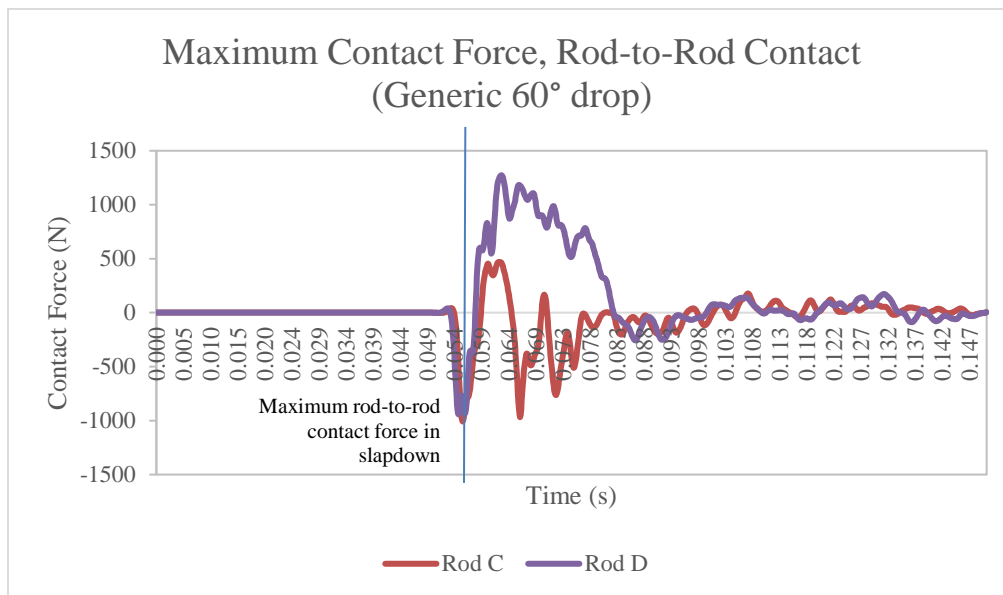

Figure C.10.   Contact Force in the Two Rods with Maximum Rod-to-Rod contact, in the Generic 60° Drop

Following the slapdown event, at 0.0701 seconds, an additional maximum contact force was found in Rod A, and from visual inspection, it was found that Rod A was in contact with the basket (see Figure C.11 and Figure C.12). As with the previous scenarios, this maximum was assumed to be solely due to this interaction.
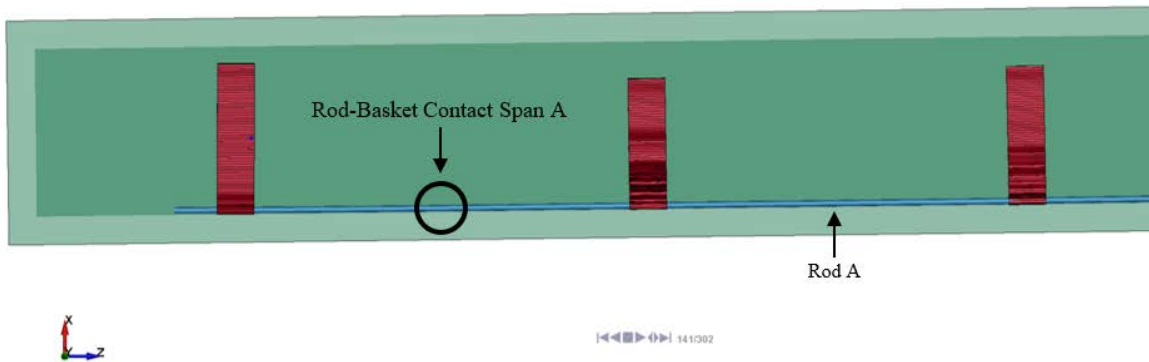
Figure C.11.   Snapshot of Model at Time of Peak Rod-to-Basket Contact in the Generic 60° Drop
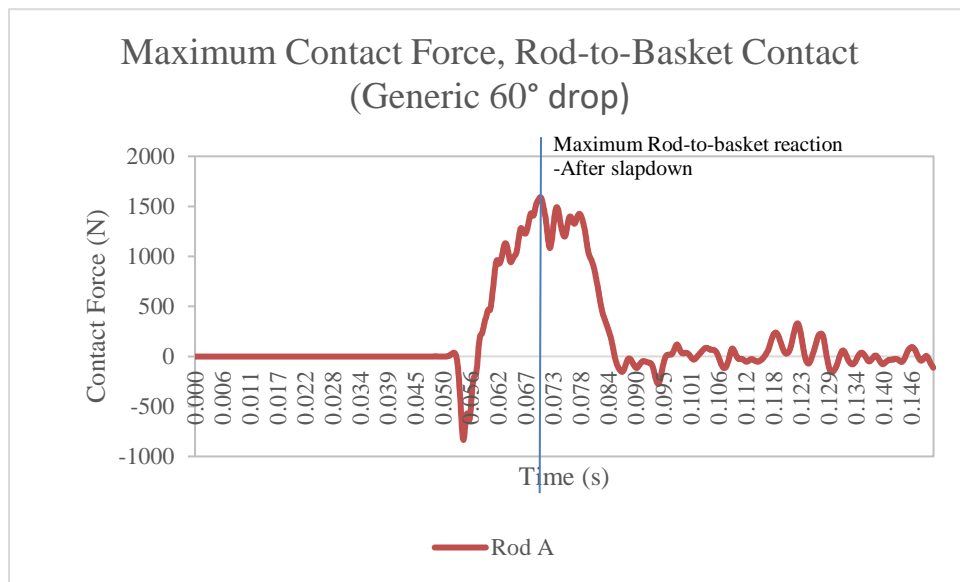

**Figure C.12. Contact Force in the Rod with Maximum Rod-to-Basket Contact, in the Generic 60°
Drop**

The estimated contact pressures in the 60° drop scenario were calculated using the same method as that used in the SNL drop case. The curvatures of each rod were estimated from nodal vertical displacement with respect to the adjacent grid at the time of contact. Table C.4 illustrates that the maximum contact pressure occurs during the rod-to-rod contact interaction at initial slapdown. Table C.5 and Table C.6 present the total circumferential stress accounting for static circumferential stresses due to internal rod pressure at two representative burnup values.

Table C.4. Approximate Contact Pressure – Generic 60° Drop

Contact Interaction	Reaction Force (N)	Maximum Contact Pressure (MPa)
Maximum Rod-to-rod (Span A)	1010	1107.1
Maximum Rod-to-basket (Span A)	1590	784.2

Table C.5.   Resultant Circumferential Stress at 30 GWd/tU Burnup, 60° Drop

Contact Interaction	Rod Circumferential Stress, 30 GWd/tU (MPa)	Contact Circumferential Stress (MPa)	Resultant Circumferential Stress, 30 GWd/tU (MPa)
Maximum Rod-to-rod (Span A)	47.5 (Tensile)	1107.1 (Compression)	1059.6 (Compression)
Maximum Rod-to-basket (Span A)	47.5 (Tensile)	784.2 (Compression)	736.7 (Compression)

Table C.6.   Resultant Circumferential Stress at 60 GWd/tU Burnup, 60° Drop

Contact Interaction	Rod Circumferential Stress at 60 GWd/tU (MPa)	Contact Circumferential Stress (MPa)	Resultant Circumferential Stress, 60 GWd/tU (MPa)
Maximum Rod-to-rod (Span A)	110 (Tensile)	1107.1 (Compression)	997.1 (Compression)
Maximum Rod-to-basket (Span A)	110 (Tensile)	784.2 (Compression)	674.2 (Compression)

C-2.3   *Discussion*

One potential concern is loss of cladding structural integrity due to contact stress during a drop event. A criterion for the onset of yield with respect to contact pressure is given by Barber (2018) and is predicted to be in the range of

$$1.6S_y < (\sigma_c)_{max} < 1.8S_y \tag{C.7}$$

where S_y is the yield stress of the material in uniaxial tension, and $(\sigma_c)_{max}$ is the maximum contact pressure. The onset of yield occurs locally, at a location y interior to the material surface, normal to contact and in the range of

$$0.45d < y < 0.8d \tag{C.8}$$

where d is the minor semi-axis of the elliptical contact. As the loading increases beyond that required to initiate local yielding, the plastic zone increases and approaches the material surface. The maximum contact pressures (excluding hoop stress) for the SNL 30 cm assembly drop and generic 60 degree drop models were compared to these relations in Figure C.13 and Figure C.14, respectively.

Note that these relationships predict local yielding, not gross yielding through the cladding thickness. Thus, the criterion used here is a conservative measure of cladding integrity. A more realistic limit for the cladding contact pressure may be evaluated in the future by using a FEA model similar to the one developed in this analysis, but incorporating material plasticity and increasing the load until plastic flow initiates.
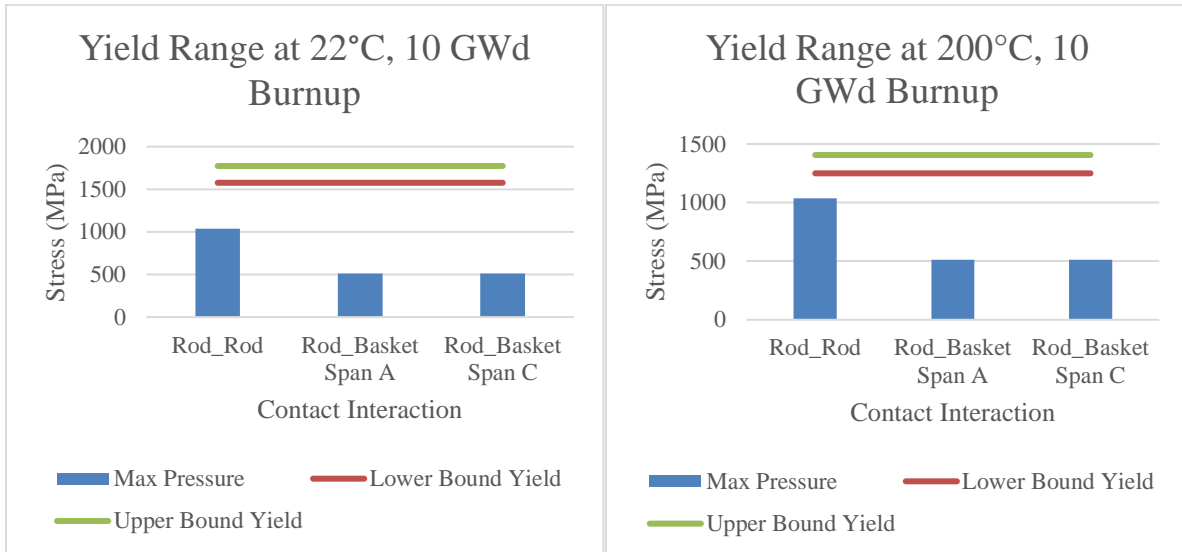
Figure C.13. **SNL Assembly Drop – Contact Pressure in Relation to Yield Point Range: 22°C, 10 GWd Burnup (left) and 200°C, 10 GWd Burnup (right)**
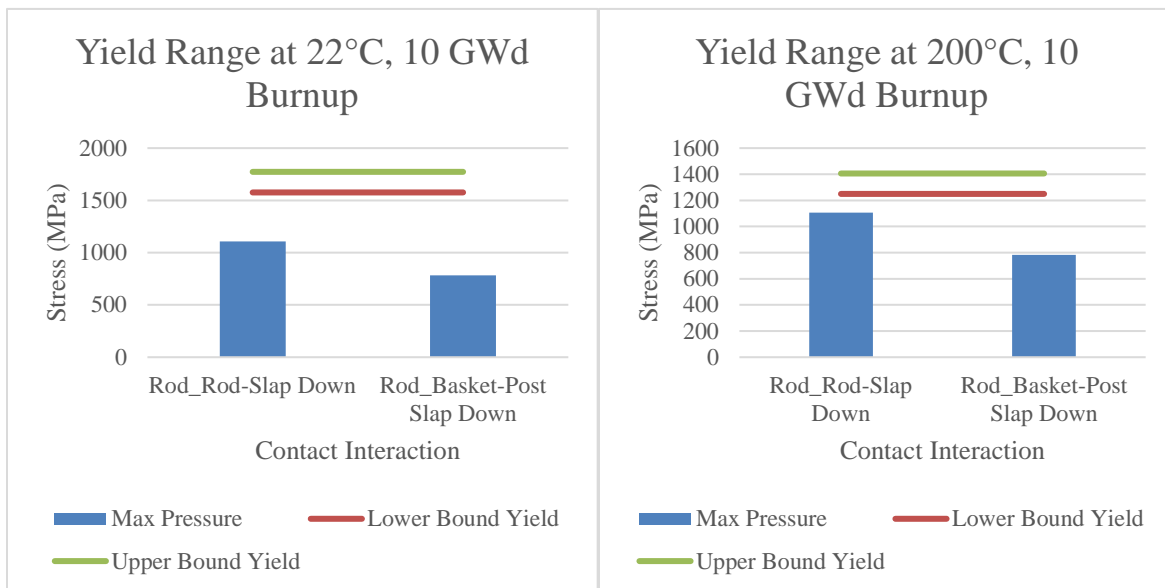
Figure C.14. **Generic 60 Degree Drop – Contact Pressure in Relation to Yield Point Range: 22°C, 10 GWd Burnup (left) and 200°C, 10 GWd Burnup (right)**

As seen in Figure C.13 and Figure C.14 the cladding never exceeded yield in all of the cases observed in this report. The assumptions used in this work mean that this analysis is likely conservative. As noted in the earlier sections, further investigation is needed to refine the contact force extraction from the fuel assembly model, and further finite element modeling is needed to evaluate cladding integrity limits during contact.

C-3 Conclusion

The maximum contact pressures and resultant circumferential stresses in fuel cladding for two 30 cm drop scenarios were evaluated in this study. The drop scenarios were simulated using the crushable grid fuel assembly model developed in LS-DYNA (Section 4), and the contact pressures calculated using

analytical solutions from Hertzian contact theory. Assumptions about the distribution of contact force and visual inspection of the contact were necessary, because the LS-DYNA model did not report reaction forces at specific locations, only the sum of reactions for an entire rod. The contact locations and curvatures were determined from visual inspection, and the reaction was taken as being the maximum recorded at the respective time step. Under these assumptions, it was determined that the cladding does not exceed yield for the cases studied. However, the true contact force could be different and likely lower than the values used in this study. Thus, further investigation is needed to obtain location-specific contact forces and better estimates of cladding contact pressure. In addition, more finite element modeling should be conducted to further investigate the contact stress allowable. Additional study could be done to investigate the total stress state in the cladding from sources such as bending and internal pressure and incorporating the individual contact stress components calculated in this work. Lastly, stresses and stress concentrations due to rod-to-fuel pellet contact during rod impact events should be investigated.

C-4   References

Barber, J.J. "Hertzian Contact." Contact Mechanics, Springer, 2018, pp. 37–37.

Kim, J.S., Hong, J.D., Yang, Y.S., et al. "Rod Internal Pressure of Spent Nuclear Fuel and Its Effects on Cladding Degradation during Dry Storage." *Journal of Nuclear Materials*, vol. 492, 2017, pp. 253–259., doi:10.1016/j.jnucmat.2017.05.047.

Young, W.C., Budynas, R.G. Roark's Formulas for Stress and Strain: Warren C. Young; Richard G. Budynas. 7th ed., McGraw-Hill, 2002.

This page is intentionally left blank.

APPENDIX D

DAMAGE MODEL

The damage prediction model described in Section 6 was developed using regression analysis to find functions and associated parameters that result in the least deviation from expected results. The regression analysis was applied in multiple steps. First, functional relationships were prescribed to attempt to fit input parameters to output results. Second, least-squares regression was used to refine the functional relationships. Finally, residuals of the fitted models were compared to determine which functional relationship best represented the conversion from input parameter to output results. Besides the initial identification of functional relationships, all processing was performed using scripts written in Python (python, 2020).

D-1   Functional Relationships

The functional relationships used to relate input variables to output results can cover any range of equations. Examples include trigonometric functions, exponential decay, linear relationships, and higher order polynomials. For each of these examples, there can be multiple parameters that must be solved to fully quantify the relationship between the input variables and the output result. In addition, the different input variables are expected to each have their own functional relationships such that the full model will be some combination of the individual functional relationships. For simplicity, it is assumed that the individual functional relationships will be combined into the overall model using elementary arithmetic (addition, subtraction, multiplication, or division).

An example functional relationship could involve a sinusoidal relationship for one variable and an exponential decay for another variable. Individually, the functions would take the forms given in Equation (D.1.) and Equation (D.2), where x_1 and x_2 are the varied inputs and the constants are fitting parameters.

$$f_1(x_1) = a_1 \sin(b_1 x_1 + c_1)$$

(D.1)

$$f_2(x_2) = a_2 \exp(b_2 x_2 + c_2)$$

(D.2)

Assuming the overall model can be represented as the product of the functional relationships of the two variables, the overall functional relationship for the model can be produced, as given in Equation (D.3). Again, x_1 and x_2 are the varied inputs and all constants are the parameters that fully define the relationship.

$$f(x_1, x_2) = a_1 \sin(b_1 x_1 + c_1) \times a_2 \exp(b_2 x_2 + c_2) + d$$

(D.3)

D-2   Least-Squares Regression

Once functional relationships are defined, least-squares regression is used to solve for the parameters in the functional relationships. As applied in the damage prediction model, this regression minimizes the sum of squared residuals, where the residual is the difference between the predicted value, $f(x_i, \beta)$, and the expected value, y_i, for each distinct set of input parameters, β. This minimization is given in Equation (D.4).

$$\min_{\beta} \frac{1}{2} \sum_{i=1}^{n} \left(y_i - f(x_i, \beta) \right)^2$$

(D.4)

For the damage model, the least-squares regression was performed using built-in functionality of the SciPy Python package, which is "a Python-based ecosystem of open-source software for mathematics, science, and engineering" (SciPy.Org, 2020).

D-3   Regression Validation

Once the desired functional relationships are solved for, the model must be validated. A simple first check is to visually inspect the results. An example is given in Figure D.1 where X is the best fitting function and Y is a worse fitting function. This example is based on data generated by starting with Equation (D.3) and adding noise to the results.
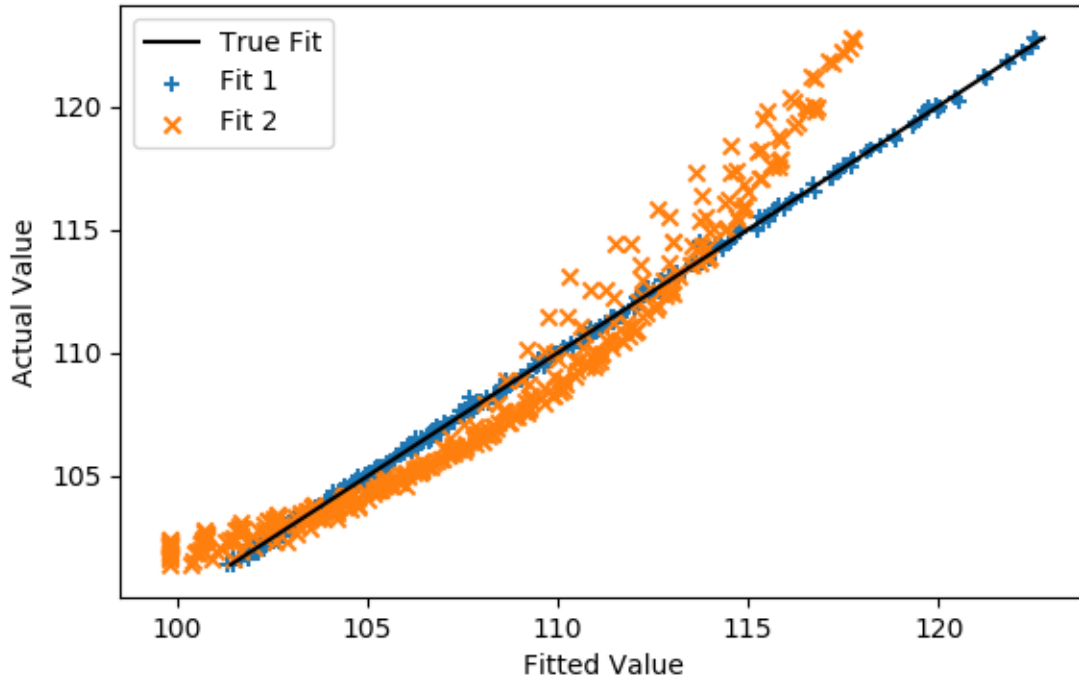
Figure D.1. Comparison of Fitted and Actual Values for Data Used in Model Generation

Another check for validity is comparing the result to data that were not used in producing the model, as shown in Figure D.2. Fit 1 provides a reasonable fit for data that were not used for model generation. Fit 2 shows how a fitted model that could be considered acceptable for a certain range can perform much worse when comparing to a larger data set.
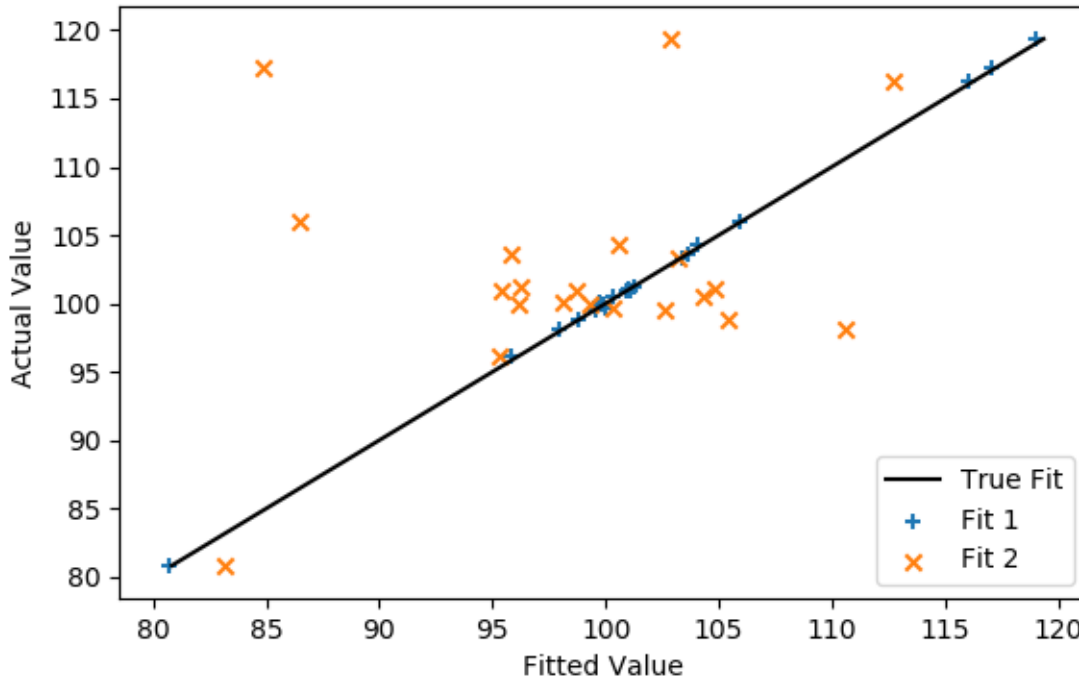
Figure D.2. Comparison of Fitted and Actual Values for Data Not Used in Model Generation

D-4   Final Model

The final fitting model is determined as an artifact of the regression and its validation. If the best fitting regression as determined by the residuals is also deemed a valid regression, then that model is used. For the two fits presented in Figure D.1 and Figure D.2, Fit 1 would be chosen. In practice, several more fitting functions should be considered.

Further considerations about the applicability of this method may also be necessary. For example, issues could arise based on the quantity of available input data, relationships between independent variables (i.e., covariance), or overfitting, especially in the presence of outliers. Future work should include improvements to better recognize these potential issues so that an enhanced damage model can be reliably used.

The framework for the damage model has been developed and tested and is now ready to incorporate model results, data from drop tests, and any relevant data from the Sibling Pin testing program.

D-5   References

"python," Python Software Foundation, 2020. [Online]. Available: https://www.python.org.

"SciPy.Org," The Scipy Community, 11 July 2020. [Online]. Available: https://docs.scipy.org/.